University of North Dakota
UND Scholarly Commons

Theses and Dissertations | Theses, Dissertations, and Senior Projects

January 2015

An Experimental Investigation Into The Effects Of High Free-Stream Turbulence On Full Coverage Shaped Hole Film Cooling In An Accelerating Boundary Layer

Joseph Kingery

How does access to this work benefit you? Let us know!

Follow this and additional works at: https://commons.und.edu/theses

Recommended Citation
Kingery, Joseph, "An Experimental Investigation Into The Effects Of High Free-Stream Turbulence On Full Coverage Shaped Hole Film Cooling In An Accelerating Boundary Layer" (2015). *Theses and Dissertations*. 1789.
https://commons.und.edu/theses/1789

This Thesis is brought to you for free and open access by the Theses, Dissertations, and Senior Projects at UND Scholarly Commons. It has been accepted for inclusion in Theses and Dissertations by an authorized administrator of UND Scholarly Commons. For more information, please contact und.commons@library.und.edu.

AN EXPERIMENTAL INVESTIGATON INTO THE EFFECTS OF HIGH FREE-STREAM TURBULENCE ON FULL COVERAGE SHAPED HOLE FILM COOLING IN AN ACCELERATING BOUNDARY LAYER

by

Joseph Elliot Kingery

Bachelor of Science, University of North Dakota, 2013

A Thesis

Submitted to the Graduate Faculty

of the

University of North Dakota

In partial fulfillment of the requirements

for the degree of

Master of Science

Grand Forks, North Dakota

May

2015

This thesis, submitted by Joseph E. Kingery in partial fulfillment of the requirements for the degree of Master of Science from the University of North Dakota, has been read by the Faculty Advisory Committee under whom the work has been done and is hereby approved.

Dr. Forrest Ames

6 May 2015
Date

Dr. Clement Tang

6 May 2015
Date

Dr. Nanak Grewal

6 May, 2015
Date

This thesis is being submitted by the appointed advisory committee as having met all of the requirements of the School of Graduate Studies at the University of North Dakota and is hereby approved.

Wayne Swisher
Dean of the School of Graduate Studies

May 7, 2015
Date

PERMISSION

Title An Experimental Investigation into the Effects of High Free-Stream Turbulence on Full Coverage Shaped Hole Film Cooling in an Accelerating Boundary Layer

Department Mechanical Engineering

Degree Master of Science

In presenting this thesis in partial fulfillment of the requirements for a graduate degree from the University of North Dakota, I agree that the library of this University shall make it freely available for inspection. I further agree that permission for extensive copying for scholarly purposes may be granted by the professor who supervised my thesis work or, in his absence, by the chairperson of the department or the dean of the Graduate School. It is understood that any copying or publication or any other use of this thesis or part thereof for financial gain shall not be allowed without my written permission. It is also understood that due recognition shall be given to me and to the University of North Dakota in any scholarly use which may be made of any material in my thesis.

Joseph E. Kingery
May 2015

TABLE OF CONTENTS

LIST OF FIGURES

LIST OF TABLES

NOMENCLATURE

Cp	specific heat at constant temperature, kJ/(kg·K)
d	coolant hole diameter, m
D	leading edge cylinder diameter, m
h	convective heat transfer coefficient, W/(m²·K)
I	electrical current, amps
k	thermal conductivity, W/(m·K)
L	hole length, m
Lu	energy scale, $Lu = 1.5u'^3/\varepsilon$
Lx	integral length scale, m
M	blowing ratio based on the combined area of hole minimum diameter, $\rho_{co}U_{co}/\rho_\infty U_\infty$
Nu	Nusselt number; dimensionless number, ratio of convective heat transfer to conductive heat transfer, Nu=hDk
p	pitch or spanwise hole spacing, m
P	pressure, Pa
Pr	Prandtl number; dimensionless number, ratio of viscous diffusion rate to thermal diffusion rate, Pr=Cpμk
q"	heat flux, kJ per unit time per unit area
R	resistance; ohms, Ω
ReD	Diameter Reynolds number; dimensionless number, ratio of inertial forces to viscous forces, $ReD = \rho U_\infty/\mu$

S space between rows, m

St Stanton number; dimensionless number, ratio of heat transferred to a fluid over the thermal capacity of the fluid, $St = h/\rho CpU_{ex}$

T Temperature, K

Tu turbulence intensity, Tu = |u'|/U∞

U velocity, m/s

Greek Letter Symbols

α Inclination or injection angle, degrees

β Lateral expansion angle, degrees

Δ Delta, difference

η Eta; adiabatic effectiveness

μ Mu; absolute viscosity, Pa·s

ν Nu; kinematic viscosity, m^2/s

ρ Rho; fluid density, mass per unit of volume, kg/m^3

Subscripts

ac refers to the air conditioner

atm refers to atmospheric conditions

aw adiabatic wall

brkt refers to the mounting bracket

co coolant out

cw cooled wall

D diameter

ex	refers to exit conditions
in	refers to inlet conditions
orf	refers to the orifice
out	refers to outlet conditions
plen	refers to the plenum
r	recovery
s	refers to static conditions
t	refers to total conditions
∞	evaluated in the free stream

ACKNOWLEDGEMENTS

This project could not have been completed without the help of many people. I would like to thank the University of North Dakota Mechanical Engineering Department for providing an excellent undergraduate education, and affording me the opportunity to continue my studies in the graduate program. I would also like to thank Dr. Ames for advising me throughout this project. The knowledge and guidance he provided during my whole college career at UND were very important and appreciated. Thank you also to my advisory committee members, Dr. Nanak Grewal and Dr. Clement Tang. Many thanks to the National Energy Technology Laboratory (NETL), the Department of Energy, and the University Turbine Systems Research (UTSR) program for providing the funding for this work.

There are several students who deserve a great deal of gratitude for their knowledge and assistance: Mitch Busche, Leo Moualeu, Jon Long, and Justin Varty. I would also like to thank Jay Evenstad and Gary Dubuque for all of their help and advice with the manufacturing of components for this project. Thank you also to Teri Salwey and Kristin Pavlish for all of your help.

ABSTRACT

The purpose of this study is to experimentally investigate the effects of high free stream turbulence on shaped hole film cooling and heat transfer in an accelerating boundary layer. Film cooling is one of most widely used techniques in cooling high pressure turbine blades and endwalls, whether they are land based power turbines or those used for aircraft propulsion. In the section immediately after the combustor, there is very high turbulence and acceleration, and adequate cooling must be implemented to ensure that components do not prematurely fail. This study is able to apply high turbulence intensities to a test section whose acceleration profile yields a favorable pressure gradient and allows us to see the real world effects on shaped hole film cooling effectiveness and heat transfer from high turbulence intensities.

The experimentation was conducted in the University of North Dakota large scale low velocity wind tunnel facility. A total of six well documented turbulence intensities ranging from 0.7% to 13.7% were implemented on a large cylindrical test surface at Reynolds numbers of 250,000 and 500,000 and four blowing ratios. The low Reynolds number setup used blowing ratios of M = 0.55, 0.97, 1.35, and 1.89, while only the lowest two blowing ratios were tested at the high Reynolds number. The six turbulence intensities were achieved using a low turbulence (LT) nozzle (Tu = 0.7%), the LT nozzle with a small grid at two locations (Tu = 3.5% and 7.8%), the LT nozzle with a large grid (Tu = 8.1%), and a mock aero combustor with and without a decay spool (Tu = 9.3% and

13.7%). The shaped holes leading edge insert was designed to provide full coverage with two staggered rows of holes with 8º lateral expansion. Both rows of holes are introduced to the surface at 30º.

Data showed turbulence to be detrimental to shaped hole film cooling effectiveness in all cases, and to increase heat transfer as the early onset of transition was amplified. The low Reynolds number showed improved film cooling effectiveness over the high Reynolds number due to a longer transition region and slower boundary layer growth. Comparisons of shaped hole film cooling to previous slot film cooling data show the slot to have similar performance in the latter half of the test surface. However, heat transfer and adiabatic effectiveness were much higher in near region due to the slot's superior coverage. IR camera measurements of shaped hole film cooling show the coolant coverage of the surface at the two low blowing ratios, giving a better perspective on the behavior of the coolant jets after ejection. These data should be useful for comparison in future studies.

CHAPTER I

INTRODUCTION

In this day and age, gas turbine manufacturers are continuously working to improve both efficiency and power output. To meet this demand, they are commonly choosing the proven technique of increasing combustion temperature. When temperatures are increased, more work can be extracted from a given amount of fuel. First generation gas turbines had recorded turbine inlet temperatures of lower than 550 °C and thermal efficiency of under 5%. Today those temperatures are commonly in the 1200-1400 °C range and thermal efficiencies are over 40%. Some manufacturers are even pushing that number up to 1600 °C for some ground based power plants. Since these temperatures exceed the metallurgical limits of the superalloys used in the blades and vanes, improved cooling techniques must be implemented to prevent oxidation and premature failure. These techniques most commonly include the use of thermal barrier coatings and film cooling.

Thermal barrier coatings generally consist of four layers with the outermost being a ceramic topcoat made of zirconia-based compounds. These coatings have very low thermal conductivities which insulate the metal from the extreme temperatures by providing a fourth conductive resistance between the external convection of the hot gases and the conduction through the blade wall [1].

Film cooling was introduced nearly 60 years ago and today is very widely used among gas turbine manufacturers. It is considered to be a game-changing technology that has had a remarkable impact on the ability to reach combustion temperatures present in gas turbines today [2]. Combustion temperatures have been increased three times as fast by improvements in cooling technology as by improvements in materials engineering [1]. Film cooling works by extracting cool air from the low pressure compressor and forcing it through the internal chambers of the high pressure turbine vanes and blades. The coolant is then ejected through holes or slots onto the surface of the vanes and blades to form a thin film. This moving film works as an insulation from the extreme temperatures, and can also help to reduce deposition on early stage vanes. Deposition has proven to be detrimental, and the resulting partial blockage of film cooling holes has one of the most adverse effects on cooling performance [3]. A build up of deposits over time can result in large aerodynamic losses as well as hot spots, another cause of premature failure.

On the near pressure and near suction sides of a first stage vane, there is an area of low relative velocity and high acceleration and turbulence. This highly complex flow creates a need for improved cooling techniques that will efficiently use coolant by providing good surface coverage and keeping the coolant near the surface. The ability of this unique test rig in UND's large-scale low-velocity cascade facility to recreate those conditions gives this project large relevance when considering film cooling performance in gas turbine engines.

CHAPTER II

LITERATURE REVIEW

The literature base of film cooling studies is very substantial. On top of that, there are a large number of variables affecting film cooling performance. This chapter will focus on the areas of round hole, shaped hole, and slot film cooling, as well as the effects of turbulence intensity. Round hole film cooling has largely been the standard since film cooling was introduced nearly 60 years ago. It is the least costly but is often outperformed by other geometries. Ideally, a continuous 2D slot geometry would be used for film cooling, but the reduction in mechanical strength is too great. Shaped hole film cooling has been studied at great length has many desirable characteristics. Shaped holes can often provide near slot-level cooling performance without sacrificing as much strength. However, cost is a large concern for shaped hole manufacturing. Turbulence has shown to generally decrease adiabatic effectiveness while increasing heat transfer. First stage vanes and blades experience very high heat load due to high temperatures and turbulence, requiring efficient use of cooling air.

Slot and Round Hole Film Cooling

Film cooling in its most ideal form would utilize a two dimensional continuous slot to disperse the coolant uniformly across the entire surface it is intended to cool. This

technique does have limitations, however. A continuous slot not only reduces the mechanical strength due to its lack of structure, but it also leads to uncontrollable coolant flow rates with its low flow resistance [4]. The current study hopes to accomplish adiabatic effectiveness levels near that of an ideal 2D slot setup, but with a geometry that does not sacrifice strength.

Busche et al. [5] examined the effects of increasing free-stream turbulence on a 2D slot film cooling setup in an accelerating boundary layer. This study was done under very similar conditions as the current, and is used in several comparisons in a later chapter. They found adiabatic effectiveness levels to essentially order on turbulence intensity at a given blowing ratio, and to increase in effectiveness as blowing ratios increase for nearly all cases. Heat transfer also generally showed a moderate increase for increases in turbulence intensity primarily due to earlier transition.

In order to create a more structurally sound method of slot film cooling, Bunker [6] studied mesh-fed slot film cooling. The mesh-fed slot used in this study utilized an array of pedestals with height-to-diameter ratios of 0.2, and proceeded onto 20° inclines to the surface. These pedestals increase flow uniformity as well as add strength. His results showed the mesh-fed slot film cooling to outperform a row of shaped holes by 25% in the near slot region and by 100% in the downstream region.

Simon [7] worked to develop equations capable of predicting slot film cooling efficiency based on parameters of turbulence intensity, temperature, and flow. The model he developed included an initial region where there is a possibility of highly efficient film cooling, and a fully developed region where complete mixing of coolant

and free-stream occurs. The model was able to predict values within 4% of his experimental data.

Discrete hole film cooling has been studied at great length in the pursuit of improvement. It is still the most widely used geometry for film cooling in gas turbines though it is certainly not the most effective. L'Ecuyer and Soecthing [8] examined many articles on the subject of density ratio's effect on discrete hole film cooling. They noticed the occurrence of three different regimes and based them on velocity ratio for a 35º inclined hole. The mass addition regime occurs at velocity ratios below 0.25, and is where effectiveness levels increase due to increased coolant thermal capacity. The mixing regime is at velocity ratios between 0.25 and 0.8, and is where effectiveness levels are influenced by the opposing mechanisms of increased coolant thermal capacity and increased mixing. Above a velocity ratio of 0.8 is the penetration regime where the coolant jets penetrate into the free-stream and increase turbulent diffusion of the coolant. They were able to develop a correlation for discrete hole cooling performance using data from Pederson et al [9], who looked at a wide range of density ratios. They found density ratio to have a large effect on cooling effectiveness at a given blowing ratio due to variation in normal momentum. Sinha et al. [10] conducted a similar study and found similar trends. They found that jet detachment and reattachment scaled with momentum flux ratio and became more important as blowing ratios increased. Since spanwise effectiveness is largely dependent on lateral spreading, lower density ratios and higher momentum flux ratios reduced coolant spreading and thus, reduced spanwise effectiveness.

Liu et al. [11] used pressure sensitive paint in a study examining the effects of blowing ratio, density ratio, turbulence intensity and momentum flux ratio. Their work showed continuous improvement in cooling effectiveness with increasing blowing ratio on the pressure side, and continuous improvement with increasing density ratio on the suction side. Turbulence was detrimental to all cases tested.

Foster and Lampard [12] changed the injection angle, hole spacing, and upstream boundary layer thickness for a row of round holes. For the low blowing ratios they found that effectiveness increased as injection angle decreased, while at high blowing ratios the effectiveness increased with increasing injection angle. Increases in boundary layer thickness were shown to reduce effectiveness levels since it increased jet penetration and lateral mixing near the wall. They also found smaller spacing to increase coverage and reduce jet detachment.

Leiss [13] varied the pressure gradient and the displacement thickness to hole diameter ratio on a flat plate containing a single row of round ejection holes. He found displacement thickness to have negligible effects on heat transfer values, but found it to severely decrease effectiveness at δ^*/d ratios of greater than 0.2. His research also showed a favorable pressure gradient to cause large reductions in effectiveness for lower blowing ratios. Similar results were obtained by Qin et al. [14]. They also found strong favorable pressure gradients to lead to higher cooling effectiveness on convex surfaces.

Muska et al. [15] worked to develop a method of predicting the overall film cooling effectiveness when placing multiple rows of cylindrical ejection holes in a series, often referred to as the superposition method. This built on a previous method dealing only with slots, and he was able to achieve good agreement between calculated values

and experimental values for different configurations of rows of holes. His research made it possible to use a small number of configurations to develop correlations that apply a vast number of configurations.

Shaped Hole Film Cooling

Many studies have shown benefits to shaped hole film cooling versus other methods. Laveau and Abhari [16] studied the vortical structures of cylindrical and shaped cooling holes. Their work showed the shaped holes to exhibit vortical structures with one fourth the magnitude of round holes, resulting in reduced jet lift-off. The lower effective momentum flux ratio works to reduce jet penetration as well.

A comprehensive summary is given by Bunker [2] and covers several decades worth of studies done on the subject. The diverging exits of shaped holes act as diffusers to reduce the momentum of the coolant and keep it from penetrating the boundary layer. This diffusion also laterally spreads the coolant for excellent coverage when compared to cylindrical holes. In some cases, however, downstream effectiveness is reduced by excessive diffusion of the coolant jet that allows excess free-stream mixing. Laid-back and fan-shaped holes have shown to produce an anti-kidney flow structure which is the opposite of that exhibited by round coolant jets. The drawback found here is a separation of the coolant layer which may also lead to a reduction in downstream effectiveness. Other limitations on shaped hole film cooling are largely the issues with cost and manufacturing [17]. Shaped holes can be on the order of 4 to 8 times more expensive than cylindrical holes.

Dittmar et al. [18] compared various configurations of ejection geometries including discrete holes, discrete slots, fan-shaped holes and compound angle fan-shaped

holes. At low blowing ratios, spanwise averaged effectiveness values only slightly favored the fan-shaped hole geometries. At medium blowing ratios the improvement by the fan-shaped holes was much more apparent, and the discrete slots outperformed all others after a distance of ten hole diameters at high blowing ratios. The discrete slots did not exhibit the same jet separation as the discrete holes which helped the coolant stay near the surface and provide such high levels of effectiveness.

Saumweber and Schulz [19] varied several parameters including lateral expansion angle, injection angle, and hole length in comparing shaped hole cooling performance. They found increasing expansion angle to result in wider spreading of the coolant, but at the cost of a separation bubble causing a fork-shaped cooling pattern. However, extending the hole length from six hole diameters to ten greatly reduced fork-shape. Their work showed inclination angle to have little effect at low blowing ratios, but large influence on effectiveness at moderate to high blowing ratios. Shaped holes and cylindrical holes show opposite trends in effectiveness when inclination angle is increased.

Yu et al. [20] examined diffusion shaped holes and found 30 to 50 percent improvement over cylindrical holes in their setup. Colban et al. [21] found similar results with tests on vane endwall cooling.

Saumweber and Schulz [22] added a second row of either cylindrical or fan-shaped coolant holes at various distances downstream of a first row. Performance downstream of the second row was largely influenced by the flow parameters of the second row. However, effectiveness downstream of the second row was significantly increased with the addition of the upstream coolant row.

Brauckmann and Wolfersdorf [23] varied the compound angle on a row of fan-shaped film cooling holes and found little effect on adiabatic effectiveness. Heat transfer showed a significant increase near 20 diameters downstream for the high blowing ratio likely due to the increased mixing from the free-stream to jet interactions.

Colban et al. [24] applied fan-shaped hole cooling to a full stator vane and ran tests with and without showerhead cooling. They found large amounts of separation on the suction surface due to the severe surface curvature that increased with increasing blowing ratio. The presence of showerhead cooling improved cooling effectiveness on the concave pressure side but no major change was found—the curvature made cooling very difficult regardless. In a similar study, Mhetras et al. [25] saw film cooling decay more slowly on the suction side when jet detachment did not occur.

Schroeder and Thole [26] reviewed much literature on shaped hole geometries and created a "baseline" hole for future comparisons. Their shaped hole has a 30° inclination angle, 7° layback, and 7° lateral expansion. This geometry allows blowing ratios to be pushed higher without worry of jets detaching and eliminates in-hole separation.

Effects of Turbulence

In the combustor section of a modern gas turbine, turbulence intensities vary significantly due to the large variety of engines and operating conditions. The turbulence intensities usually reach a maximum primary zone of the combustor, often as high as 30%. Much research has been conducted in the past on film cooled turbine components documenting the influence of turbulence. Elevated turbulence levels have shown to generally reduce adiabatic effectiveness and increase heat transfer values.

Saumweber and Schulz [27] and Saumweber et al. [28] studied free-stream effects on both round and shaped film cooling holes. Both studies found that at low turbulence conditions, the benefits of shaped hole use are greatly overestimated. They also found that higher turbulence intensities actually can improve effectiveness for higher blowing ratios as the mixing pushes the coolant back to the surface, but the higher intensities always negatively affect shaped hole film cooling. Regardless, shaped holes outperformed round holes.

Using liquid crystal thermography, Mayhew et al. [29] show the effects of turbulence on a flat plate with three holes spaced three diameters. They found high free-stream turbulence to increase spanwise coverage at the blowing ratio of M=1.5 and decrease effectiveness for M=1.0 and M=0.5. In a follow-up study, Mayhew et al. [30] applied similar techniques to study heat transfer. They found the heat transfer was increased with increased turbulence, and a group of holes showed greater increase in heat transfer than just a single hole due to the kidney vortices of neighboring holes strengthening each other.

Ames [31, 32] looked at vane film cooling with single and double rows of film cooling holes. He subjected them to low and high turbulence levels, 0.9% and 12.4% respectively, and found that turbulence has a much larger effect on the pressure side of the vane. Cutbirth and Bogard [33] found similar results when introducing turbulence intensities of 20% to a vane with and without showerhead cooling.

Mayhew et al. [34] found turbulence to reduce effectiveness for low blowing rates and increase effectiveness for high blowing rates. They also found high turbulence to

reduce the vortical structure behind the film cooling hole from two counter-rotating vortices to a single vortex.

A relatively basic row of fan-shaped cooling holes was used by Wright et al. [35]. As turbulence intensity was increased, the jets largely maintained their structures and effectively protected the surface. The shaped holes appeared to be very robust over the range of their flow conditions. The limited interaction of the free-stream with the film cooling flow due to coolant's attachment to the wall and low velocity is a clear advantage of shaped hole use. Similar conclusions were reached by Davidson et al. [36].

Considerations

The current study looks at two staggered rows of shaped holes subjected to an accelerating and transitioning flow. The holes were given an 8° lateral expansion to eliminate the separation bubble seen with larger lateral expansion angles, and were placed in two staggered rows to provide full coverage with uniform flow. Six turbulence intensities between 0.7% and 13.7% and four blowing ratios between 0.55 and 1.90 were used in this study to give a wide range of data. Downstream heat transfer data were also taken to show the state of the boundary later.

CHAPTER III

EXPERIMENTAL APPROACH

This chapter gives a detailed description of the University of North Dakota's large-scale low-velocity cascade wind tunnel facility, as well as the experimental procedure used to acquire surface and free-stream pressure and temperature measurements. A single large cylindrical leading edge test section with constant radius stagnation region and downstream expansion to maintain flow acceleration was fitted with a shaped holes leading edge insert to simulate the film cooling geometry on the leading edge of a first stage vane or blade. A total of six well documented turbulence intensities ranging from 0.7% to 13.7% were implemented on the test surface at approach Reynolds numbers of 250,000 and 500,000 with four blowing ratios. The six turbulence intensities were achieved using either a low turbulence nozzle, a mock aero combustor, or with different grid combinations. The low Reynolds number setup tested blowing ratios of M = 0.55, 0.97, 1.35, and 1.89, while at the high Reynolds number only the two lowest blowing ratios were tested.

Low-Velocity Cascade Wind Tunnel

The University of North Dakota's large-scale low-velocity cascade facility has been used in several studies to acquire heat transfer and other aerodynamic measurements related to issues in gas turbine cooling. The facility, shown in Figure 1, is composed of

several parts: a filter box, a large blower, diffusers, a heat exchanger, a flow mixer and conditioner (installed for this experiment), a flow conditioning section, a series of nozzles, and the test section which contains the leading edge cylinder.

Air is entrained into the wind tunnel through a filter box containing eight Air Handler 6B640 industrial air filters to catch any particulates that might attach to the test surfaces and foul sensors. These filters are 60.96 cm x 60.96 cm (24 in x 24 in) and have a filtering efficiency of 95%. The blower used to entrain and push the air flow through the wind tunnel is a New York Blower 274-AF which can push 6.6 m^3/s at a 5000 Pa static pressure rise. This blower is powered by a 45 kW electric induction motor which is controlled with a Hitachi variable frequency drive. The ability to finely tune the power to the motor via the VFD allows the operator to keep the Reynolds number very near the target number. The blower can be seen in Figure 2.

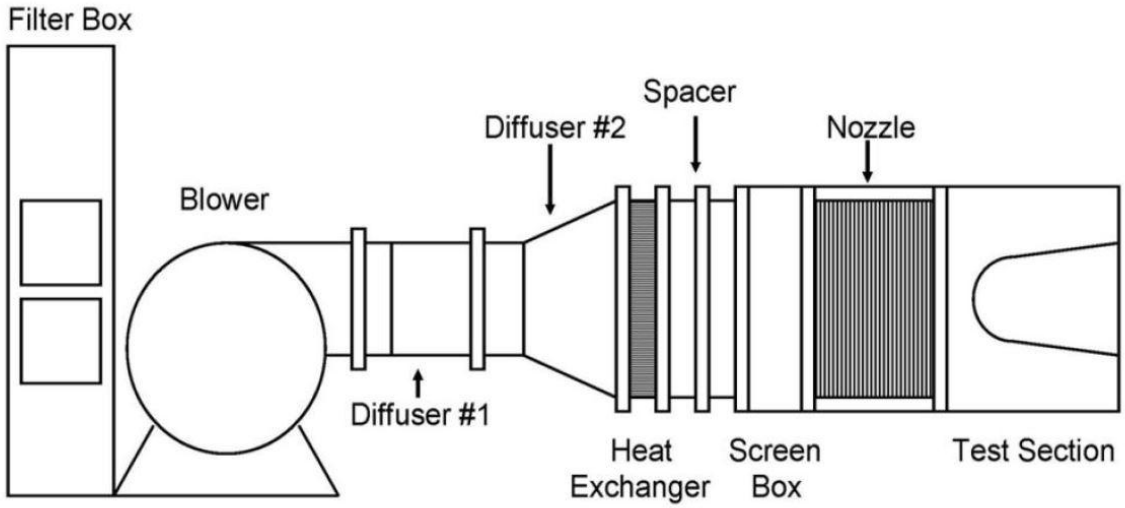

Figure 1. Large scale low velocity cascade wind tunnel [5].

Figure 2. New York Blower used for wind tunnel [42].

Immediately downstream from the blower is a two stage multi-vane diffuser in place to recover some static pressure by expanding and slowing down the air flow. In order to maintain a desired inlet temperature in the tunnel, the air then passes through a 91.44 cm x 121.92 cm (36 in x 48 in) heat exchanger to remove the energy added to the air by the blower. The heat exchanger cooling water is circulated by a1/2 hp jetted tub pump that is connected to a 100 gallon water reservoir. The reservoir also has an inlet for cold water which is used to maintain a desired temperature and an overflow tube that drains excess water straight into a floor drain. Figure 3 shows the heat exchanger system schematic.

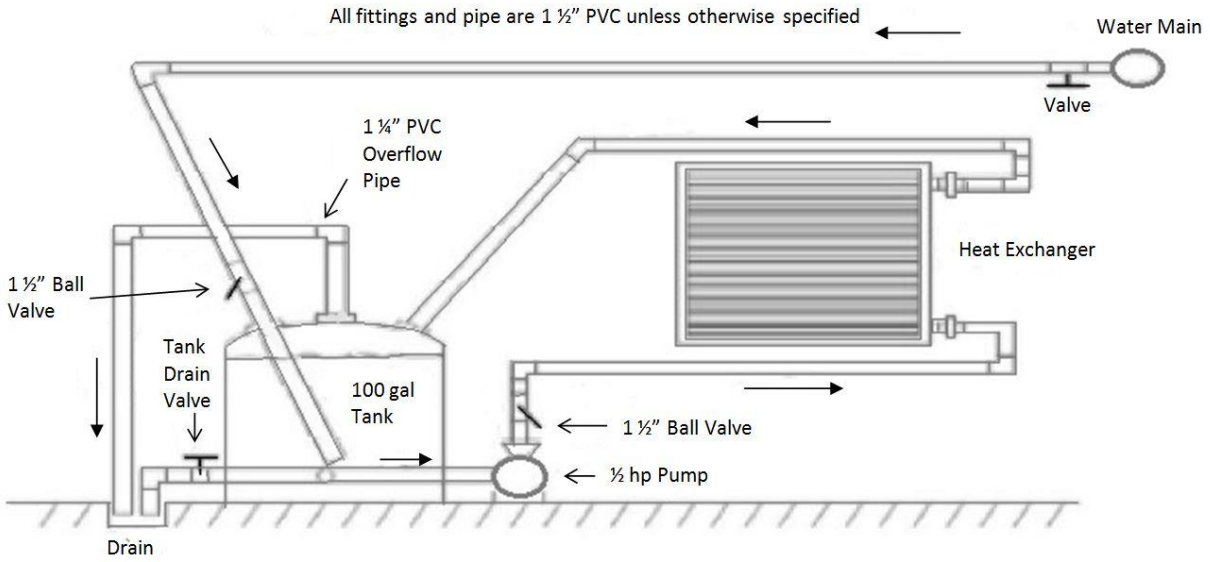

Figure 3. Schematic of wind tunnel heat exchanger [42].

In previous studies it was found that this heat exchanger experiences spanwise temperature stratification when running at higher Reynolds numbers due to several reasons. First, at the high Reynolds number, there is a large amount of cold freshwater being added to the system. Second, the heat exchanger is relatively large so the water circulating has a chance to warm up significantly by the time it returns to the reservoir. In high free-stream turbulence cases, this stratification is largely negated by the extreme mixing that takes place downstream of the heat exchanger. These effects are more pronounced for the lower turbulence cases so a flow mixer was added about 33 cm (13 in) downstream from the heat exchanger, the location where the expansion from the heat exchanger to the full tunnel height ends. The flow mixer is made from 16 gauge steel and measures 91.44 cm x 127 cm (36 in x 50 in). It contains ten rows of five fins turned 30° off the plane perpendicular to the flow, causing the flow to turn 60° right or left,

depending on the row. This helps to mix out the spanwise temperature differences. Figure 4 shows the flow mixer mounted inside the wind tunnel.

Figure 4. Flow mixer installed downstream of heat exchanger.

Since the flow mixer creates significant circulation in the tunnel, a flow straightener was also added, as can be seen on the left of Figure 5. The flow straightener is made from 0.3175 cm (1/8 in) diameter honeycomb aluminum with a streamwise length of 5.08 cm (2 in). The flow then goes directly into the conditioning section on the right in Figure 5 made up of four nylon screens spaced 5.08 cm apart to further reduce variations in the flow velocity and increase uniformity. The combination of these components gives a more uniform flow in both temperature and velocity.

Figure 5. Flow straightener (left) and screenboxes (right).

Turbulence Generation

For this experiment, one of two nozzles was connected to the flow conditioning section. A low turbulence nozzle was used for the four lowest turbulence levels and gave the flow a smooth transition through the 3.6 to 1 area reduction. The mock aero combustor was used for the two highest turbulence levels. Both the low turbulence nozzle and the mock aero combustor have an inlet area of 91.44 cm x 127 cm (36 in x 50 in) and reduce to 25.4 cm x 127 cm (10 in x 50 in). The two nozzles can be seen in Figures 6 and 7.

Figure 6. Mock aero combustor (left) and low turbulence nozzle (right) [42].

Figure 7. View inside the LT nozzle (left) and mock aero combustor (right) [42].

In order to achieve all of the different turbulence levels, several combinations of nozzles and the spool are used. The lowest turbulence intensity of 0.7% is achieved using solely the low turbulence nozzle. The intensity is increased when either a small grid or a large grid are added to the decay spool in between the nozzle and the test section. The decay spool is made of 1.91cm (3/4 in) acrylic and maintains the same 25.4 cm x 127 cm cross section as the two nozzles and the test section. It has holes drilled along the sides at different locations to hold each of the grids in place at their respective locations. The small grid is made up of 0.635 cm square aluminum bars spaced at 3.175 cm or five bar widths. It is placed at two different positions upstream of the test surface, 32 mesh lengths (101.6 cm) and 10 mesh lengths (31.75 cm). When in the far position (SG2), a turbulence intensity of 3.5% is achieved. In the near position (SG1), an intensity of 7.8% is achieved. The large grid is composed of 1.27 cm square aluminum bars with five bar width spacing, and can be seen in Figure 8. The large grid is placed 10 mesh lengths (63.5 cm) upstream. The resulting turbulence from the large grid condition is 8.1%. For the two highest turbulence intensities, the mock aero combustor is used alone and with the decay spool. With the decay spool in place, turbulence intensity drops from 13.7% to 9.2%. These turbulence and flow conditions have been studied to great extent previously [37, 38]. Tables 1 and 2 show the flow conditions and boundary layer parameters.

Table 1. Turbulence level characteristics [5].

Condition	Tu	U (m/s)	Lx (cm)	Lu (cm)
AC	0.1371	8.91	3.45	6.17
AC	0.1377	17.72	3.81	7.08
ACS	0.0933	8.61	4.95	9.48
ACS	0.0924	17.02	4.83	9.81
GR	0.0807	9.70	1.83	3.33
GR	0.0809	18.64	1.94	3.19
GS1	0.0781	9.12	1.61	1.84
GS1	0.0792	17.87	1.12	1.97
GS2	0.0350	9.08	1.73	3.23
GS2	0.0348	17.01	2.13	2.85
LT	0.0076	10.43	5.02	154.5
LT	0.0060	18.71	3.58	15.5

Table 2. Boundary layer parameters [5].

File:	BAC1R3Y1	BAC1R4Y3	BACS1R3Y1	BACSR4Y1
δ^* (cm)	0.0218	0.0174	0.0199	0.0154
δ_2 (cm)	0.0101	0.0082	0.0090	0.0071
H	2.16	2.13	2.22	2.17
Cf/2	0.0061	0.0040	0.0063	0.0041
$Re_{\delta 2}$	54.0	94.5	51.6	85.6
Uinf (m/s)	8.63	19.34	9.28	19.66
Tu0	0.1371	0.1377	0.0933	0.0924
Lu0 (cm)	6.17	7.08	9.48	9.81
File:	BGS2R3Y1	BGR2R4Y5	BLT2R3Y1	BGR2R4Y5
δ^* (cm)	0.0192	0.0158	0.0221	0.0163
δ_2 (cm)	0.0086	0.0069	0.0098	0.0074
H	2.23	2.27	2.26	2.19
Cf/2	0.0064	0.0038	0.0057	0.0036
$Re_{\delta 2}$	50.2	85.6	60.1	95.0
Uinf (m/s)	9.43	20.42	9.99	21.10
Tu0	0.0350	0.0348	0.0076	0.0060
Lu0 (cm)	3.23	2.85	154.5	15.5

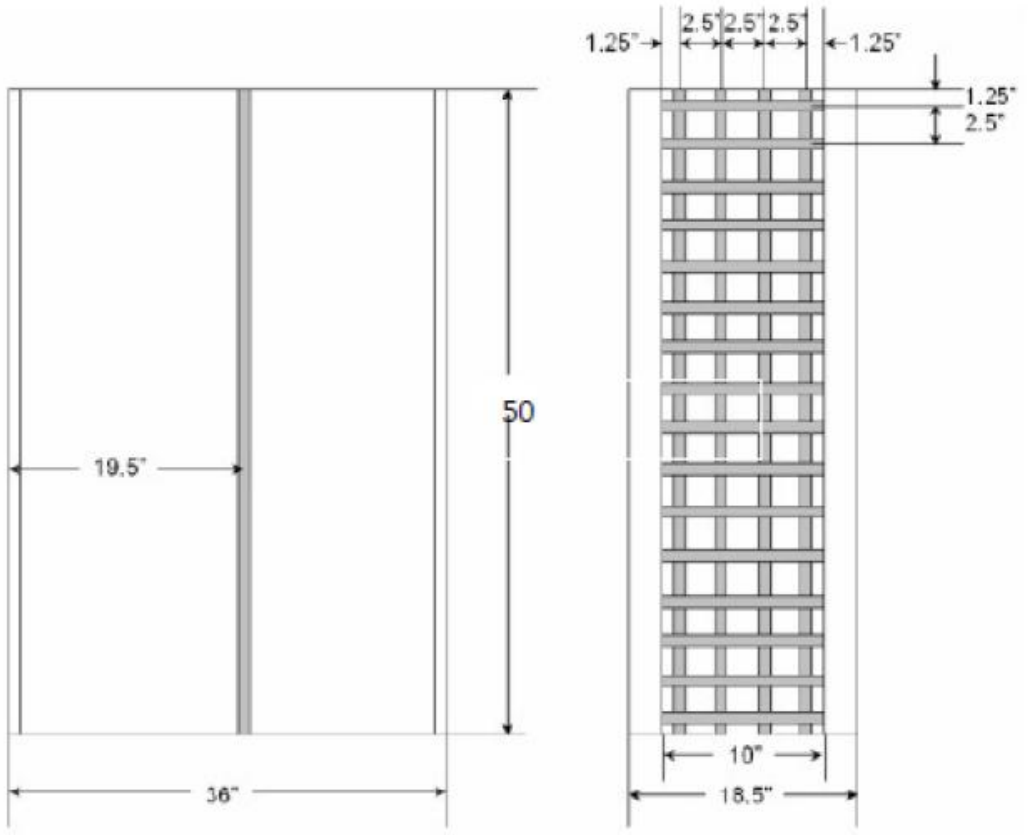

Figure 8. Large grid (GR) schematic with dimensions in inches [43].

Large Cylindrical Leading Edge Test Surface

The test surface shape has been used in several previous studies in the cascade wind tunnel facility. The cylindrical leading edge test surface has a leading edge diameter of 40.64 cm (16 in), and the body was designed by increasing the radius incrementally. The profile of the test surface housed in the test section is shown in Figure 9. The acceleration around the stagnation region is high, but proceeds to taper off. The predicted velocity profile is given in Figure 10.

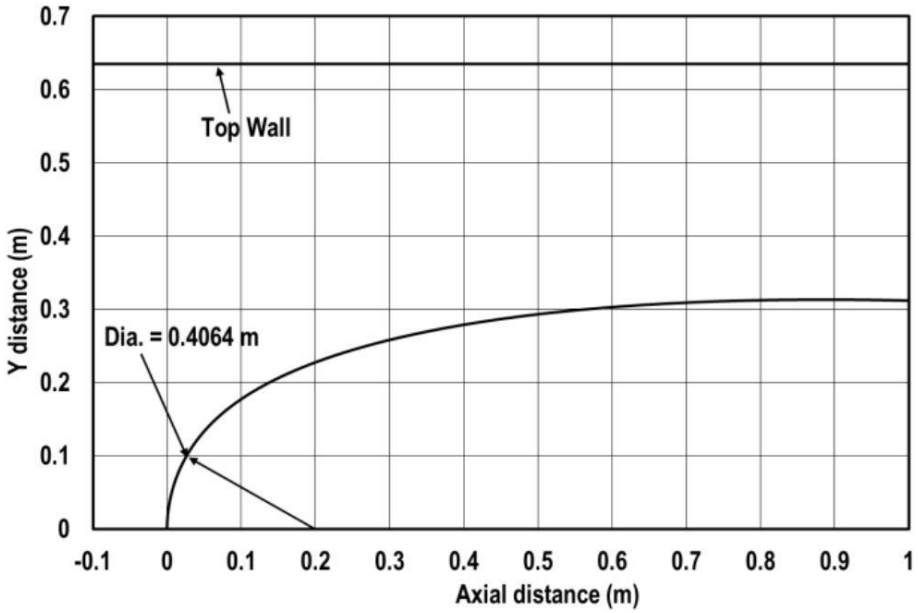

Figure 9. Cylindrical test section schematic.

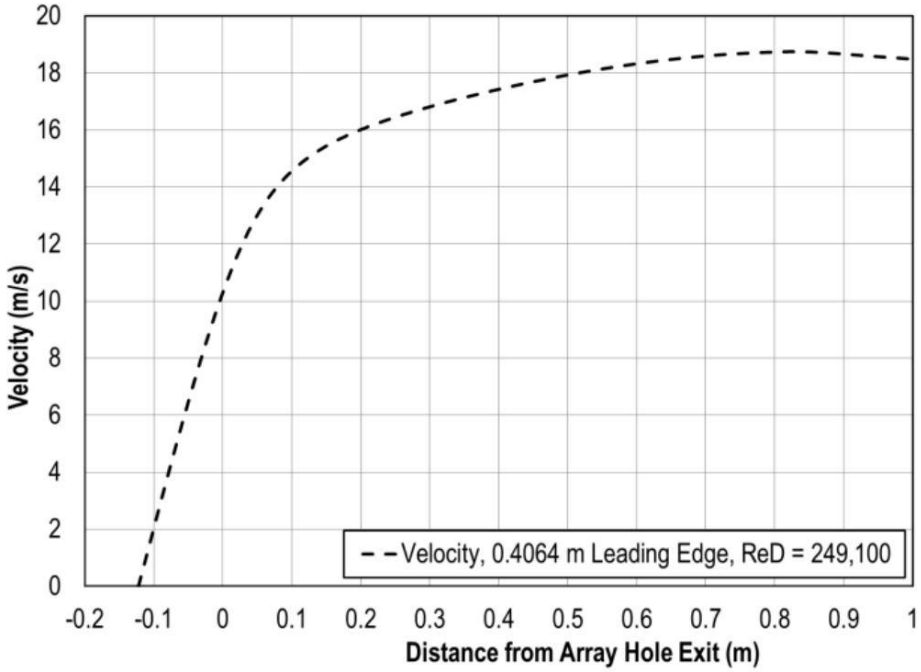

Figure 10. Predicted velocity profile over large leading edge cylinder.

Shaped Holes Leading Edge Insert

The shaped holes insert was designed to fit the existing bracket in the large leading edge cylinder. The insert utilizes a double wall design and a pin fin array very similar to the slot film cooling insert used by Busche et al. [5]. A wireframe representation can be seen in Figure 11. The insert was designed so that air would be injected into the plenum, flow through the pin fin array and then be ejected through the holes.

Construction of the shaped holes insert was done via stereolithography by Quickparts solutions, a branch of 3D Systems in Atlanta, GA. Stereolithography is a very quick and efficient technique of rapid prototyping that utilizes an ultraviolet laser to cure layers of a photopolymer resin. Although it is a relatively expensive technique, the speed and precision at which it can produce parts made it the best option for this project.

The pin fin array used was based on a previously used array and works to create a uniform temperature of the coolant air. The pins have a diameter of 1.68 cm and are spaced 1.625 diameters in the spanwise direction and 1.074 diameters in the streamwise direction. There are three rows of pins in the bottom section and two rows in the top section. Each row of pins is staggered to ensure complete mixing.

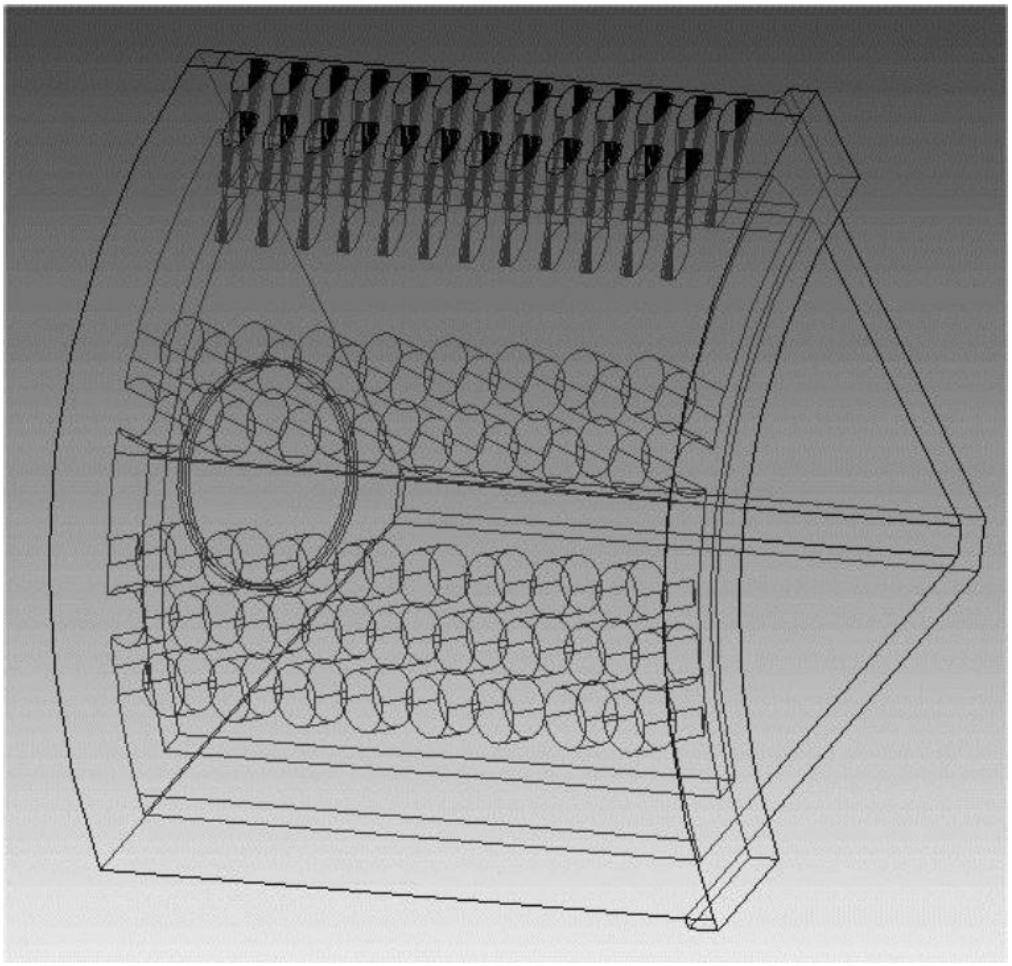

Figure 11. Wireframe model of shaped holes leading edge insert.

The shaped holes insert introduces air to the surface at an inclination angle of 30° with a lateral expansion of 8°. Each hole has a minimum diameter of 0.559 cm (0.22 in) and a length of four diameters. The spacing between rows as well as between holes of the same row is three diameters. Table 1 shows the shaped holes insert dimensions and specifications for the schematic in Figure 12.

Table 3. Shaped Holes Leading Edge Insert Specifications.

Inclination Angle, α	30°
Lateral Expansion Angle, β	8°
Hole Diameter, d	0.559 cm
Hole Length, L	2.24 cm
Pitch, p	1.68 cm
Space Between Rows, S	1.68 cm

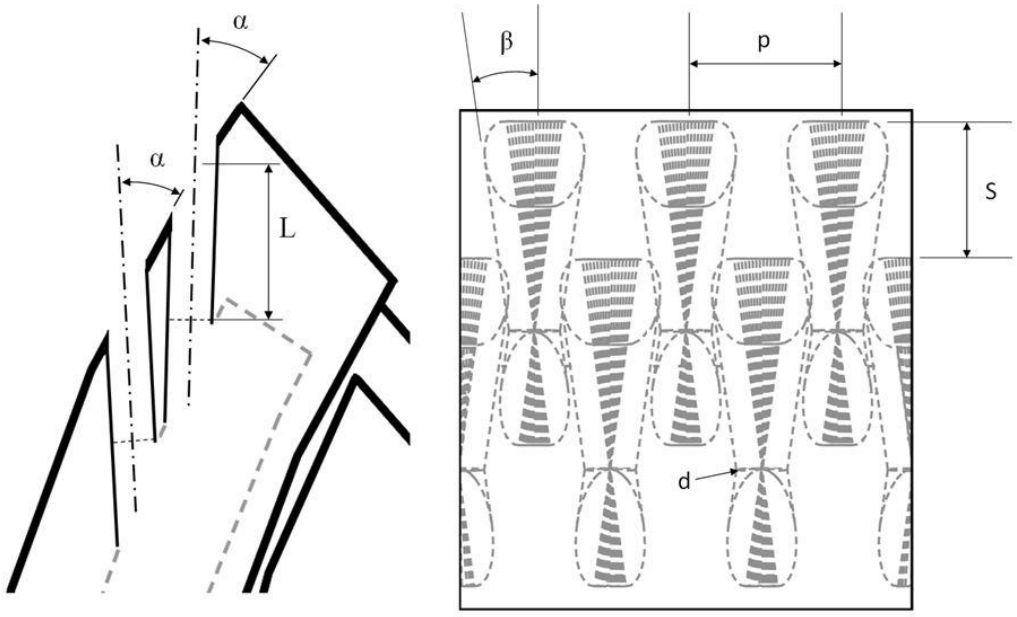

Figure 12. Dimensioned schematic of shaped holes leading edge insert.

Since the insert has no wall on the right side, a piece of acrylic had to be machined to seal the plenum. The acrylic piece is 1.91 cm (0.75 in) thick and a CNC mill was used to cut it to the correct size and shape. It is attached via screws around the outer edge, and silicone applied around the edge provides an airtight seal. For the injection pipe seen in Figure 13, a section of PVC was cut and 1.27 cm holes were drilled with 2.54 cm spacing. Inside the pipe, a baffle was glued into place to meter the flow out of

the holes to provide an even dispersion of the coolant into the plenum. To hold the injection pipe straight, it is pushed into place inside the ring on the far wall of the shaped holes insert. The completed injection system can be seen in Figure 14.

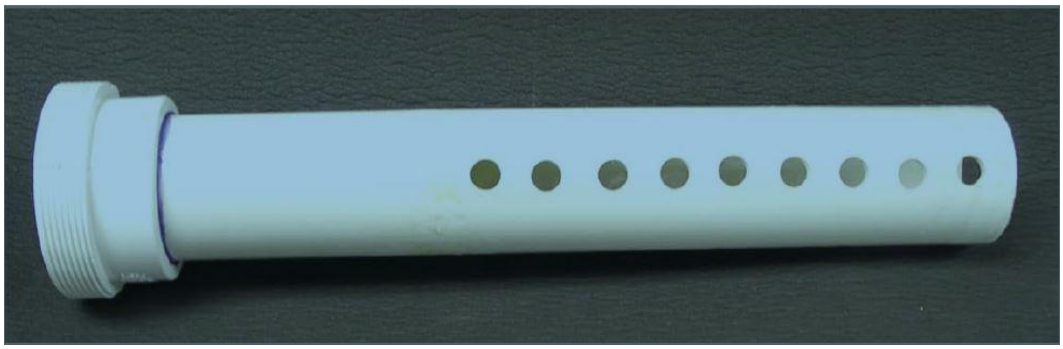

Figure 13. PVC injection pipe with quick disconnect [42].

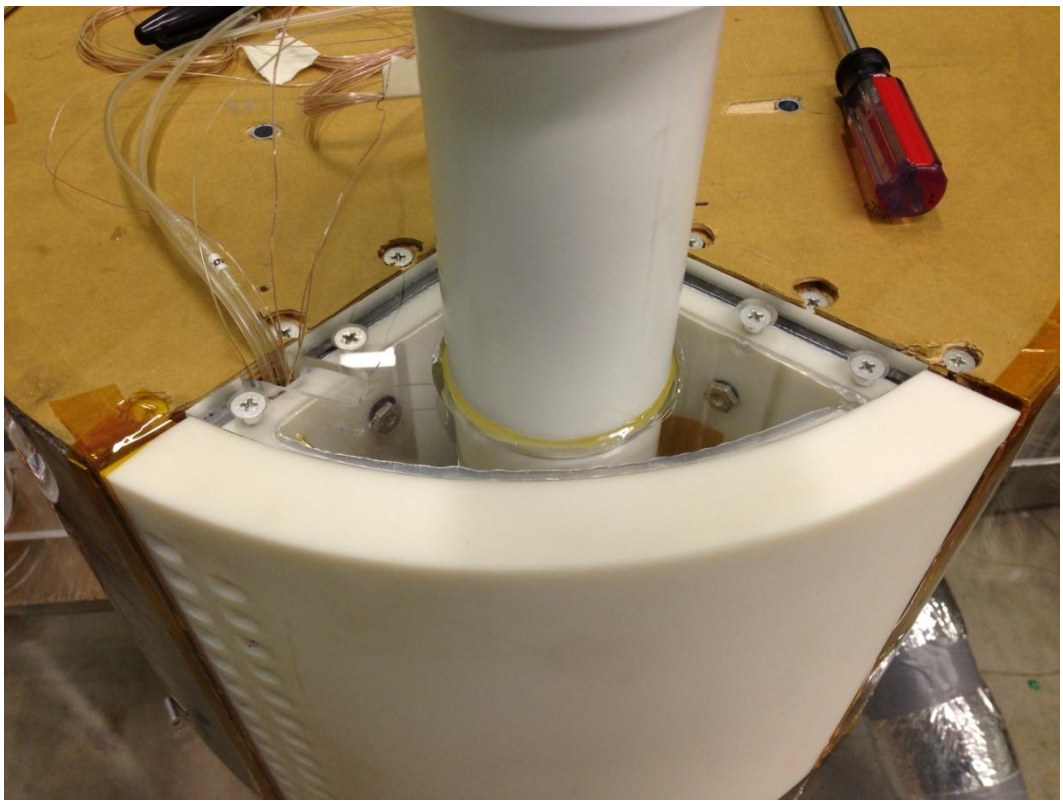

Figure 14. Close-up of injection pipe installed in leading edge insert.

The shaped holes insert is instrumented with both thermocouples and static pressure taps. In two upstream holes and one downstream hole, a thermocouple is placed to get an accurate temperature reading of the coolant air as it is being ejected from the holes. This can be seen in Figure 15. The coolant exit temperature is used in all calculations.

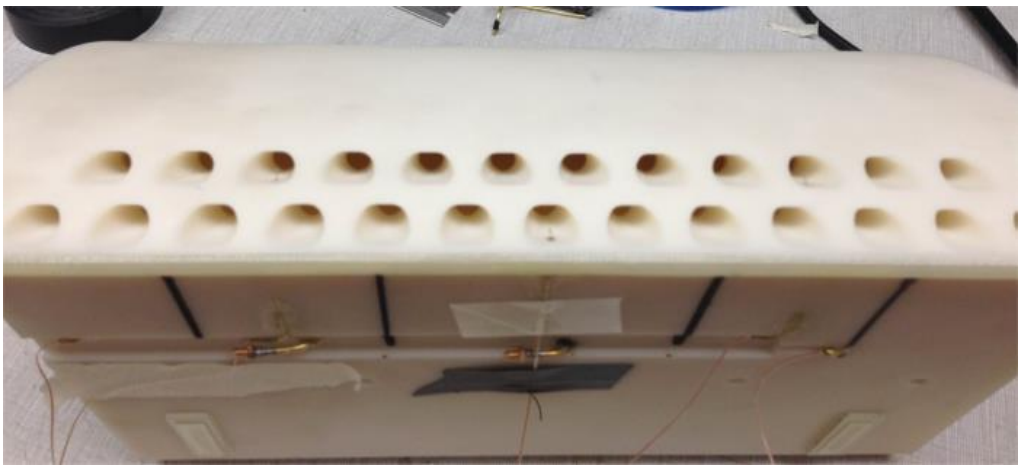

Figure 15. Instrumentation in shaped holes insert.

Test Surface

The shaped holes insert was designed to fit directly into the existing mounting bracket on the large cylindrical test surface seen in Figure 16. The bracket bolts directly to the cylinder and contains ten threaded holes to which the shaped holes insert attaches. Inside the top portion of the bracket are three thermocouples and two static pressure taps. The thermocouples in the bracket are the actual start of the surface temperatures and are used as a reference during the heat transfer tests.

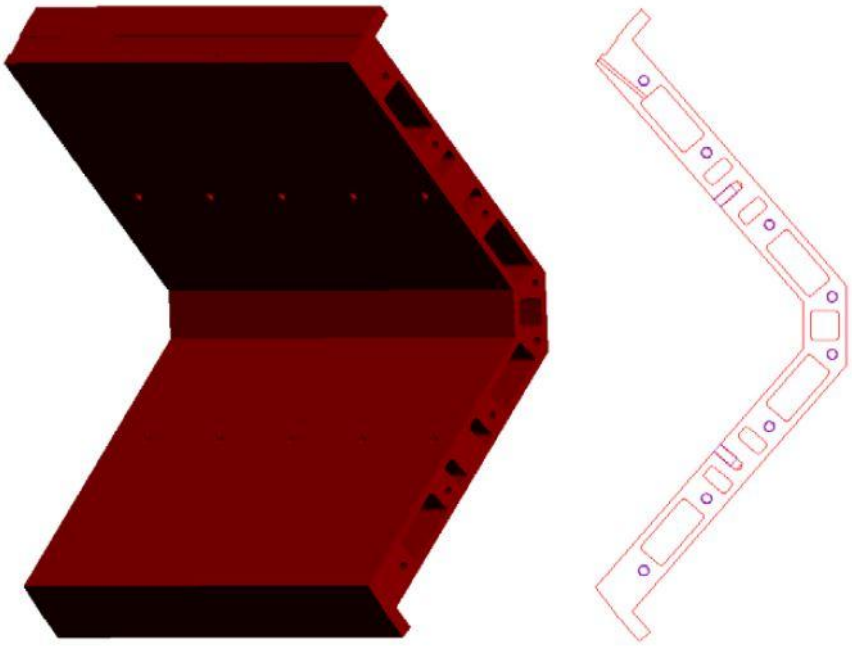

Figure 16. Mounting bracket for shaped holes insert [42].

Sheets of epoxy board are attached to the top and bottom surfaces of the cylindrical test surface. These 0.4 mm (1/64 in) sheets of epoxy board are attached in order to smooth out any variations in the surface from the foam and plywood, and to hold the instrumentation used for temperature measurement. They were cut to 25.15 cm wide by 99.06 cm long (9.9 in x 39 in). Holes of 0.159 cm diameter were then marked and drilled at midspan ± 5.08 cm at a total of 20 streamwise locations on the test (top) surface. The locations of the rows of holes are given in Table 2. In each of the holes, a k-type thermocouple was taped into place on the underside of the epoxy board. Once all 60 thermocouples were in place, the board was flipped over and Omegabond 101 high thermal conductivity epoxy ($k = 1.04\ W/m \cdot K$) was added to each hole to hold the thermocouples in place. Once the epoxy was dry, it was sanded smooth as to not disrupt

the air flowing over the cylinder. After the sanding was complete, the epoxy board was cleaned with alcohol and attached to the cylinder using contact cement. The alignment is guided via two tabs on the bracket to which the epoxy board is screwed down. Figure 17 shows the instrumented top surface and untouched bottom surface epoxy boards.

Figure 17. Epoxy board with thermocouples (left) and bottom surface (right).

Table 4. Thermocouple locations.

Distance from Second Row of Holes to Start of Epoxy Board: 0.7879 inches				Distance from Second Row of Holes to Start of Epoxy Board: 2.0015 cm		
Distance from Start of Epoxy Board to:				Distance from Second Row of Holes to:		
Row	inches	cm		Row	inches	cm
0	0.4	1.0		0	1.2	3.0
1	0.8	2.0		1	1.6	4.0
2	1.3	3.3		2	2.1	5.3
3	1.8	4.6		3	2.6	6.6
4	2.3	5.8		4	3.1	7.8
5	2.8	7.1		5	3.6	9.1
6	3.4	8.6		6	4.2	10.6
7	4.4	11.2		7	5.2	13.2
8	5.4	13.7		8	6.2	15.7
9	6.4	16.3		9	7.2	18.3
10	7.4	18.8		10	8.2	20.8
11	9.4	23.9		11	10.2	25.9
12	11.4	29.0		12	12.2	31.0
13	13.4	34.0		13	14.2	36.0
14	15.4	39.1		14	16.2	41.1
15	17.4	44.2		15	18.2	46.2
16	19.4	49.3		16	20.2	51.3
17	21.9	55.6		17	22.7	57.6
18	24.4	62.0		18	25.2	64.0
19	26.9	68.3		19	27.7	70.3

An Inconel foil manufactured by Tayco Engineering Inc. was then attached to the test surface to create the heat transfer surface. The foil's schematic is shown in Figure 18. Inconel is a superalloy engineered to withstand extreme environments. It is comprised mostly of nickel and chromium, and several other metals including iron and molybdenum may be added depending on the alloy. This composition gives it superior corrosion resistance and high temperature tolerance. Kapton is a polyimide film and is used as backing for the heater foil due to its ability to retain its properties over a wide

range of temperatures. The 0.051 cm x 0.635 cm (0.02 in x 0.25 in) copper bus bars are soft soldered to each end of the foil. The foil heater is able to produce a constant heat flux through the use of a large DC voltage power supply. Varying the differential voltage across the foil allows the user to achieve the desired temperature difference at all blowing ratios and turbulence levels. Since this Inconel heater is not wrapped around the entire leading edge of the test cylinder, an unheated starting length should be accounted for. The presence of this unheated length causes the thermal and velocity boundary layers to initiate at different positions. Kays, Crawford and Weigand [39] give equations for calculating Nusselt number for laminar flow. The Nusselt number on a heated flat plate is given in Eq. 3-1.

$$\mathrm{Nu} = 0.332\mathrm{Pr}^{1/3}\mathrm{Re}^{1/2} \tag{3-1}$$

Since the unheated starting length ξ must be considered, the equation changes to Eq. 3-2.

$$\mathrm{Nu} = \frac{0.332\mathrm{Pr}^{1/3}\mathrm{Re}^{1/2}}{[1-(\xi/x)^{3/4}]^{1/3}} \tag{3-2}$$

As will be seen in Chapter 4, the heat transfer values shown are the Stanton number. Stanton number is a dimensionless value that relates the heat transfer coefficient to the heat capacity of the fluid stream. It essentially shows for this study how the changing flow conditions force convection upon the surface and remove heat from it. The thermocouples on the test surface directly measure the recovery temperature T_r and the thermocouples in the free-stream directly measure the total temperature T_T. The

recovery temperature is used later in calculating the convective heat transfer coefficient. Next, the total net heat of the system must be calculated. This is given in Eq. 3-3:

$$\dot{Q}_{net} = \frac{\dot{Q}_F}{A_F} - \dot{Q}_{rad} \tag{3-3}$$

where $\dot{Q}_F$ is the heat generated by the Inconel heater and is given in Eq. 3-4:

$$\dot{Q}_F = V_F * I_F \tag{3-4}$$

where V_F and I_F are the voltage and current of the Inconel heater, respectively. The current is calculated through the use of a shunt resistor with a known resistance, and the voltage across the foil is measured directly. The surface area of the Inconel heater is represented by A_F. After finding these values, the convective heat transfer coefficient h can be calculated using Eq. 3-5 where T_{hw} represents the heated wall temperature.

$$h = \frac{\dot{Q}_{net}}{T_{hw} - T_r} \tag{3-5}$$

Finally, the Stanton number can be calculated based on exit conditions using Eq. 3-6.

$$St = \frac{Nu}{PrRe} = \frac{h}{\rho_{ex} U_{ex} C_p} \tag{3-6}$$

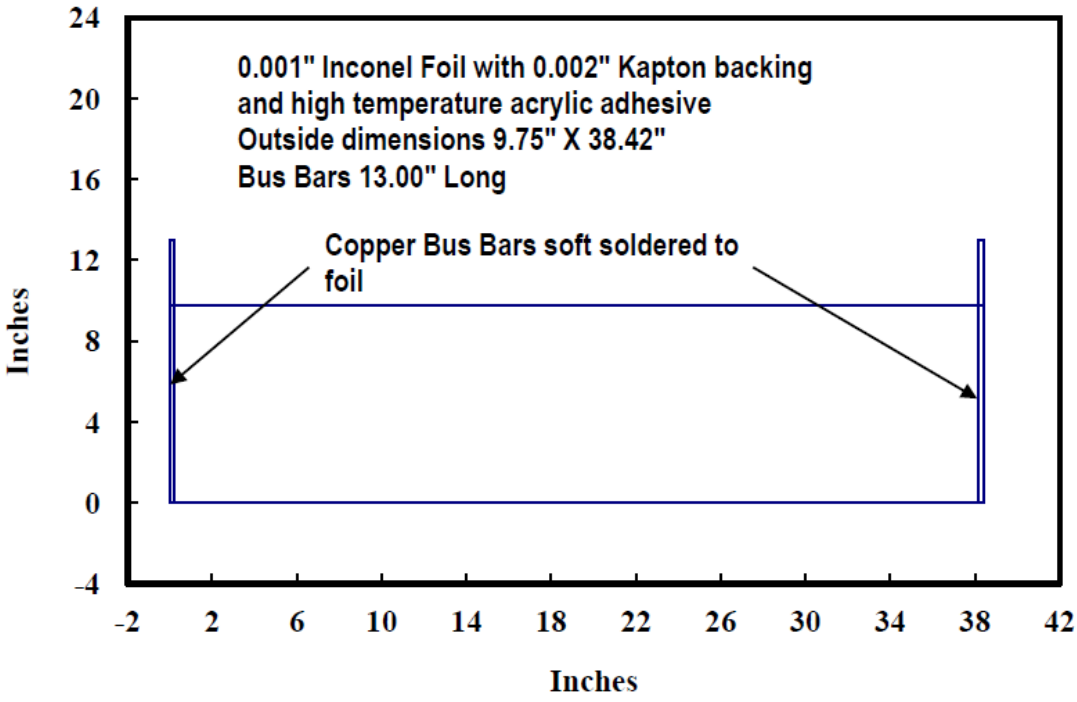

Figure 18. Inconel foil heater geometry.

The test cylinder is built from nine layers of 2.54 cm polyiscocyanurate foam insulation ($k = 0.025\ W/m \cdot K$) between sheets of 1.27 cm plywood. The foam gives a soft surface that the thermocouple wires can be pushed into in order to keep the surface flat and smooth. It also serves to keep the cylindrical test surface's weight as low as possible. Both the foam and the plywood were cut using a router and the jig shown in Figure 19. PL300 foam adhesive was used to bond the layers of foam and plywood. Weights were placed on the entire cylinder once the adhesive was applied to ensure complete adhesion and a constant width. The adhesive was allowed ample time to harden before the weight were removed.

Figure 19. Jig used for cutting cylinder sections.

Infrared Camera Measurements

In order to gain perspective on the film cooling coverage of the cylinder, infrared (IR) camera measurements were taken. The camera used is a FLIR SC500 which gives a 320 x 240 pixel image. In pairing the camera with FLIR Systems ThermaCam Researcher, we are able to get real-time images of the cylinder and its temperature distributions. The SC500 was mounted on an adjustable bracket on top of the test section, allowing the camera to be placed at an angle that would give the best view of the cylinder directly downstream of the shaped holes. A coated zinc selenide window was also added to the top of the test section to provide an interface between the camera and

the test surface. Zinc selenide is often chosen for its low absorptivity at infrared wavelengths and for its visible transmission. This ZnSe window is 7.62 cm (3 in) in diameter and housed in an aluminum fixture that bolts directly to the top of the test section. Figure 20 shows the adjustable bracket and the ZnSe window bolted into place.

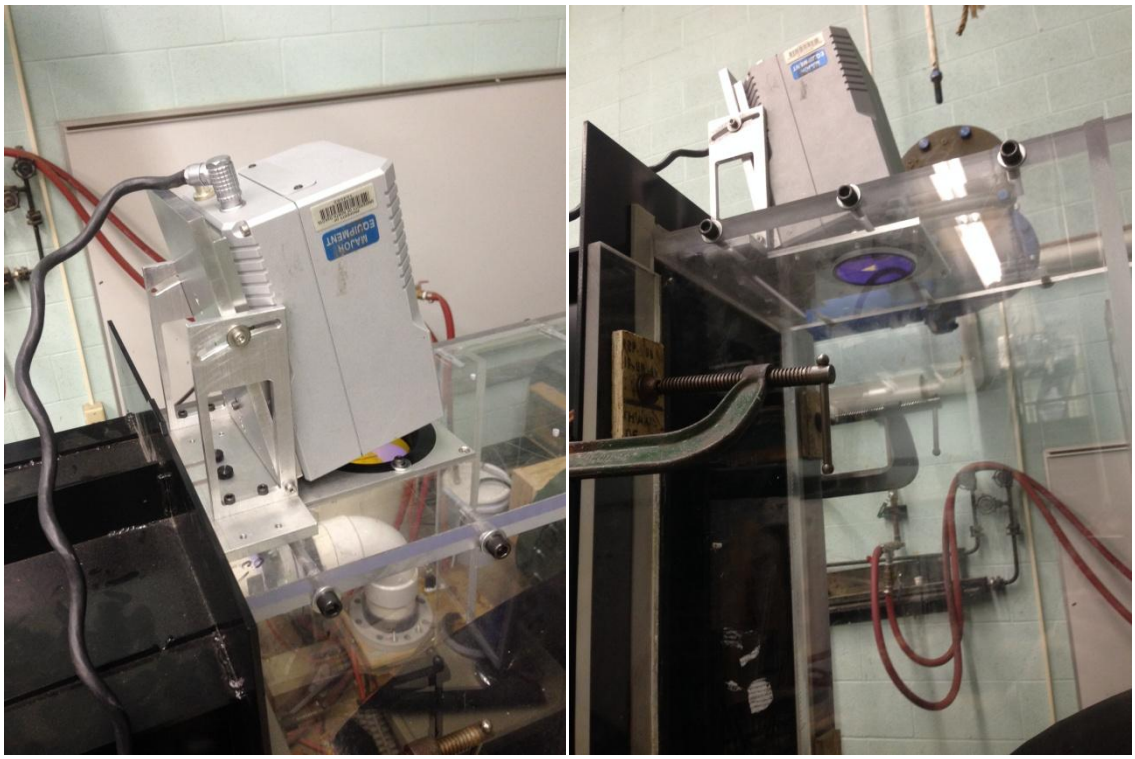

Figure 20. Mounted IR camera and zinc selenide window.

For these IR camera measurements, the test cylinder was painted matte black to have a previously documented emissivity of 0.96. Black acrylic paint was used in a small airbrush to achieve the desired texture and finish. In order to have a reference on the test surface, a grid of gold dots with documented emissivity of 0.437 was added after the black paint cured. The gold dots were painted on the black surface using a jig made from engineering paper. The dots are painted at midspan ± 6.35 cm to fully encompass the

thermocouples, and at 5.08 cm increments in the streamwise direction. The process of painting the gold dots can be seen in on the left of Figure 21, and the finished surface can be seen on the right.

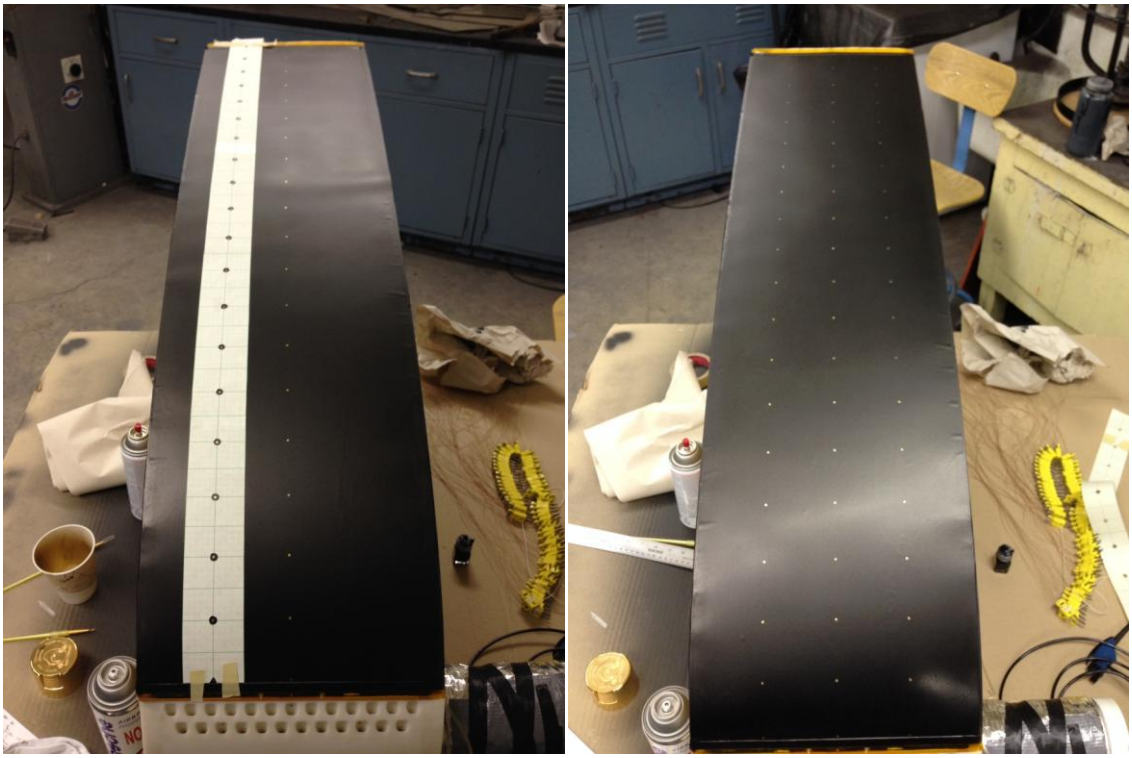

Figure 21. Painted test surface with gold dot jig (left) and completed surface (right).

Once the test cylinder was installed in the test section, a hole was drilled 0.635 cm (1/4 in) off the surface near the start of the painted foil. By inserting a brass rod through the hole and pressing the autofocus button in the ThermaCam Researcher program, the user is able to focus the camera on the surface and get enough contrast to see the gold dots. After the camera was running and the wind tunnel was dialed in to the desired Reynolds number and blowing ratio, a black fleece blanket was placed over the top of the tunnel in order to reduce the outside radiation hitting the cylinder. The blanket is large

enough to hang down both sides of the test section and completely block out the light from reaching the test surface.

New LT Nozzle

For the IR measurements, the blue wooden low turbulence nozzle was replaced with a steel low turbulence nozzle. The blue wooden nozzle had been used for a significant amount of time and experiments and was very much showing signs of wear. The steel pieces used to construct the nozzle were laser cut by Dakota Laser & Manufacturing in Arvilla, ND, and a team of senior design students put them together. After construction, the nozzle was taken to Northern Valley Machine and given a thick coat of black paint. The interior dimensions are identical to the nozzle it replaced so no alterations to the flow path were made, although several adjustments to the H-stands holding it up had to be made in order for it to line up. The new LT nozzle can be seen in Figure 22.

Figure 22. Installed new LT nozzle.

Coolant Supply System

The coolant for this film cooling study was driven by a smaller blower, a New York Blower 1704A. An AC Tech variable frequency drive is used to control the rpm of motor with excellent precision. One problem encountered during the study was the inability to effectively control the inlet temperature in the same way the large tunnel is controlled. In the summer when the lab temperatures were often in the low to mid 80s Fahrenheit, there was a great difficulty in matching the coolant and free-stream temperatures for the heat transfer measurements. The solution was installing a small heat exchanger at the exit of the blower before the air conditioning unit as seen in Figure 23. The heat exchanger system included 1/4 hp submersible water pump in a 5 gallon bucket

and a motorcycle engine oil cooler. A freshwater line allows the addition of colder freshwater into the bucket as the warmed water exits through the drain. The submerged pump pushes water at 25 GPM through the heat exchanger which measures 22.23 cm x 18.42 cm (8.75 in x 7.25 in). Figure 24 shows the heat exchanger with the lid removed. Silicone was used to seal the interior of the box and foam tape was used to seal the lid.

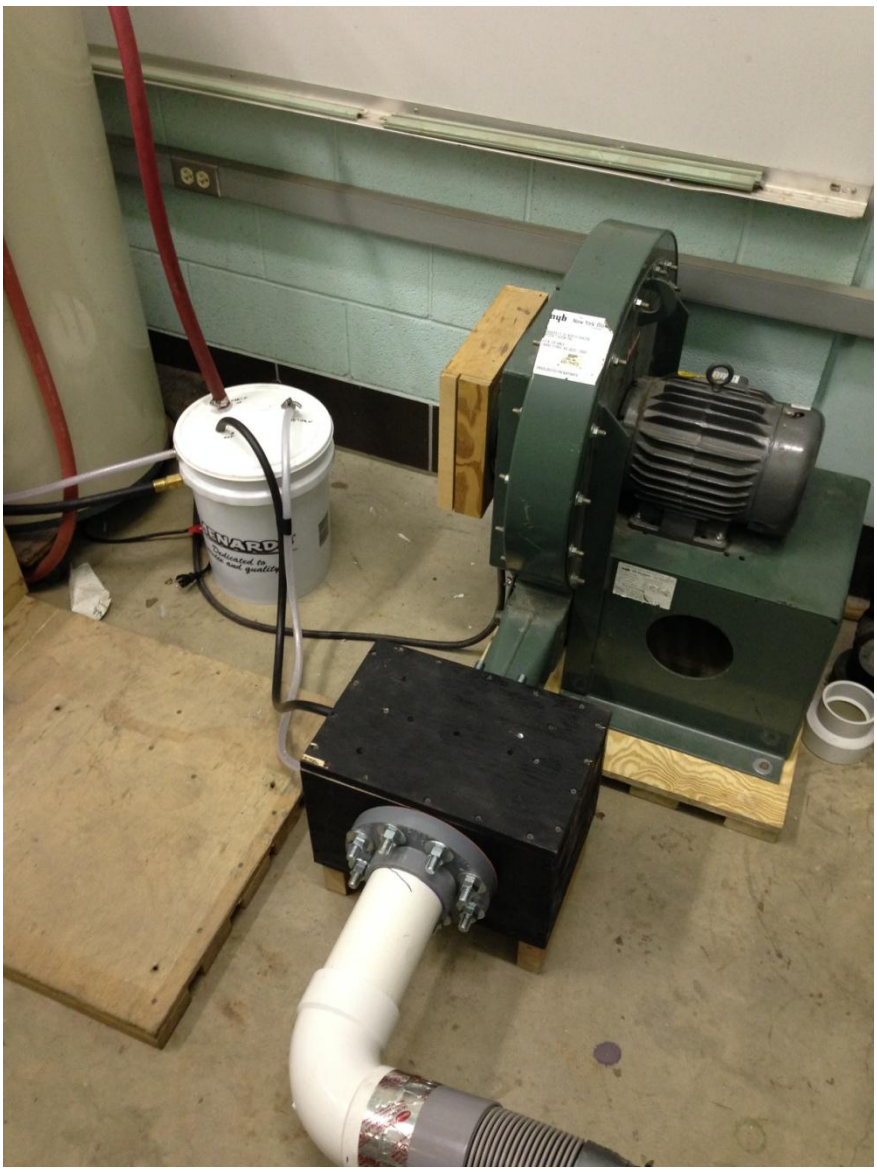

Figure 23. Small blower with new heat exchanger system.

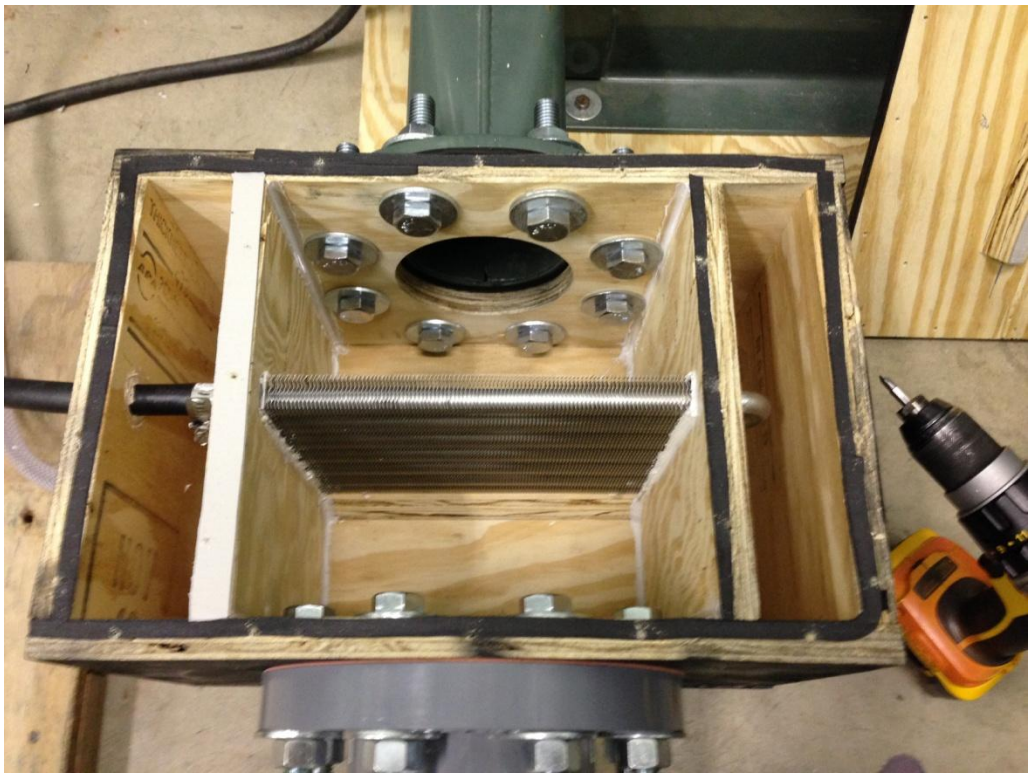

Figure 24. Internals of new heat exchanger.

Air Conditioning Unit. Downstream from the heat exchanger is a small General Electric window air conditioning unit capable of cooling at 5050 Btu/hr. The front fascia was removed and a modified steel plate was screwed to the front to allow the entry and exit registers to be attached. Once the registers were attached, the seams were sealed with aluminum tape and then insulated with reflective foil insulation. Later, the squirrel cage was removed from the air conditioning unit to allow the blowing to come solely from the blower. It seemed that as both the blower and air conditioner were forcing air through the air conditioner, the blowing ratio became harder to maintain.

Thermal Inertia Box. The coolant air then entered the thermal inertia box. This box was constructed to provide a thermal mass for the coolant system, allowing the coolant to remain cool enough to reach the desired temperature difference in the test section for a

significant period of time. Inside the box are thirteen aluminum plates previously used to cast turbine vanes. Each plate measured 2.54 cm x 25.4 cm x 55.88 cm (1 in x 10 in x 22 in) and was spaced using small pieces of 0.3175 cm (1/8 in) particle board at the corners. The box itself was constructed from plywood and 2.54 cm polyisocyanurate foam insulation was taped to the outside of the box to prevent losses.

Orifice Plate. Once the air had passed through the thermal inertia box, it passed through a section of 7.62 cm (3 in) PVC pipe containing a ball valve used to bleed air before the orifice plate. The ball valve was in place to bypass flow after the thermal inertia box to cool the plates down more quickly, and to keep the coolant as cold as possible for the film cooling cases. The only case where the ball valve was necessary was the 250,000 Reynolds number with 0.55 blowing ratio. The orifice plate is a 0.635 cm (0.25 in) disk of aluminum with a 3.175 cm (1.25 in) hole cut out of the middle. The upstream side of the hole is very sharp and the downstream side is beveled at a 45° angle. By placing a static pressure tap on both the upstream and downstream sides of the orifice plate, we can calculate the mass flow rate of the coolant with this pressure difference and the area of the hole. This pressure drop is then used to calculate the blowing ratio. In order to ensure smooth and fully developed flow, the section of PVC pipe preceding the orifice plate was 25 diameters (31.25 in) and a section of PVC with a 16 diameter (20 in) length was used downstream before the flexible hose. Since some turbulence levels required the decay spool to be in place, flexible hose was needed to connect the coolant system to the shaped holes insert to accommodate the different locations of the test section. Figure 25 shows the small blower with the heat exchanger, the thermal inertia box, the bleed valve and the orifice plate.

Power Supply. This project utilized a powerful DC power supply to deliver current to the Inconel foil heater. A precision constantan shunt resistor with 0.001 ohm resistance and ± 2% accuracy was connected to the power supply's output and used to determine the heater current by measuring the voltage difference across it. Using the calculated current and the direct measurement of the voltage across the Inconel foil heater, the power used by the Inconel heater was calculated. That value was then used in calculating the heat transfer coefficient and Stanton number.

Figure 25. Entire coolant supply system.

Data Acquisition

Data were acquired for this study via a Hewlett Packard 3497A data acquisition system. It is capable of reading 100 channels of DC voltage measurements with a sensitivity of one microvolt. The HP unit was connected to a Dell OptiPlex GMT-590 computer.

Pressure Measurement. Pressure measurements for this study were acquired through the use of two Rosemount pressure transducers. The smaller one measured differential pressures up to 250 Pa, while the larger was capable of measuring differential pressures up to 5000 Pa. Both of the transducers have a documented accuracy of ±0.1% of full scale. These transducers were connected to the pressure sensor board, also housed in the data acquisition tower. The board is composed of an MC Computing CIO-ERB48 board connected to 48 12VDC pressure solenoids with 1-44 connected to the low side of the transducers and 45-48 connected to the high side.

Temperature Measurement. All thermocouples used in this study were k-type, or composed of chromel and alumel. Each thermocouple was cut to length from a roll of 36 gauge wire from Omega, and at one end the chromel and alumel wires were welded into a junction using a Therm-X thermocouple welder. The unwelded end was then attached to a male plug. Temperature measurements were taken using these thermocouples in the free stream, inside the plenum, inside the holes, on the bracket, on the test surface, before and after the air conditioner, and at the orifice. The temperature measurements were referenced to an ice bath to ensure accuracy. The ice bath consisted of a Thermos with a hole drilled in the cap, through which a glass tube was inserted. Mineral oil was added to the tube to give a uniform temperature inside the tube, and a thermocouple was then

inserted deep enough to reach the mineral oil. All of the male plugs from the thermocouples were attached to the board on the front of the data acquisition tower. The data acquisition tower can be seen in Figure 26.

Figure 26. Data acquisition tower [42].

Procedure. The procedure for acquiring data in the wind tunnel had several steps. The water pumps and blowers were turned on first and the Quickbasic program was opened. In the program, the barometric pressure was entered and the pressure sensors were zeroed. The program was then turned to the monitoring routine and the large blower was adjusted to the desired Reynolds number, and the freshwater valve was opened enough to

maintain a steady inlet temperature. The small blower was then tuned to set the blowing ratio in its given routine. At that point, the system was allowed to run until steady state was reached. Once steady state was reached, three data sets were acquired for each scenario.

There were two types of data taken, film cooling and heat transfer. The first data set taken for every turbulence level was a no-blowing scenario where the holes were taped over and a cap was attached to the PVC quick disconnect instead of the flexible hose. Steady state was considered to be reached once the temperatures changed less than 0.05 °C in a ten minute time period. Three data sets were acquired with no voltage across the heater, and then the power supply was turned on. The goal for the heat transfer data sets was to have a minimum of 6 °C temperature difference between the inlet total temperature and the first row of surface thermocouples, and approximately a 20 °C temperature difference by the downstream rows. Three data sets were acquired once steady state was reached. The tape was removed from the holes for the rest of the heat transfer measurements, and the coolant system was reattached. The inlet and coolant temperatures were adjusted to be nearly identical using the heat exchangers, within ± 0.1°C of each other. Three data sets were acquired with no voltage across the heater for each increasing blowing ratio, and three were taken once the target temperature difference was reached with the power turned on. This procedure was repeated for all turbulence levels.

The air conditioning unit was turned on the night before to cool down the plates in the thermal inertia box for the film cooling data sets. The blower was also turned on and set to a low rpm to ensure the cold air was reaching the plates. The startup procedure

remained the same as the heat transfer sets, but the goal was to achieve a 10 °C temperature difference between the thermocouples in the holes and the free stream. For the 250,000 Reynolds number with M=0.55, this difference was never achieved due to the heat up of the coolant in the piping. There was no issue for the rest of the data sets. Once steady state was reached, three data sets were acquired for each blowing ratio. This process was repeated for all turbulence levels. Figures 27 and 28 are two examples of the small grid being used for holes the no blowing condition. The small grid far is shown first, followed by the small grid near.

When the IR camera data was being acquired, all other data acquisition procedures remained the same. Since the acquisition process takes about four minutes to complete, the IR data was taken at the two minute mark. For the IR data, both a physical image in the ThermaCam Researcher program and a temperature array (.csv) file were acquired for every data set taken in QuickBasic.

Figure 27. Full tunnel setup with SG2 and no blowing.

Figure 28. Full tunnel setup with SG1 and no blowing.

Future Studies

A high turbulence generator was also designed and built during this time, though it was not used in any of the film cooling testing. It was used in a stagnation region heat transfer test to expand the database of stagnation region heat transfer augmentation due to high free-stream turbulence.

A new mock combustor liner was designed to replace a previous one that created a large pressure drop. The new liner is 127 cm tall and 32.39 cm wide, with a depth of 54.94 cm. The rear wall of the mock combustor liner has eight slots on each edge that measure 2.54 wide and 14.61cm long. Each side wall contains 16 rows of two ovular plastic inserts. A drawing of the oval insert can be seen in Figure 29, and the turbulence generator can be seen in Figures 30 through 32.

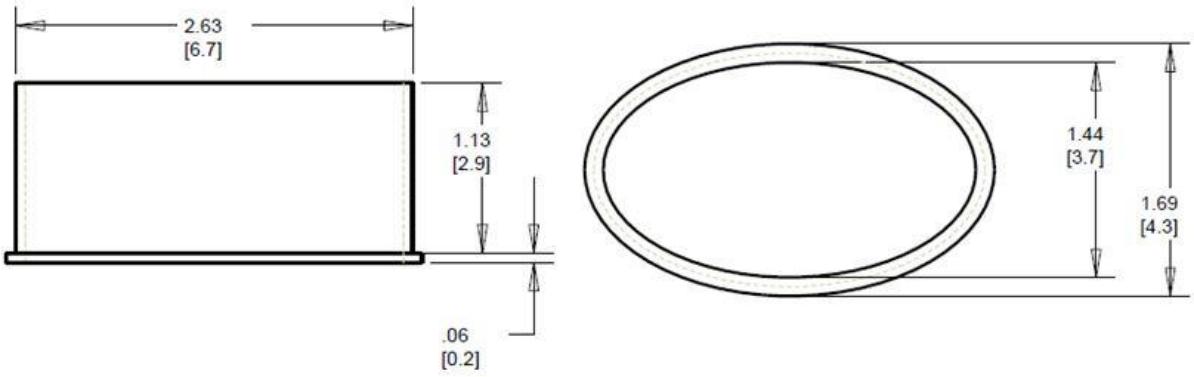

Figure 29. Oval insert for high turbulence generator dimensioned in inches [cm].

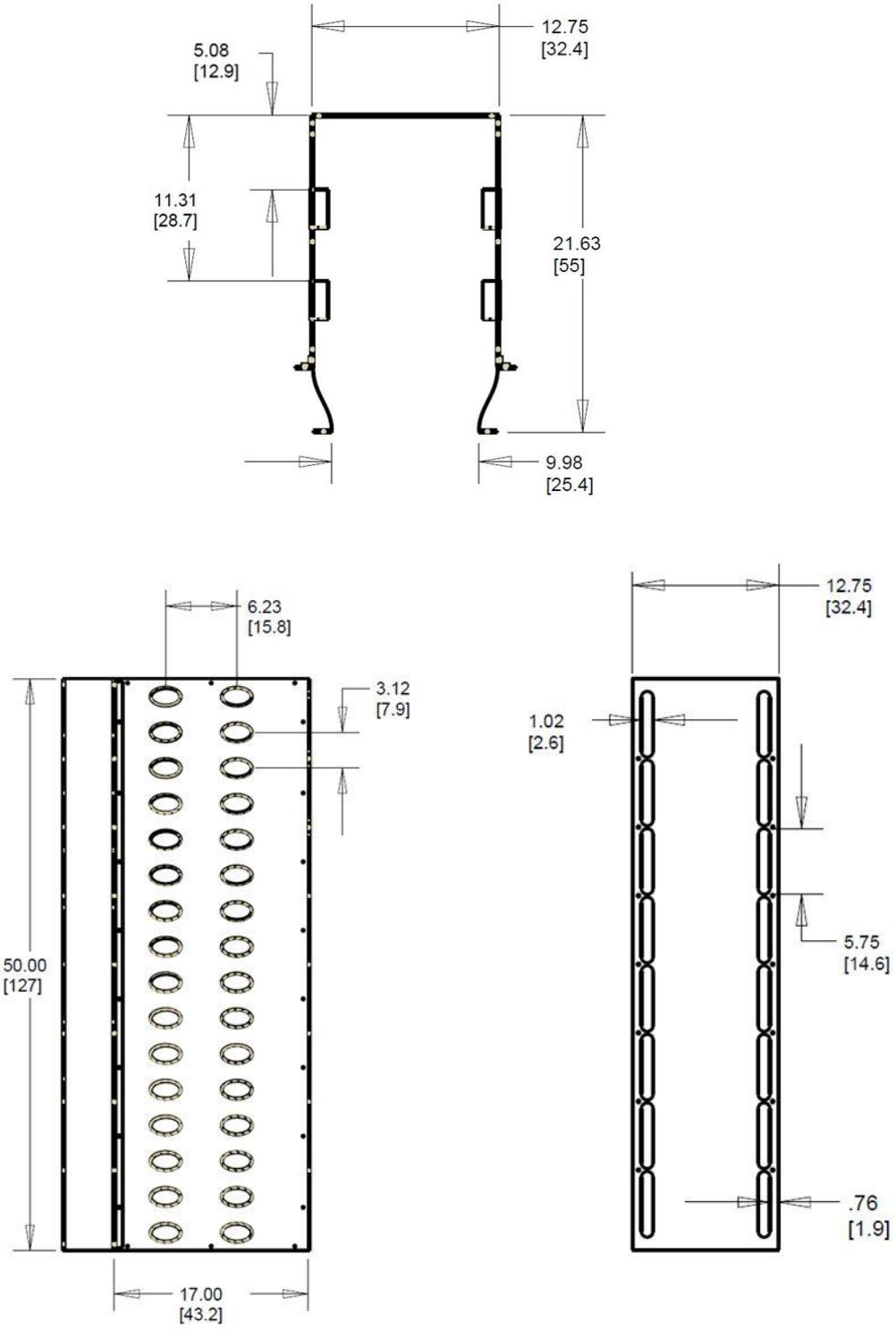

Figure 30. Dimensions of high turbulence generator mock liner in inches [cm].

Figure 31. Photos of completed turbulence generator mock liner.

Figure 32. Photos of fully completed turbulence generator.

An IFA 300 anemometer from TSI was used with a Dantec Dynamics 55P14 probe with a single hot wire to characterize the resultant turbulent flow. Measurements were taken at two streamwise locations of 7 cm and 17.1 cm from the entrance to the test section, and at three spanwise locations of 4 cm, 5 cm, and 6 cm from the far wall of the test section for each streamwise location. The flow velocities used for these measurements were nominally 5 m/s, 10 m/s, and 20 m/s. The resulting turbulence intensities from this new high turbulence generator (AH) are in the neighborhood of 17.2%-17.4%, a substantial increase over the mock aero combustor. The flow characteristics for the high turbulence generator are given in Table 3.

Table 5. High turbulence generator flow characteristics.

	U (m/s)	Tu	Lx (cm)	Lu (cm)	ε (m^2/s^3)
AH	4.89	0.1744	3.76	6.66	13.95
	9.72	0.1744	3.91	7.22	101.3
	19.34	0.1718	4.00	7.69	715.9

The film cooling study was not subjected to this high turbulence intensity, but two previous cylindrical test surfaces with 10.16 cm and 40.64 cm leading edge diameters used for stagnation region heat transfer was examined. The results show an increase in heat transfer augmentation of 26% and 52% over the aero combustor for the large and small leading edge test surfaces, respectively. These results should provide useful information for improving predictive methods and gas turbine design where high turbulence is important [40].

CHAPTER IV

EXPERIMENTAL RESULTS

This chapter will discuss the results found in the study regarding film cooling effectiveness and heat transfer on the large test cylinder with shaped holes. Both the film cooling and the heat transfer sections will include a discussion on the effects of blowing ratio, turbulence and Reynolds number. This chapter will also include a discussion on the findings of the IR camera measurements and give some insight into the coverage of the coolant when it is ejected from shaped holes. Finally, since this test cylinder was previously used in a study on slot film cooling under nearly identical conditions of turbulence and coolant flow rates, a comparison will be made between the shaped holes and slot film cooling regimes on their performance both near the front and at downstream locations.

Large Cylinder with Shaped Holes—Adiabatic Effectiveness

Effects of Blowing Ratio

The effects of blowing ratio (M) are quite large on the adiabatic effectiveness. For all turbulence cases, there was a sharp drop in effectiveness after the first row of thermocouples with the blowing ratio of M=0.55 dropping the most quickly. For all cases except the low turbulence nozzle (LT), the difference in effectiveness between the highest and lowest blowing ratios was at least $\Delta\eta$=0.20 by a surface distance of 25 hole

diameters. This difference stayed for the majority of the test surface, dropping to around $\Delta\eta$=0.10 at the end of test surface for most of the cases. Figure 33 shows the low turbulence case with increasing blowing ratios. The difference at 25 diameters between the high and low blowing ratios is around $\Delta\eta$=0.15, and that value falls only to 0.12 downstream. The increase in effectiveness from M=0.55 to M=0.97 is very large, but the gain seen by M=1.35 is much less, indicating the flow regime is nearing penetration. Increasing the blowing ratio to 1.89 results in effectiveness levels lower than for M=0.97, suggesting there is significant penetration occurring. Figure 34 shows the change in effectiveness when the small grid far turbulence level is applied. For this case, the difference at 25 diameters is nearly $\Delta\eta$=0.21 and falls to about 0.10 downstream. Again, there is a large gain in effectiveness levels over the low blowing ratio with M=0.97. The blowing rate of 1.35 shows a larger increase over the 0.97 condition at this turbulence level when compared the LT condition, and the high blowing ratio is very similar to it for the duration of the surface. Figure 35 shows the change in effectiveness when the large grid turbulence level is applied. Here, the difference in effectiveness at 25 diameters downstream is just over $\Delta\eta$=0.22, and only about 0.07 downstream. This figure also shows that after a distance of about 60 diameters, all of the blowing ratios appear to be equally spaced which shows the importance of mass addition at higher turbulence levels. Finally, Figure 36 shows the change in effectiveness when the aero combustor turbulence level is applied. For this high of turbulence, all blowing ratios had effectiveness levels below 10% by a distance of 75 diameters, showing the rapid growth of the boundary layer and rapid dissipation of effectiveness as the coolant is mixed into the boundary layer.

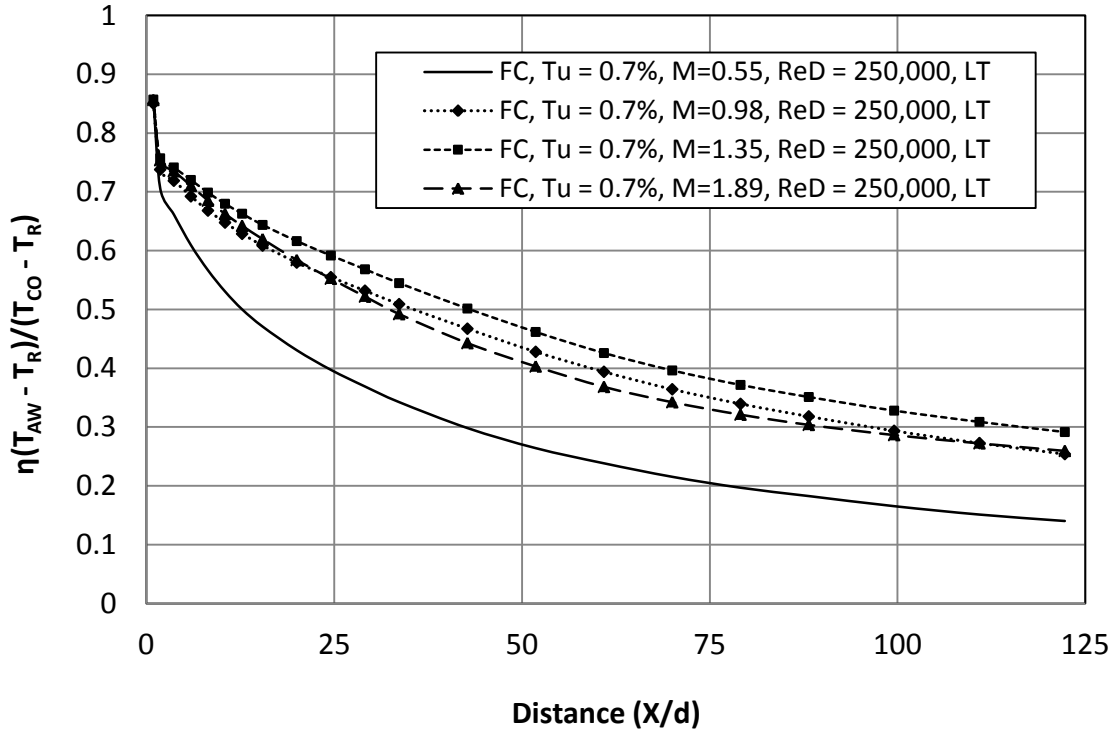

Figure 33. Adiabatic film cooling with LT nozzle Tu at ReD=250k and varying M.

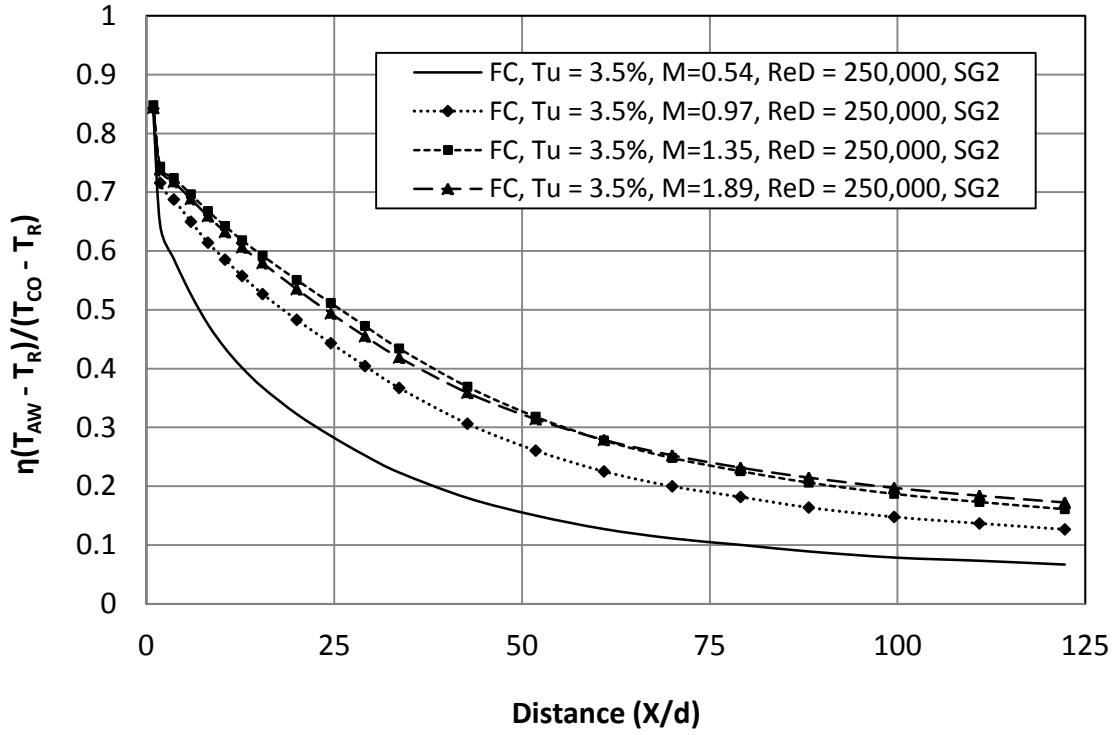

Figure 34. Adiabatic film cooling with small grid far Tu at ReD=250k and varying M.

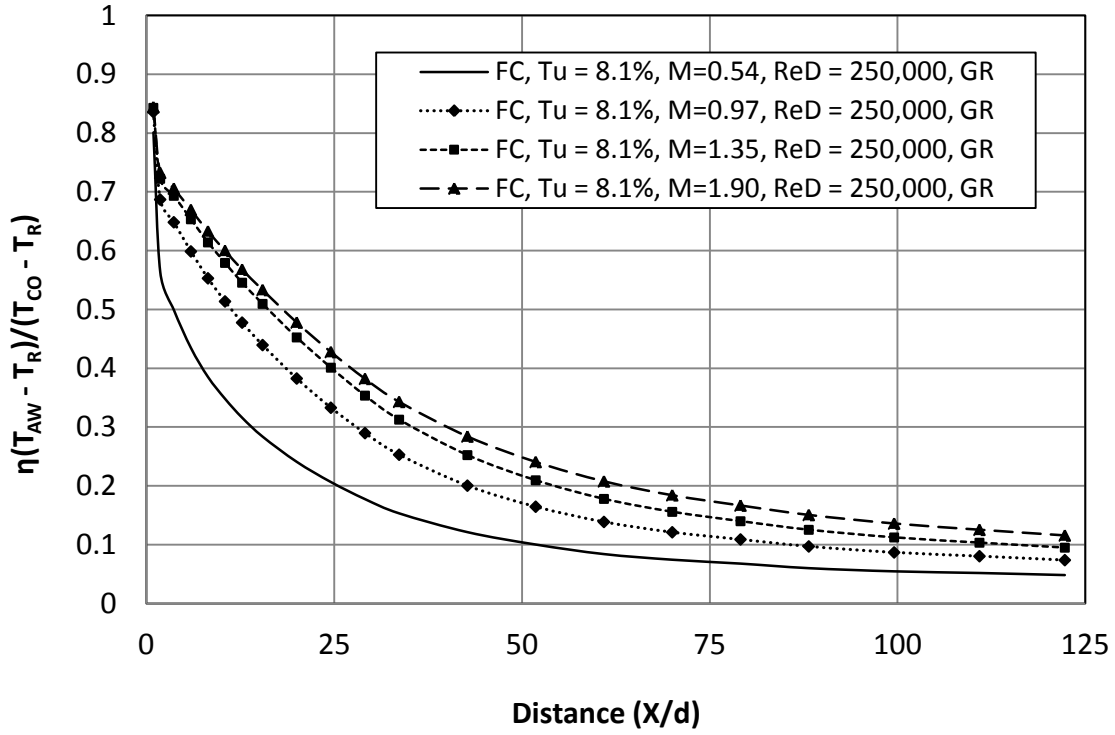

Figure 35. Adiabatic film cooling with large grid Tu at ReD=250k and varying M.

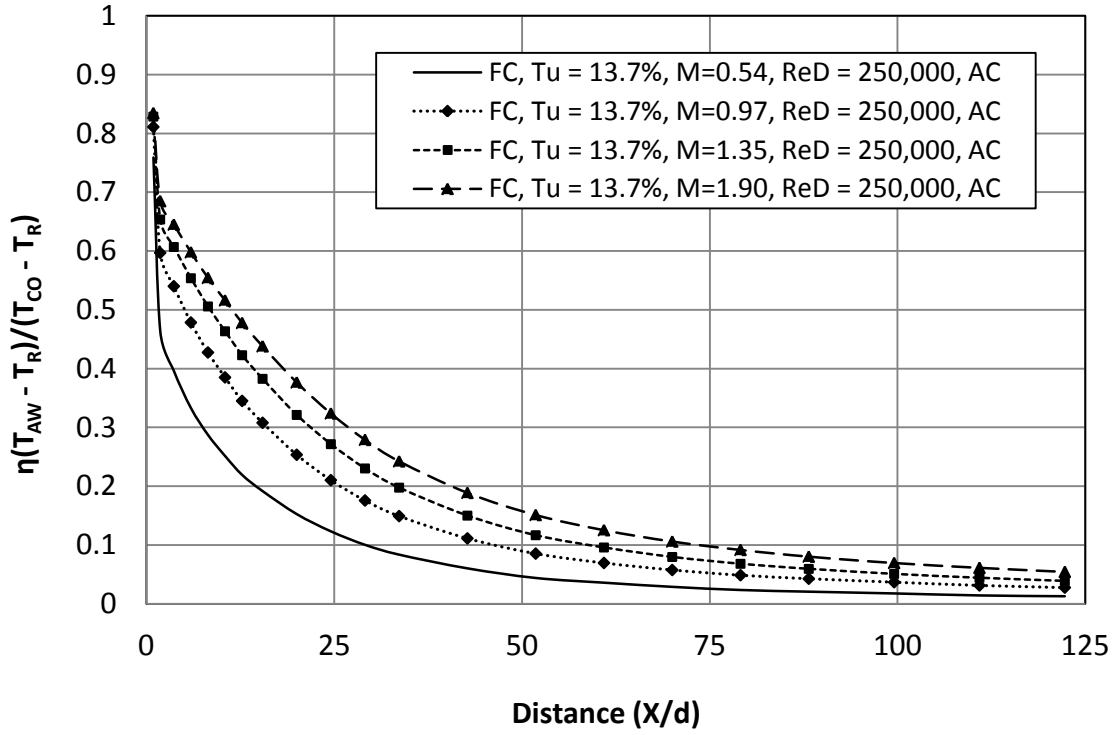

Figure 36. Adiabatic film cooling with aero combustor Tu at ReD=250k and varying M.

Effects of Turbulence

Turbulence has a very strong influence on adiabatic effectiveness—as turbulence increases, effectiveness decreases. The difference in effectiveness appears to order on intensity as each increasing turbulence case shifts the line down. As shown in Figures 37 to 42, the small grid near, large grid, and aero combustor with spool turbulence cases appear to group together, while the others are more spread out. In Figure 37 with M=0.54, all of the turbulence levels drop the effectiveness below 30% by a distance of about 42 hole diameters, and five of those fall below 30% by 25 hole diameters. In Figure 38 with M=0.97, the disparity in effectiveness grows to over 0.35 between the high and low turbulence intensities. Even downstream, the difference is around 0.22 for this blowing ratio. Figure 39 shows the effects of increasing turbulence with a blowing ratio of M=1.35. Again, a large difference is seen between the high and low turbulence cases, with a $\Delta\eta$=0.25 difference in effectiveness seen downstream. The high blowing ratio of M=1.90 yields results very similar to the one before it. In Figure 41 we see the effects turbulence has on the 500,000 Reynolds number with low blowing ratio. An effectiveness of 30% is achieved around 7 hole diameters for the aero combustor case and around 34 diameters for the LT nozzle case. At the higher blowing ratio in Figure 42, the LT nozzle case achieves 30% effectiveness about 100 diameters downstream, while the aero combustor case achieves it around 13 diameters downstream. This shows just how rapidly the turbulence is causing the boundary layer to grow and mix the coolant away from the surface.

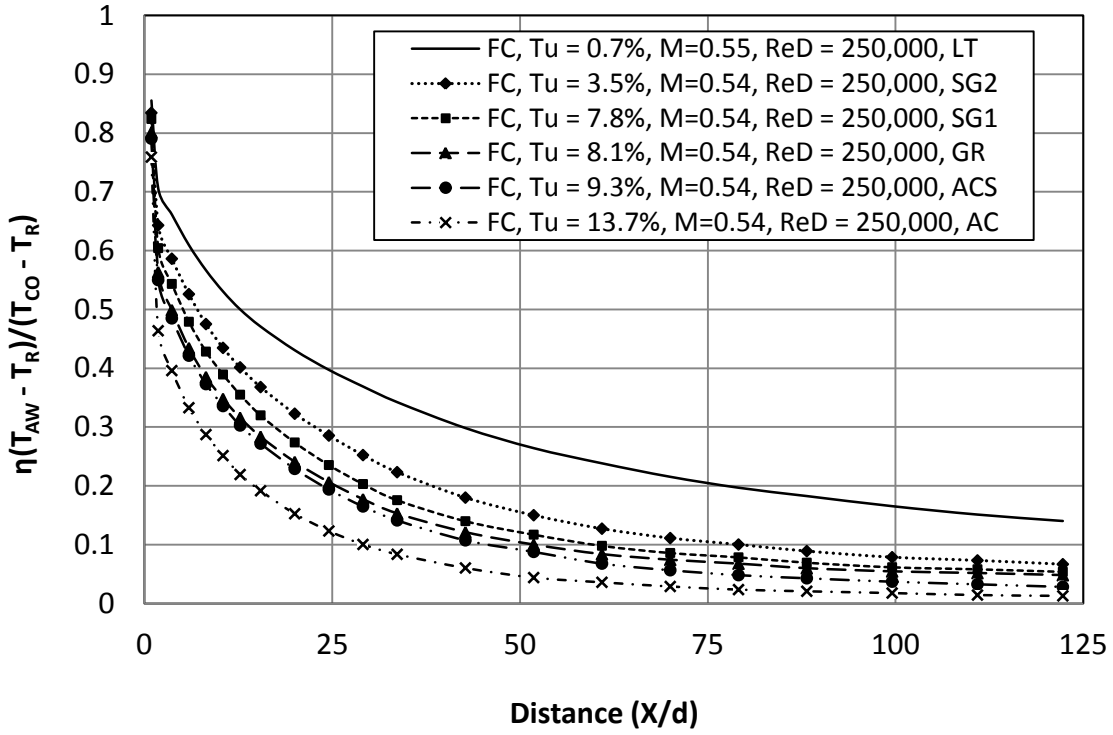

Figure 37. Adiabatic film cooling with varying Tu levels at ReD=250k and M=0.54.

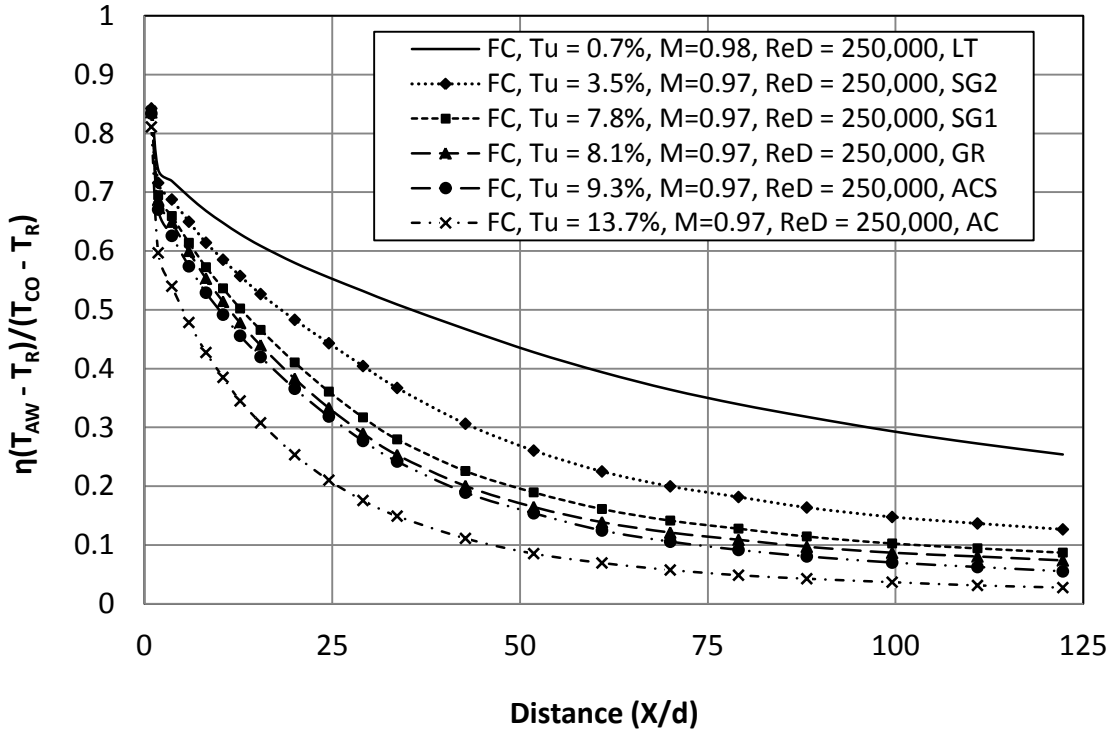

Figure 38. Adiabatic film cooling with varying Tu levels at ReD=250k and M=0.97.

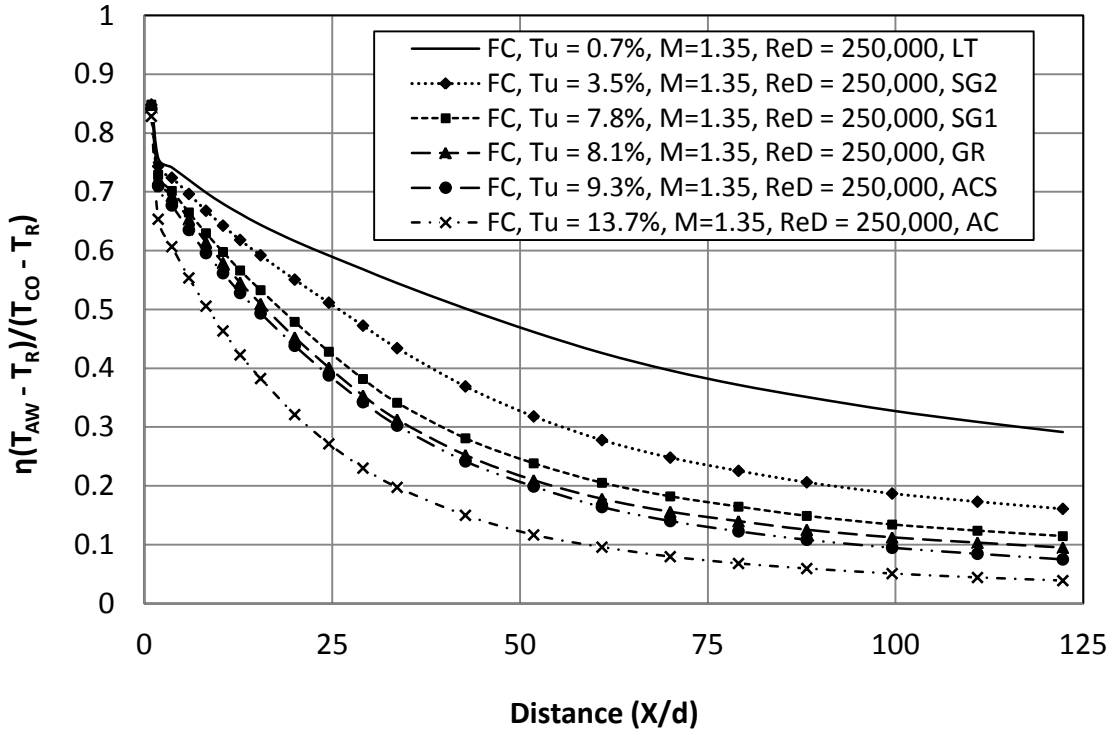

Figure 39. Adiabatic film cooling with varying Tu levels at ReD=250k and M=1.35.

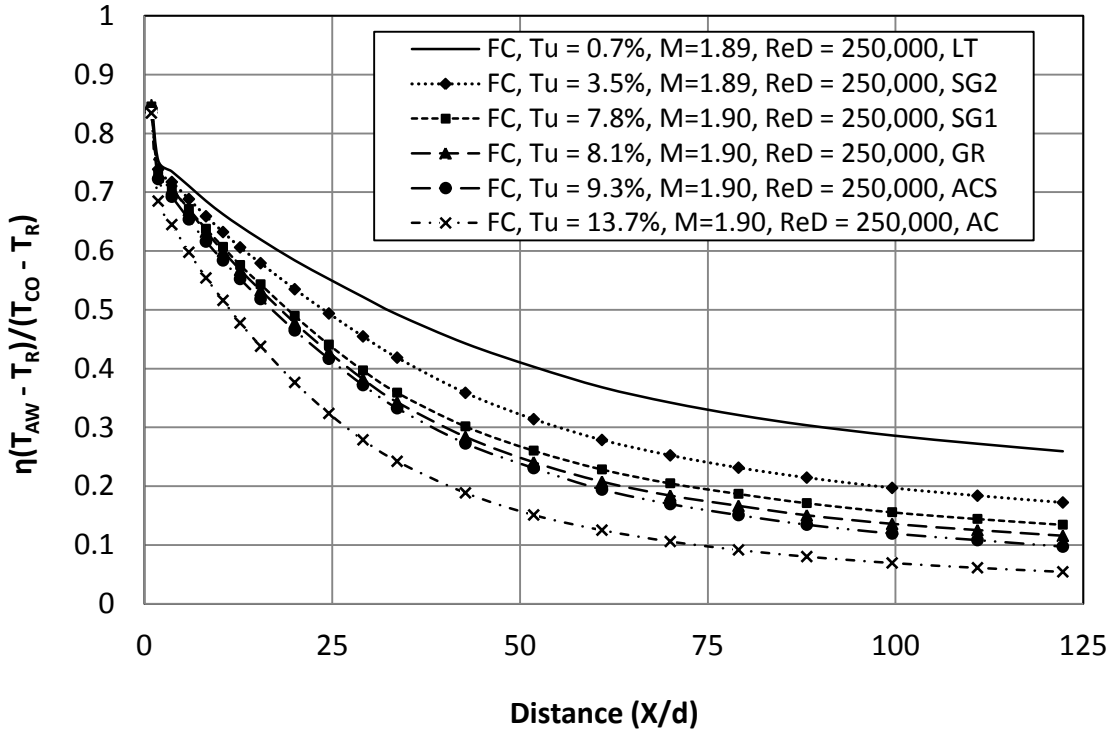

Figure 40. Adiabatic film cooling with varying Tu levels at ReD=250k and M=1.90.

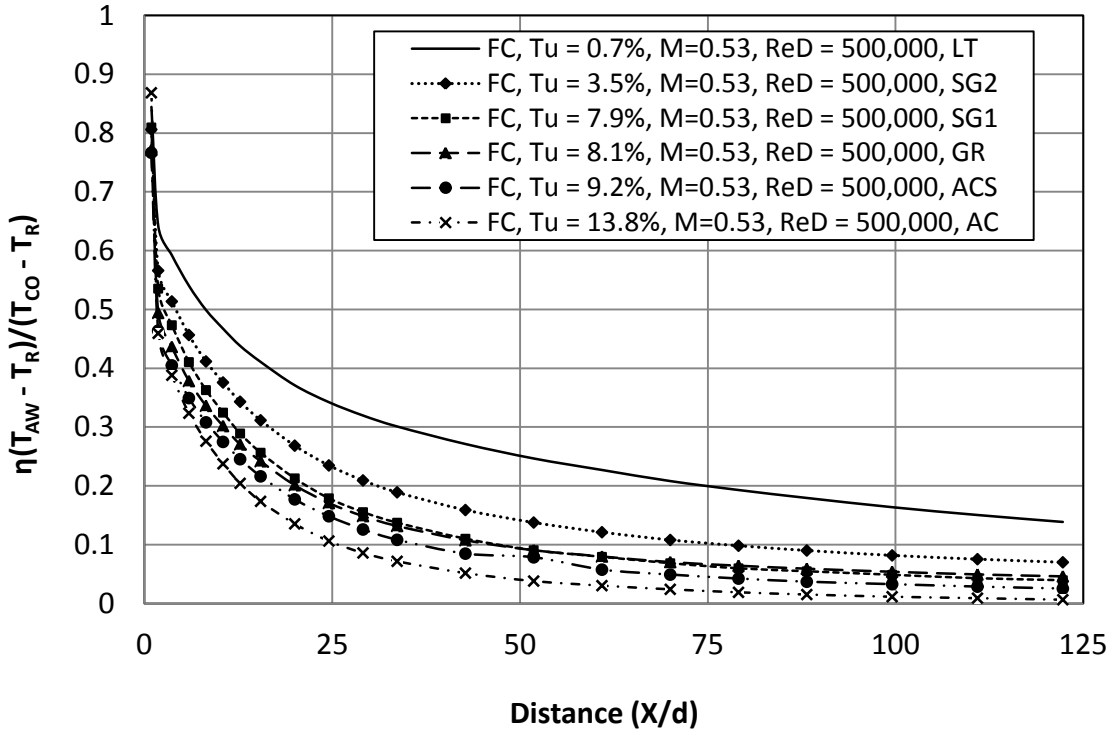

Figure 41. Adiabatic film cooling with varying Tu levels at ReD=500k and M=0.53.

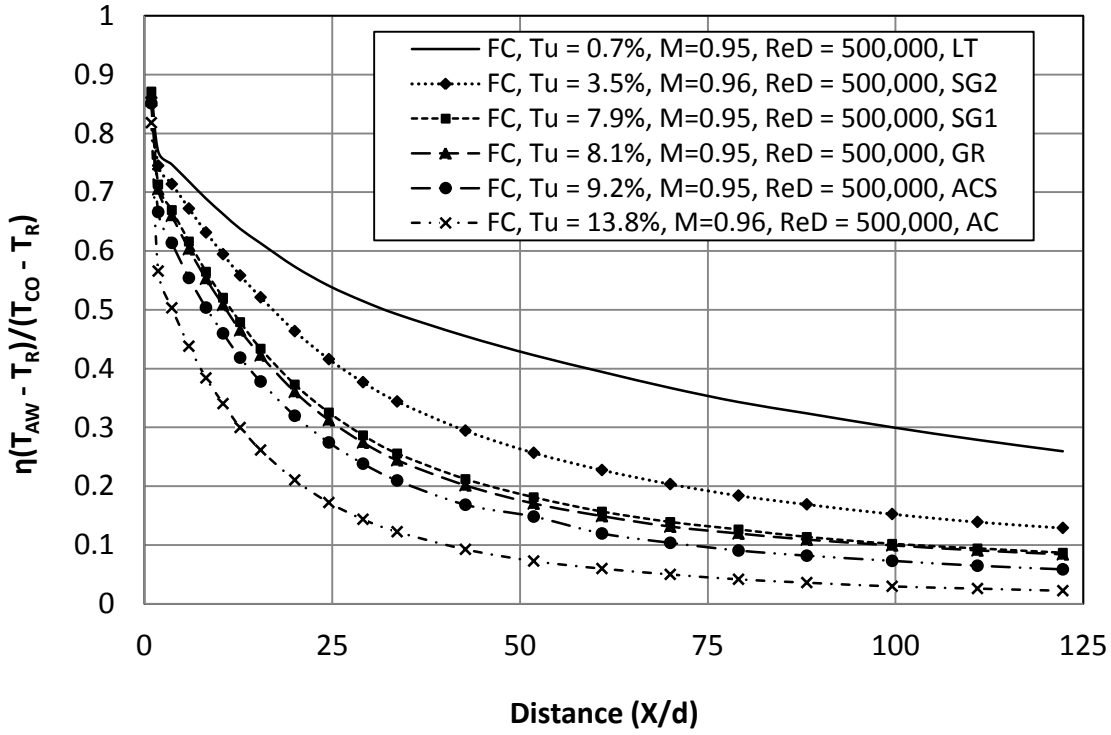

Figure 42. Adiabatic film cooling with varying Tu levels at ReD=500k and M=0.95.

Effects of Reynolds Number

Shaped hole film cooling can generally be understood in terms of an energy sink model where the injected film cooling is essentially mixed across a developing boundary layer. Normally, higher Reynolds numbers would be expected to produce better film cooling than lower Reynolds numbers since boundary layers are expected to be thinner. However, the current study shows the lower Reynolds number to have enhanced film cooling over the higher Reynolds number due to the high acceleration, causing a longer transitional region that inhibits boundary layer growth. This study also shows that Reynolds number has by far the smallest effect on adiabatic effectiveness. As seen in Figures 43 to 45, the largest differences occur before a distance of 50 hole diameters which would suggest the high Reynolds number cases exhibiting earlier transition than the lower Reynolds number cases. In Figure 43 we see the largest effect on the low blowing ratio with low turbulence intensity. Here, an effectiveness level of 30% was reached at 33 and 42 hole diameters for the high and low Reynolds numbers, respectively. However, after a distance of 75 diameters, the two lines are nearly indistinguishable. At the higher blowing ratio, the two lines are almost identical, with no more than 3% difference after only three hole diameters. This would show the state of the boundary layer at both velocities to be nearly identical. At the large grid turbulence level in Figure 44, there is little disparity between the low and high Reynolds numbers, though the high Reynolds number case appears to transition earlier. The low blowing ratio values are nearly identical after about 60 hole diameters. The high blowing ratio curves are very close, with a difference of less than 2% for the entire length. Finally, the effects of Reynolds number can be seen for the high turbulence case in Figure 45. Here,

there is more variation between the corresponding values for the high blowing ratio, with about a 4% difference at 25 hole diameters. Little difference exists for the low blowing rate.

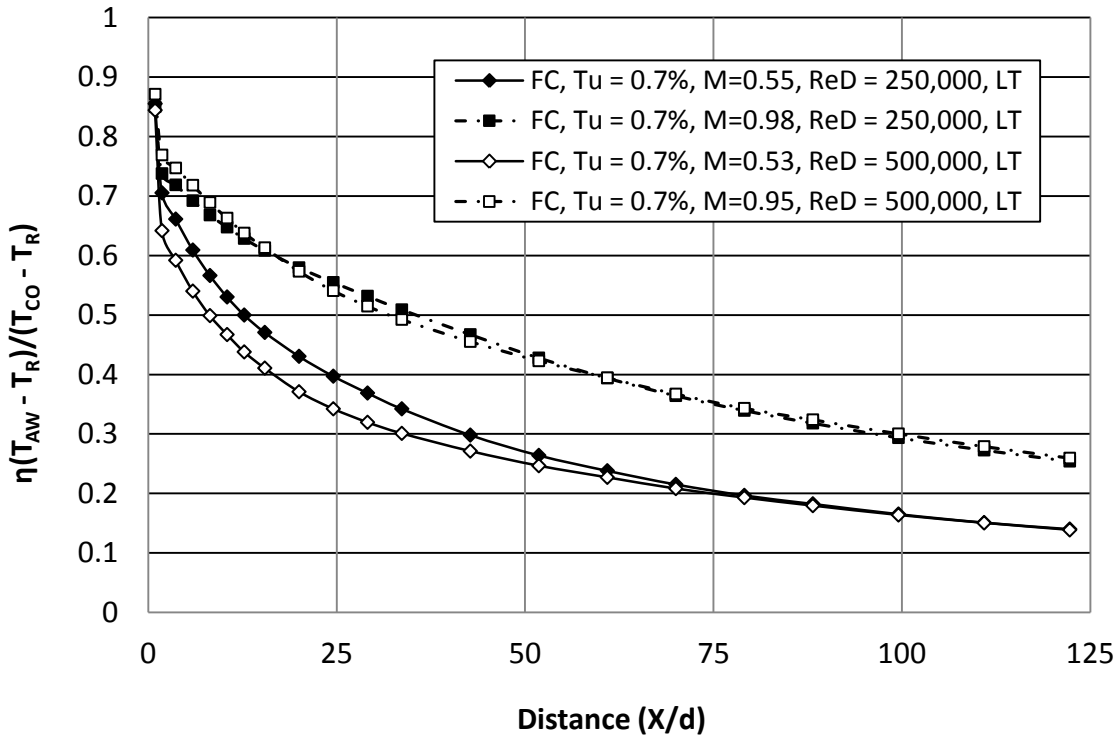

Figure 43. Adiabatic film cooling comparison of high-low ReD at LT nozzle Tu.

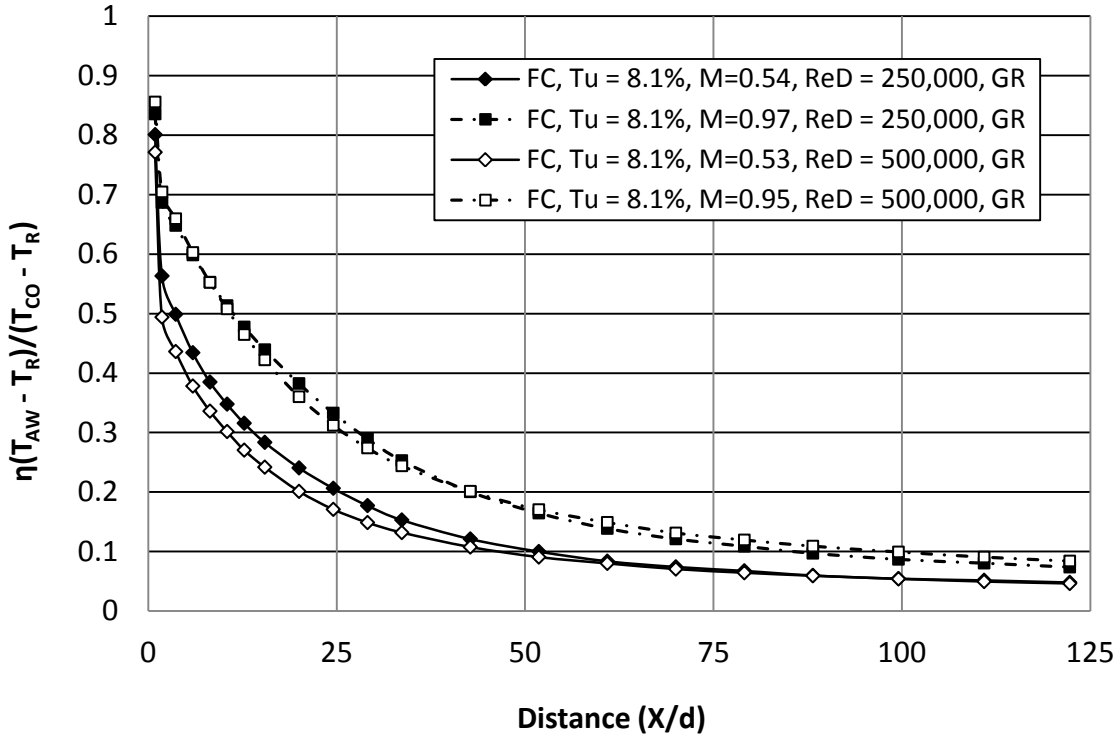

Figure 44. Adiabatic film cooling comparison of high-low ReD at large grid Tu.

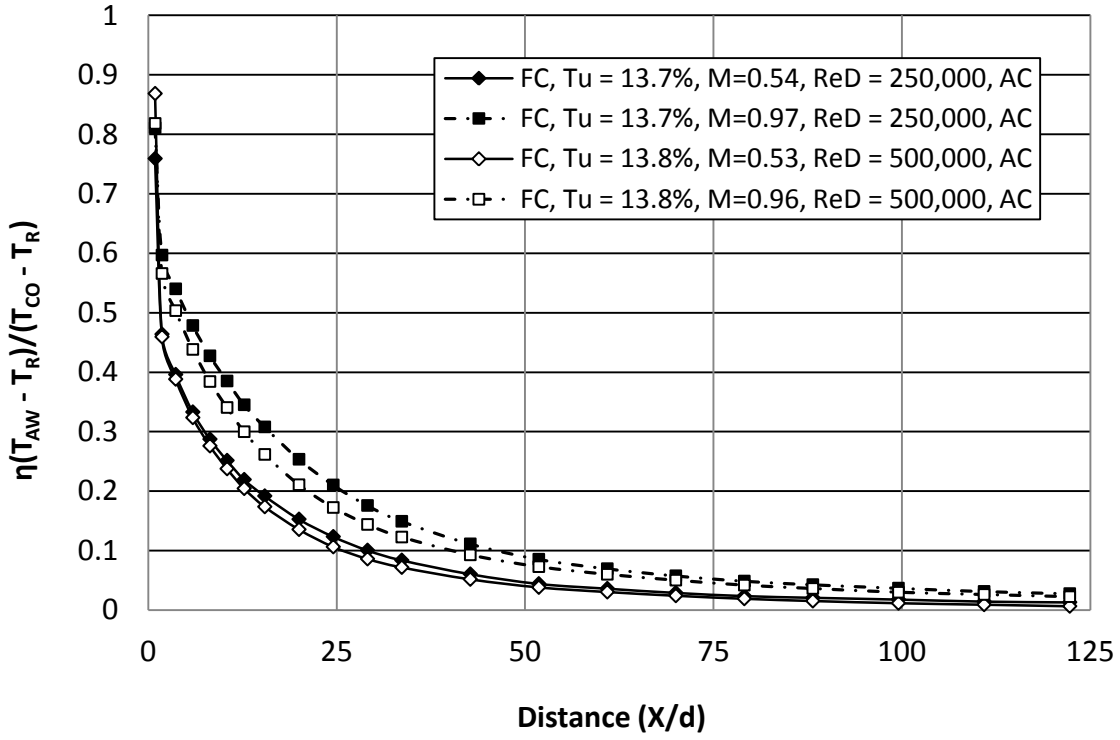

Figure 45. Adiabatic film cooling comparison of high-low ReD at aero combustor Tu.

Effects of Blowing Ratio

Heat transfer increases as blowing ratio increases, and the greatest values of heat transfer were generally achieved when M=1.90. The no blowing cases most commonly resulted in the lowest heat transfer values. The beginning of the test surface exhibited the highest values for Stanton number, likely due to the unheated starting length of the stagnation region. Most blowing ratios showed a large drop in heat transfer with the minimum value occurring near 25 hole diameters, followed by a small recovery and relatively constant values for the latter half of the test section. This drop and recovery shows the transitional state of the boundary layer. The no blowing case appears to stay laminar for the duration of the surface at the low turbulence level in Figure 46. Interestingly, the two blowing ratios with the highest heat transfer were 1.90 and 0.55, indicating a shearing effect at the low blowing ratio due to the low fluid momentum in the low turbulence flow. The high blowing ratio has increased heat transfer immediately after the ejections holes, with a 49% increase over the holes taped scenario in Figure 46. In Figure 47 we see the effects of blowing at the small grid far turbulence condition. Here, there is a tighter grouping throughout the length of the test surface, and the four blowing ratios appear to transition by a distance of 60 diameters. The no blowing condition stays laminar for much of the surface distance, and appears to transition right near the end where the maximum difference in Stanton number is only 0.000024. The turbulence was increased with the large grid in Figure 48, and the differences in heat transfer curves continue to decrease. After 75 hole diameters, the five curves appear to essentially become a single curve, with an average difference of 0.000026 across the final

40 hole diameters. With the high turbulence level shown in Figure 49, there is very little distinction between curves for most of the test surface. The difference between the four blowing ratios is down to 0.000096 at 25 hole diameters, and the five curves again appear to become one after a distance of about 50 hole diameters. For the section of $50 < X/d < 125$, the average difference between the five curves is 0.000030. These figures suggest that blowing ratio effects lessen as the boundary layer transitions, and are severely lessened as turbulence intensity increases.

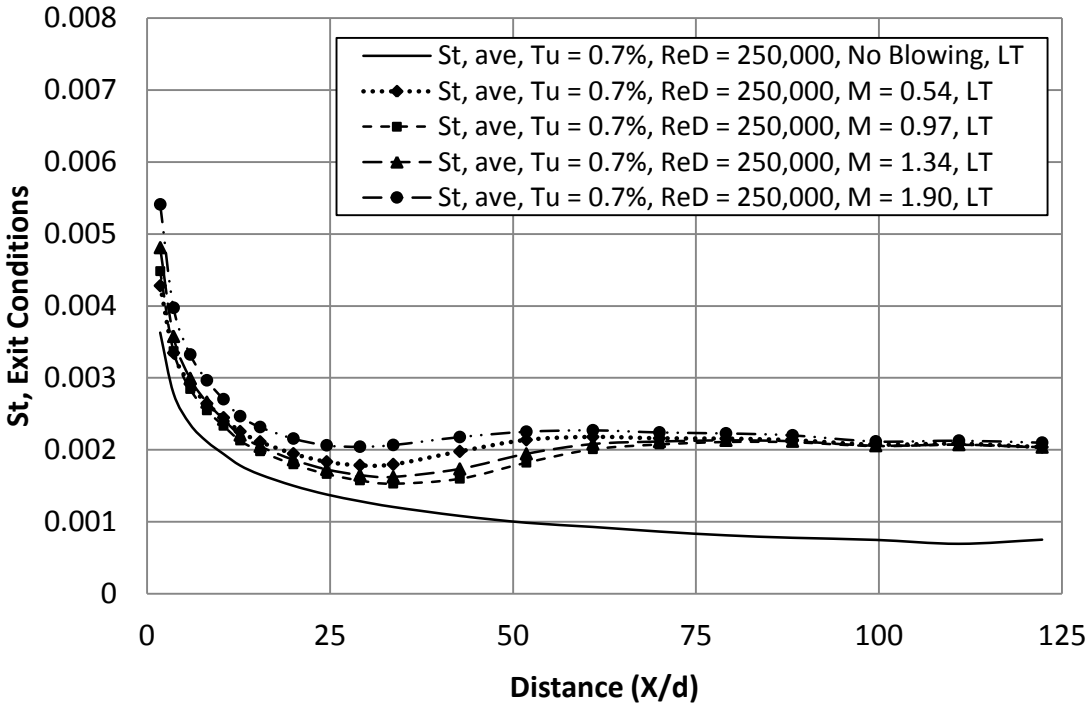

Figure 46. Stanton number with varying blowing ratios at ReD=250k, LT nozzle Tu.

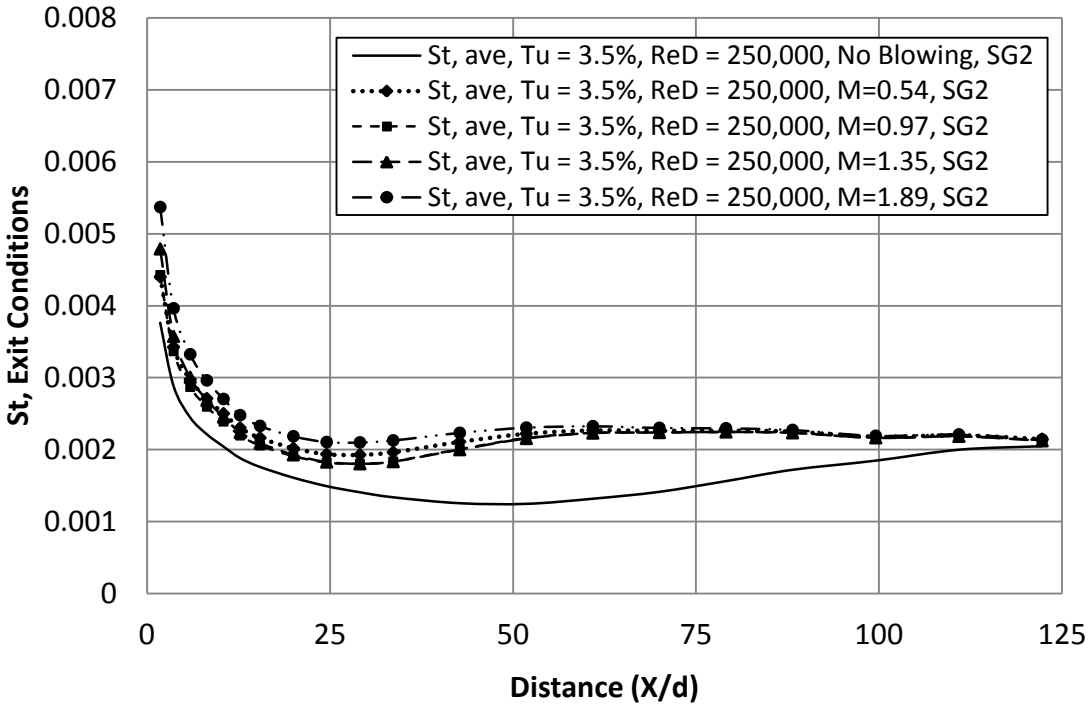

Figure 47. Stanton number with varying blowing ratios at ReD=250k, small grid far Tu.

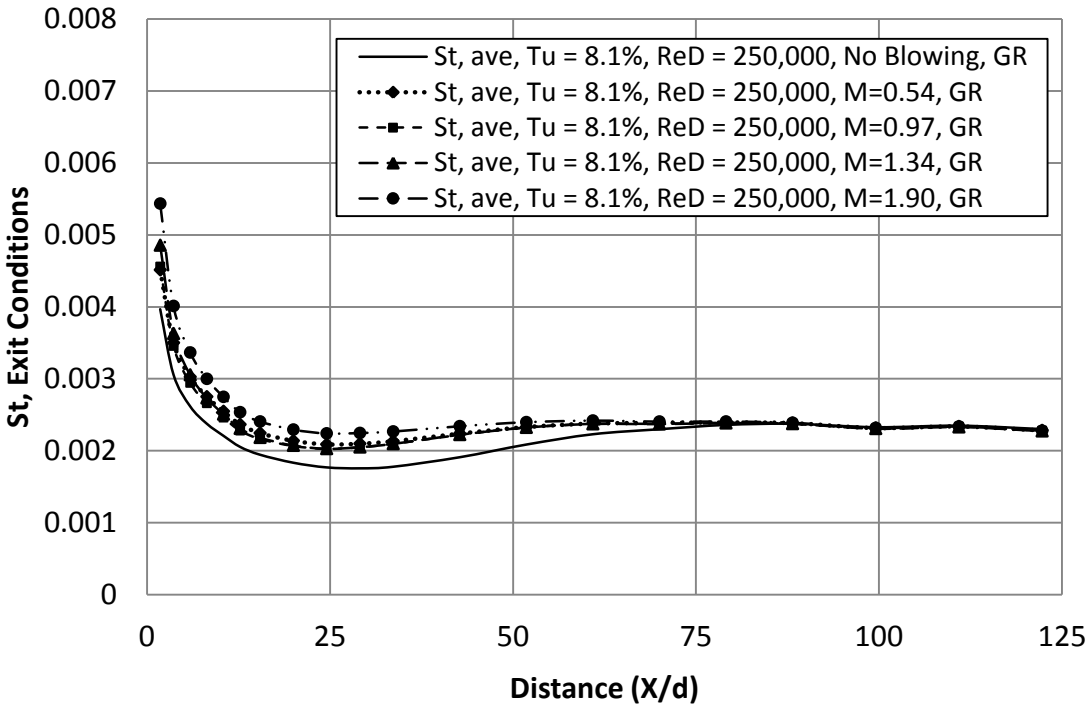

Figure 48. Stanton number with varying blowing ratios at ReD=250, large grid Tu.

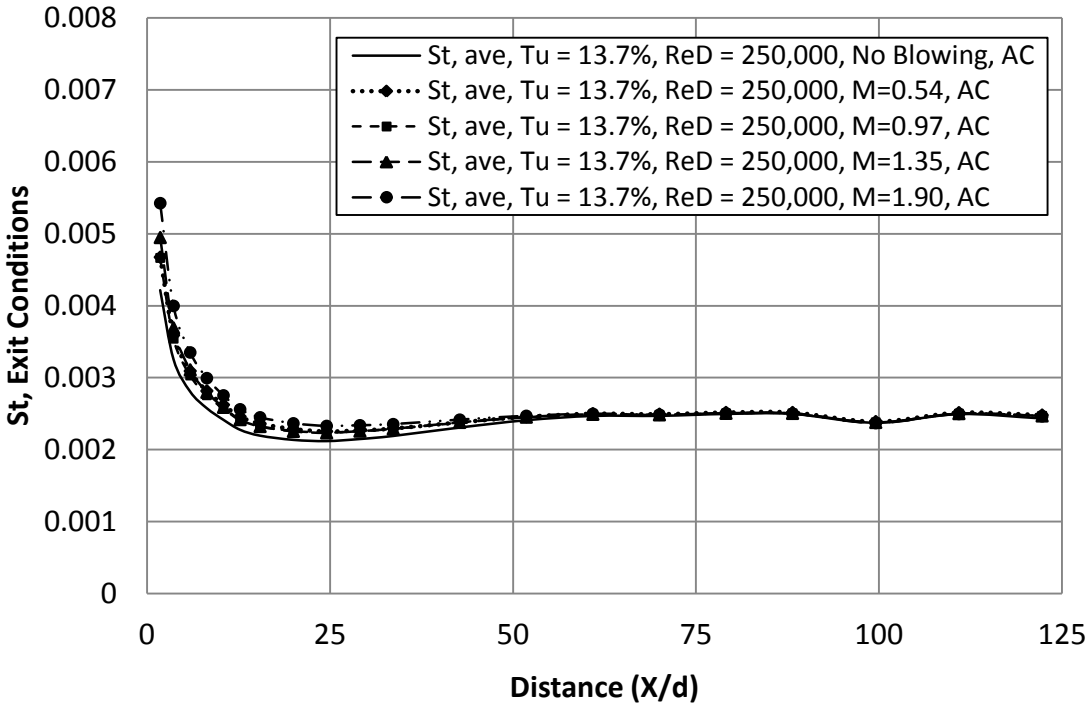

Figure 49. Stanton number with varying blowing ratios at ReD=250k, aero combustor Tu.

Effects of Turbulence

Turbulence has a strong impact on surface heat transfer, with the most pronounced effects occurring on the no blowing condition. This condition can be seen in Figure 50. Here, the difference in Stanton number at the end of the foil is around three times larger than at the beginning. The decrease in transition length can be seen quite easily with the low turbulence condition appearing to stay laminar for the entire length, the small grid far condition transitioning very slowly, and the higher turbulence conditions transitioning more and more quickly with increasing turbulence intensity. The increase in heat transfer appears to order on turbulence level for the no blowing condition, similar to the way film cooling effectiveness decreases order on turbulence level. In Figure 51 the effects of turbulence are seen on the low blowing ratio for the 250,000 Reynolds number. Again, the transition region appears to get smaller and move toward the leading edge of the test surface as turbulence intensity increases. It is also interesting to note that the grouping is tighter for the low blowing ratio than for M=1.35 in Figure 52. This is likely due to the shearing effect as discussed previously. The high blowing ratio in Figure 53 has the tightest grouping of the low Reynolds number conditions, showing that at this blowing ratio, the boundary layer quickly transitions at all turbulence intensities. Figures 54 and 55 show the effects of turbulence at the high Reynolds number. In both cases we see a transition around a distance of 15 hole diameters and again, very little difference between turbulence levels. This early transition helps to explain the better performance of the lower Reynolds number over the higher in the film cooling comparisons.

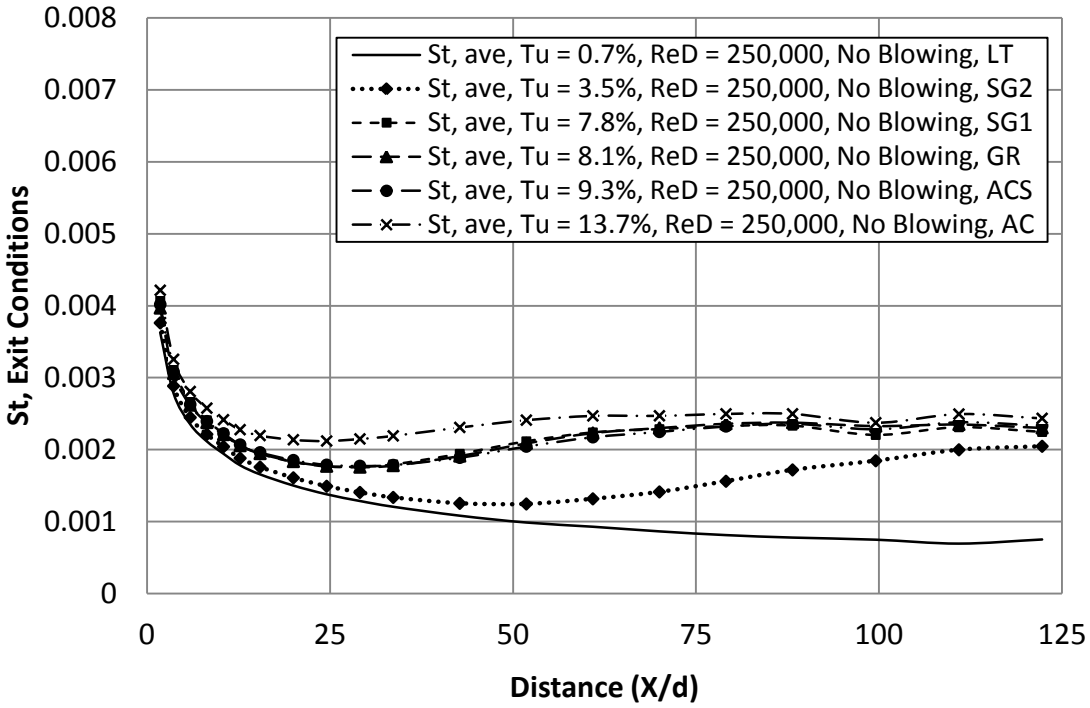

Figure 50. Stanton number with varying turbulence at ReD=250k with holes taped.

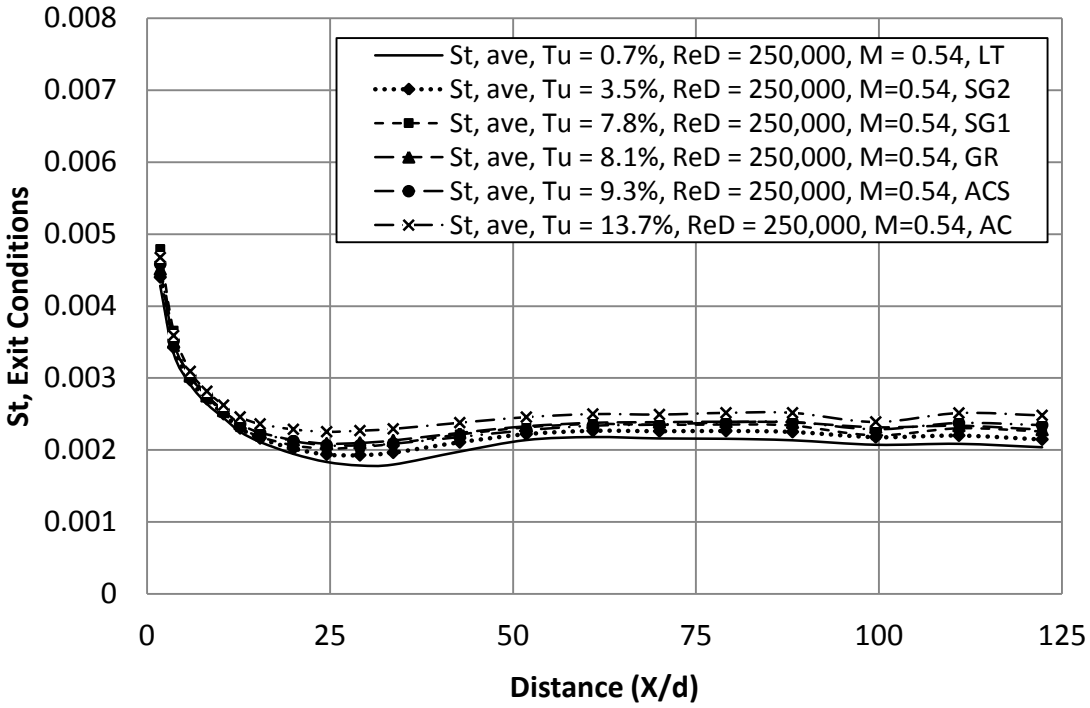

Figure 51. Stanton number with varying turbulence at ReD=250k with M=0.54.

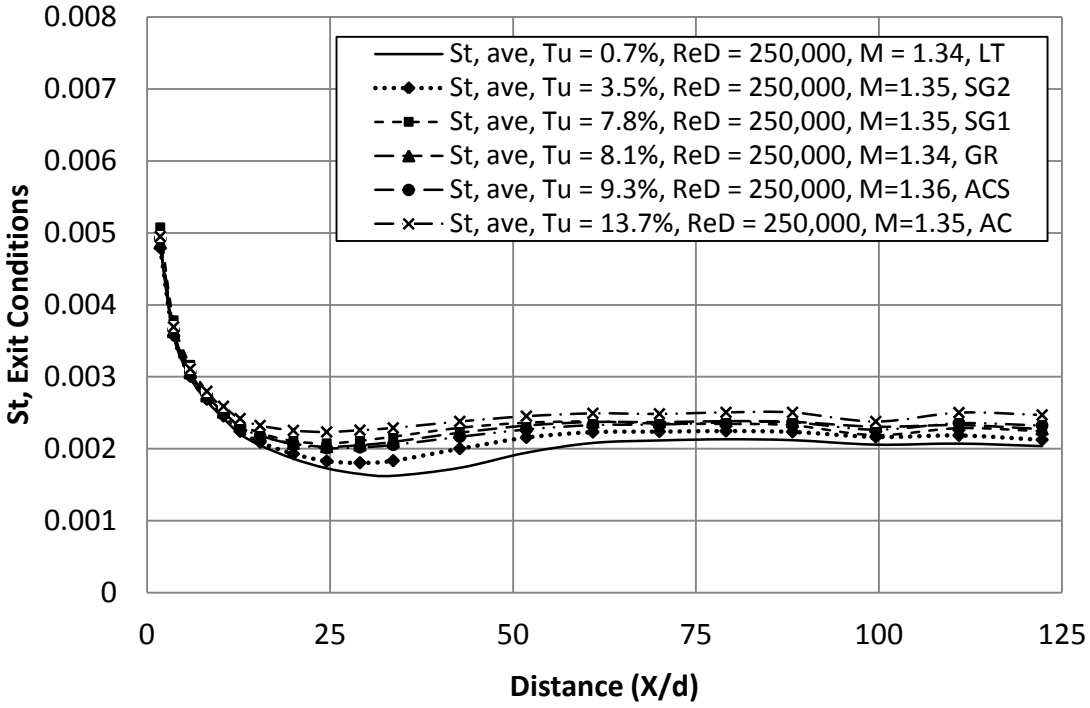

Figure 52. Stanton number with varying turbulence at ReD=250k with M=1.35.

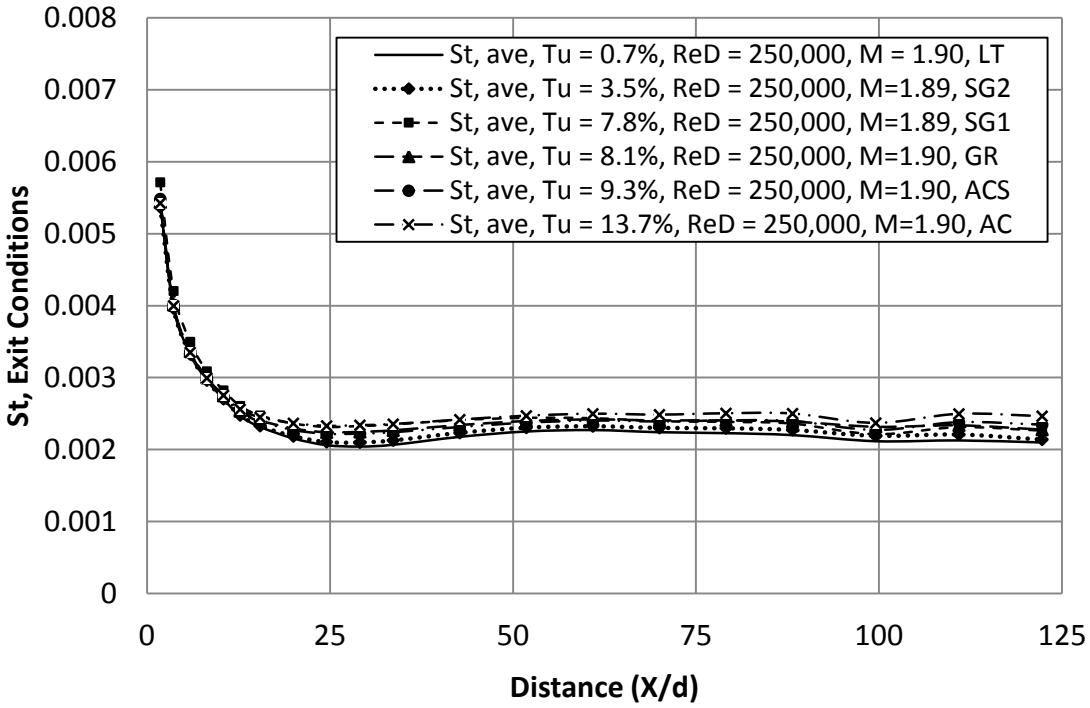

Figure 53. Stanton number with varying turbulence at ReD=250k with M=1.90.

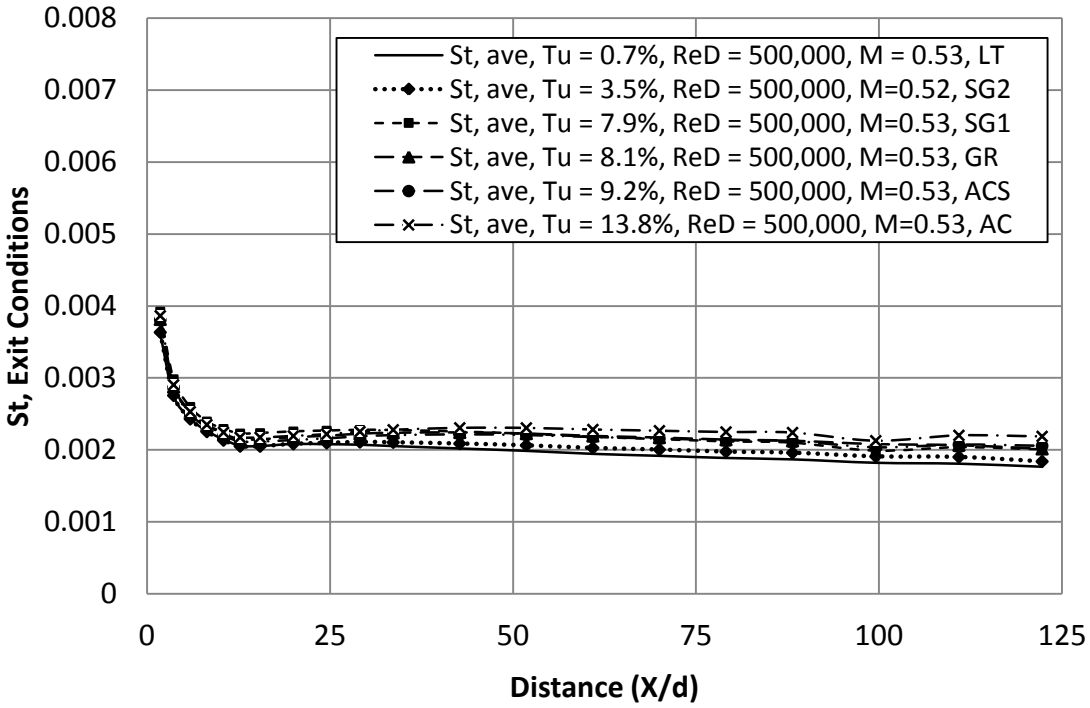

Figure 54. Stanton number with varying turbulence at ReD=500k with M=0.53.

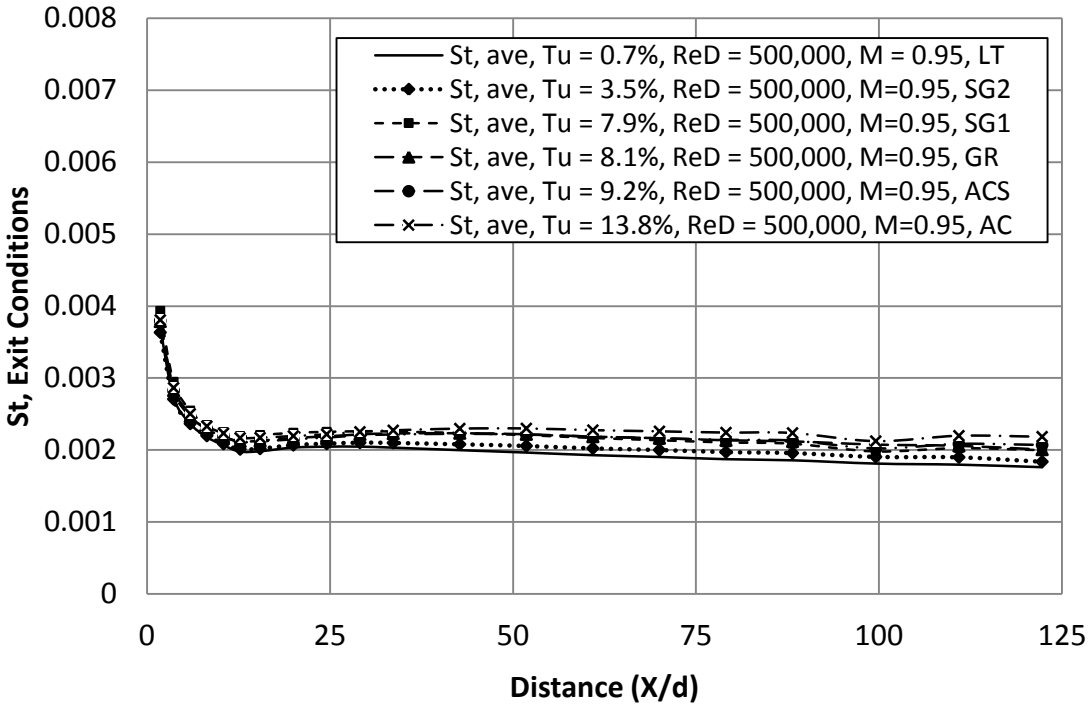

Figure 55. Stanton number with varying turbulence at ReD=500k with M=0.95.

Effects of Reynolds Number

The effects of Reynolds number become clearer as the blowing ratio and turbulence are increased. Figure 56 shows the Stanton number comparisons for the high and low Reynolds numbers with low turbulence. Early on, the low Reynolds number gives significantly higher heat transfer for all three blowing conditions due to the laminar flow and unheated started length. For the no blowing condition, this trend continues until a distance of about 60 hole diameters. At the low blowing ratio, the high Reynolds number has higher Stanton number values than the low Reynolds number due to the turbulent flow in the region of $20 < X/d < 43$ before switching back as the low Reynolds number case begins to complete transition. The high blowing ratio has a similar behavior in a slightly larger region of $15 < X/d < 52$. Increasing the turbulence to the small grid far level, we see a similar behavior in Figure 57. These both show the larger transition region for the lower Reynolds number conditions and help to explain the improved film cooling performance at the lower Reynolds number. The small grid near turbulence level data in Figure 58 shows nearly the same trends as the aero combustor in Figure 59. In Figure 59 we see that at the high turbulence level, however, the only time the high Reynolds number gives higher Stanton number values is at the no blowing condition between 20 and 34 hole diameters downstream. The two blowing ratios at the low Reynolds number give about 15% higher transfer in the immediate region and around 10% higher values for the latter half of the test section. The behavior of these curves show the higher Reynolds number causes an earlier transition which produces slightly higher heat transfer momentarily. The low Reynolds number cases exhibit higher heat transfer at given turbulence levels once transition has occurred.

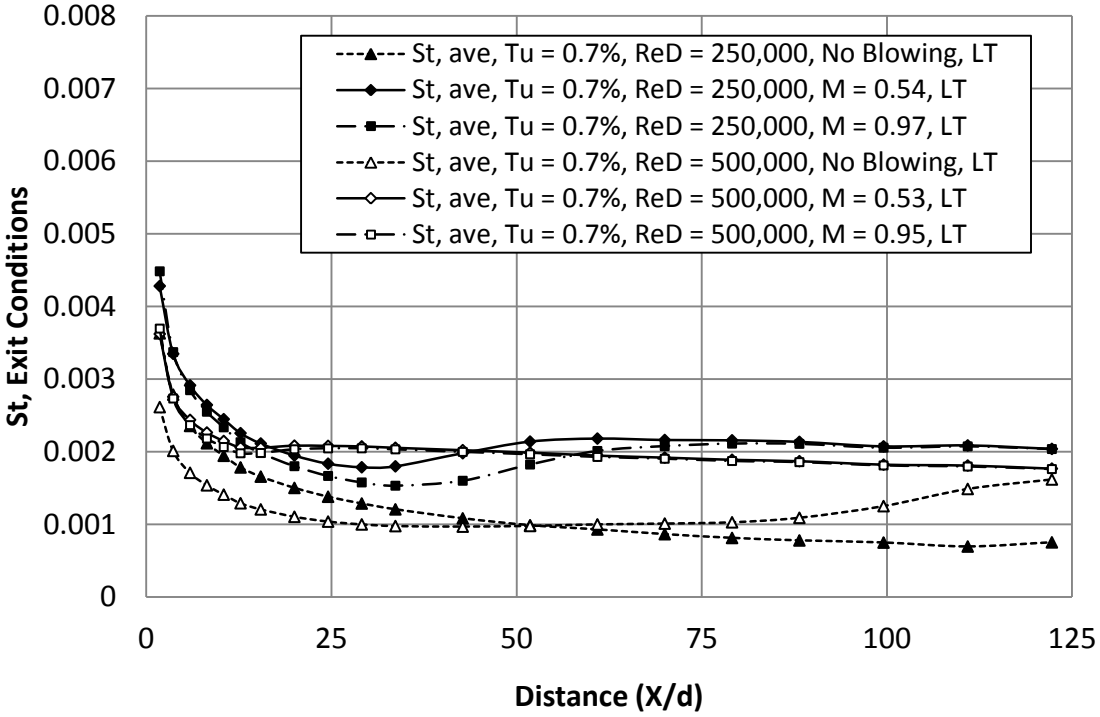

Figure 56. Stanton number comparison of high-low ReD at low turbulence Tu.

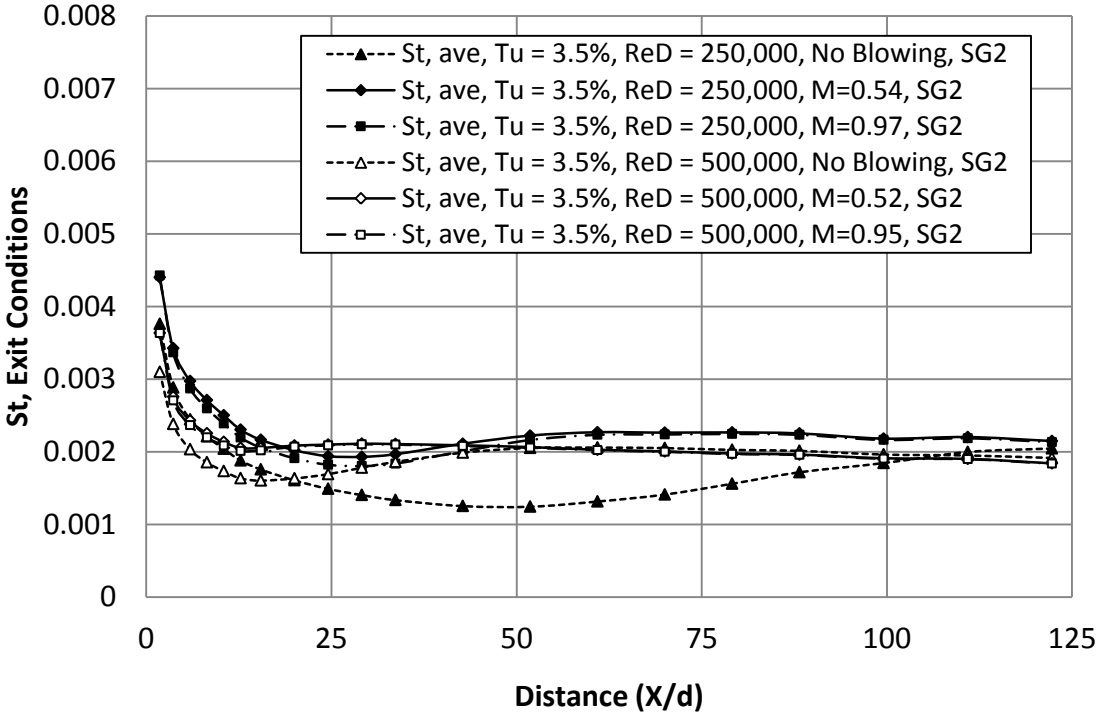

Figure 57. Stanton number comparison of high-low ReD at small grid far Tu.

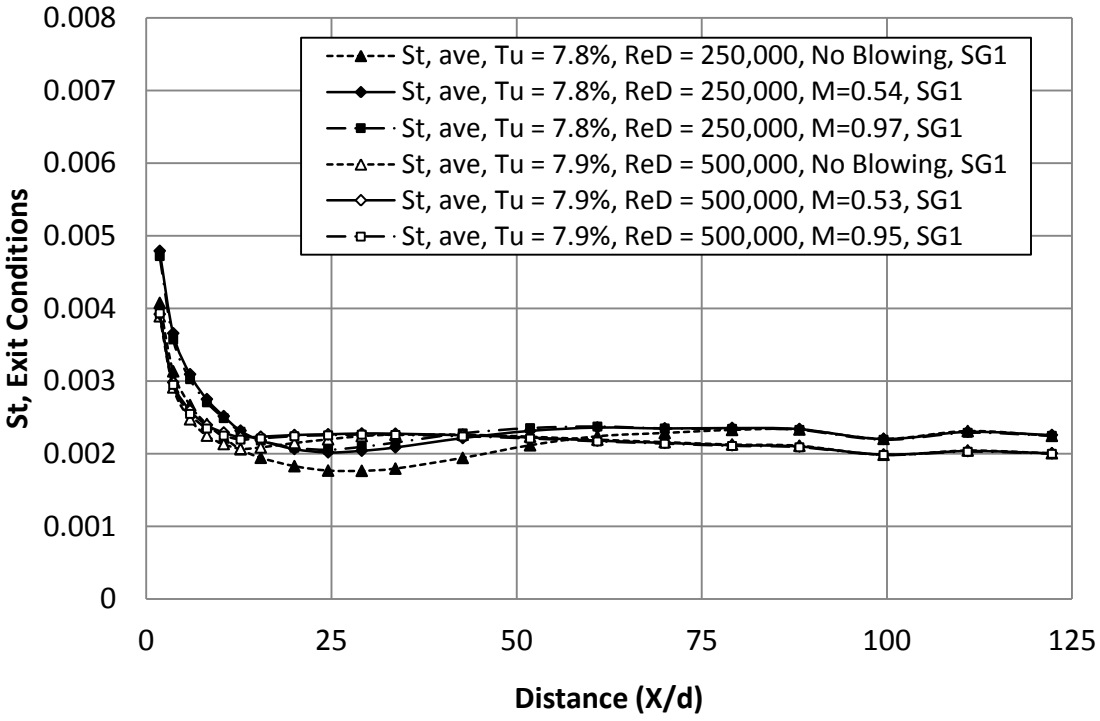

Figure 58. Stanton number comparison of high-low ReD at small grid near Tu.

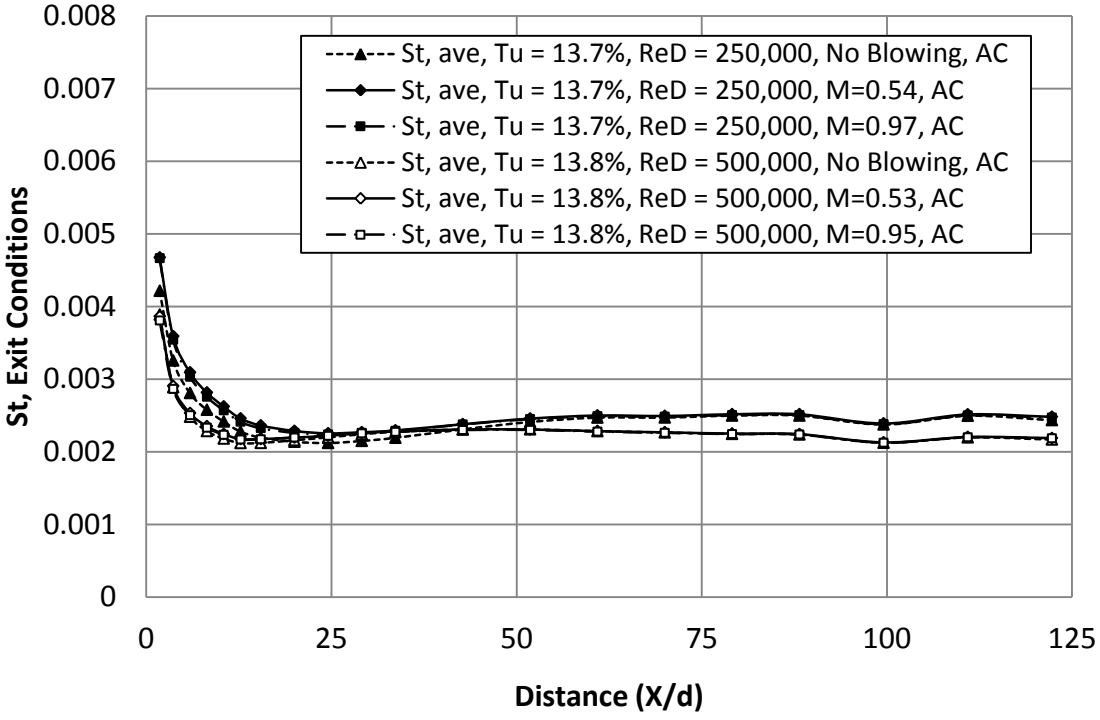

Figure 59. Stanton number comparison of high-low ReD at aero combustor Tu.

Adiabatic Effectiveness

In order to gain perspective on the nature of the film cooling coverage, IR camera measurements were taken at the low turbulence (LT) and small grid far (SG2) turbulence levels. Since the test section was not flat, the temperature array files were adjusted by correlating them to thermocouple data taken simultaneously. An IR image was used to locate the thermocouples underneath the foil as different temperatures were shown where thermocouple wires ran underneath the Inconel foil. For each thermocouple location, a block of nine cells in the array was averaged and compared to the thermocouple data taken. The regressions derived from this comparison gave an average value at each streamwise pixel location that was subtracted from all values to form a new array of adjusted values. From there, the same calculations were made as for the thermocouple data to form adjusted arrays of adiabatic effectiveness and heat transfer values. The figures show a common occurrence of several holes grouping together to provide a higher level of film cooling effectiveness. As the blowing ratio increases, these streaks of higher effectiveness go farther downstream, however the difference in spanwise effectiveness stays around 10% for the low turbulence level. In Figures 60 through 63, the low turbulence IR contour plots can be seen with increasing blowing ratios at the 250,000 Reynolds number. The black dots shown are marked at the locations of the reflective gold dots painted on the cylinder.

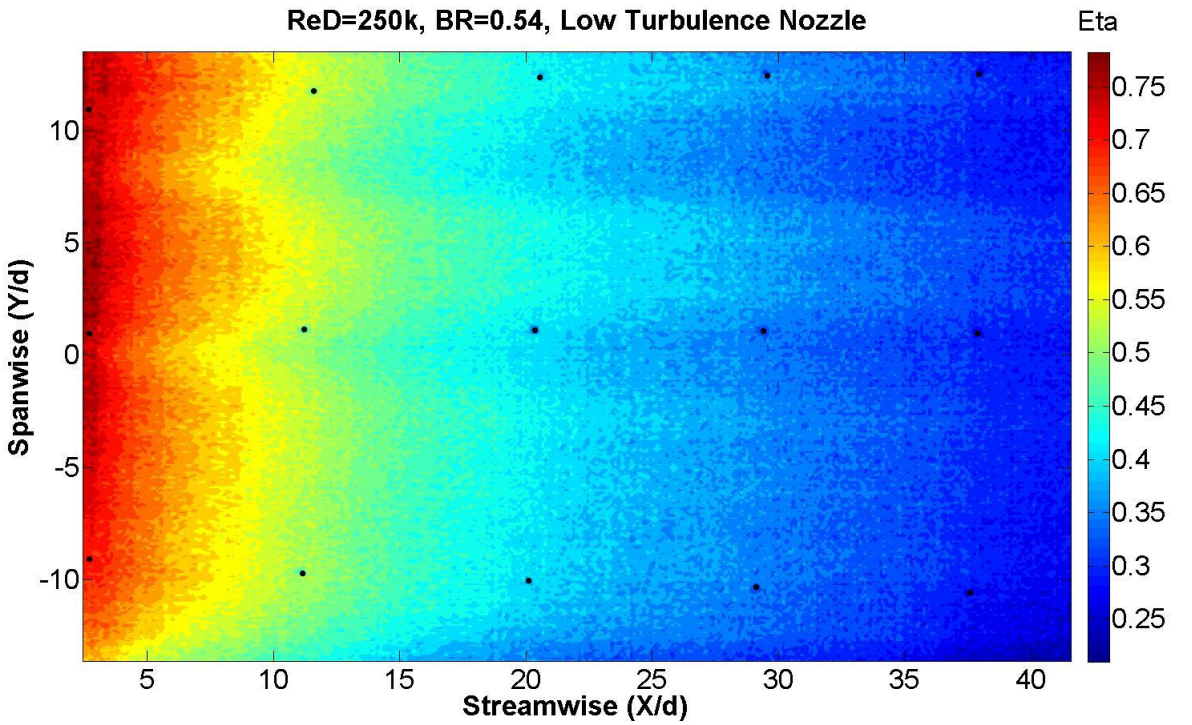

Figure 60. IR contour plot of adiabatic film cooling with LT nozzle at ReD=250k, M=0.54.

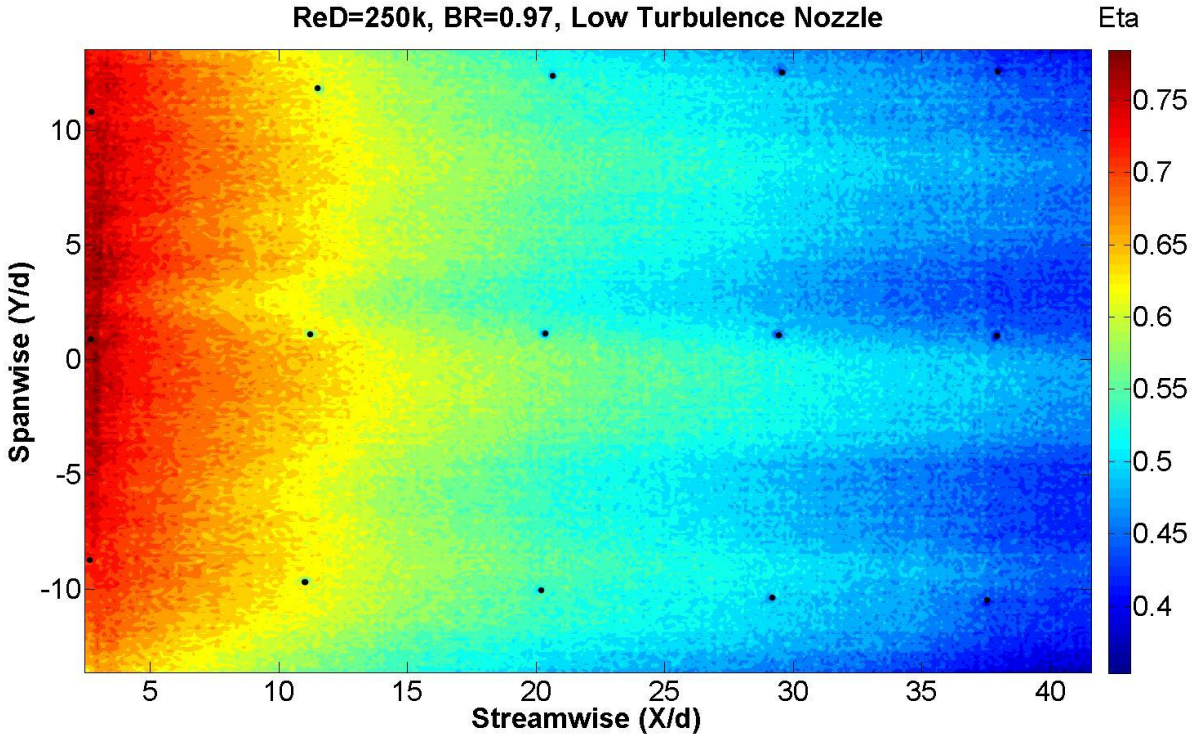

Figure 61. IR contour plot of adiabatic film cooling with LT nozzle at ReD=250k, M=0.97.

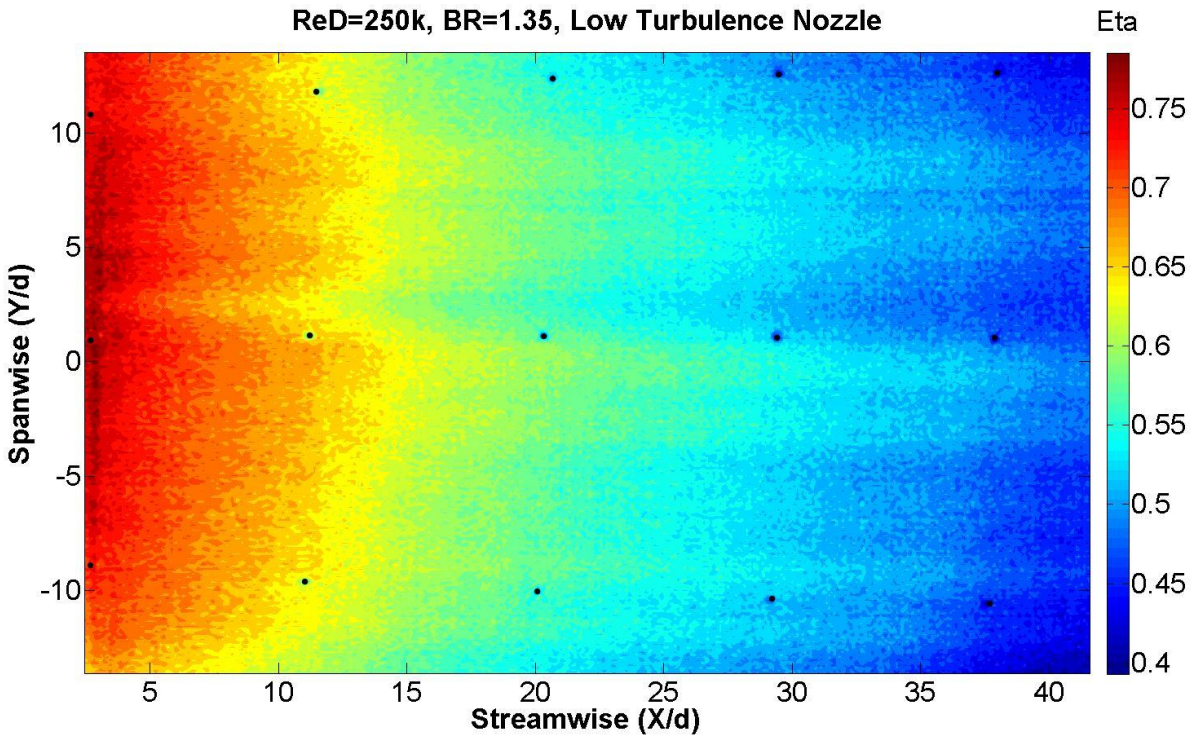

Figure 62. IR contour plot of adiabatic film cooling with LT nozzle at ReD=250k, M=1.35.

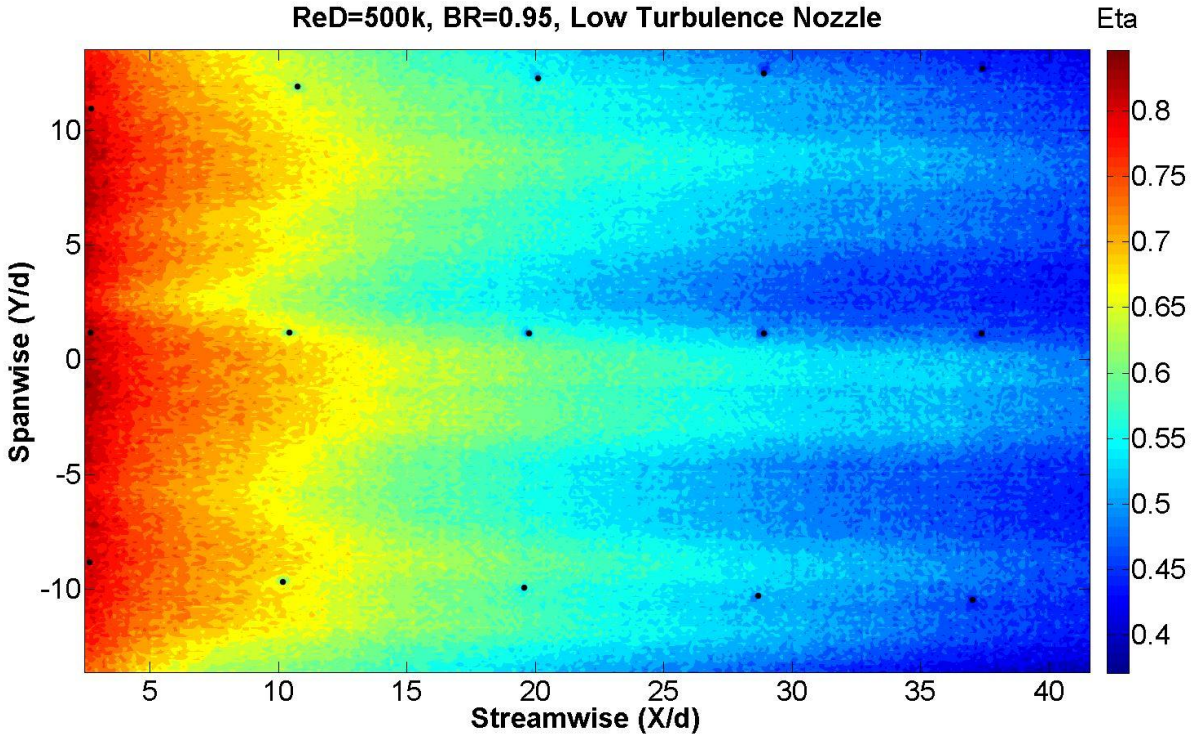

Figure 63. IR contour plot of adiabatic film cooling with LT nozzle at ReD=500k, M=0.95.

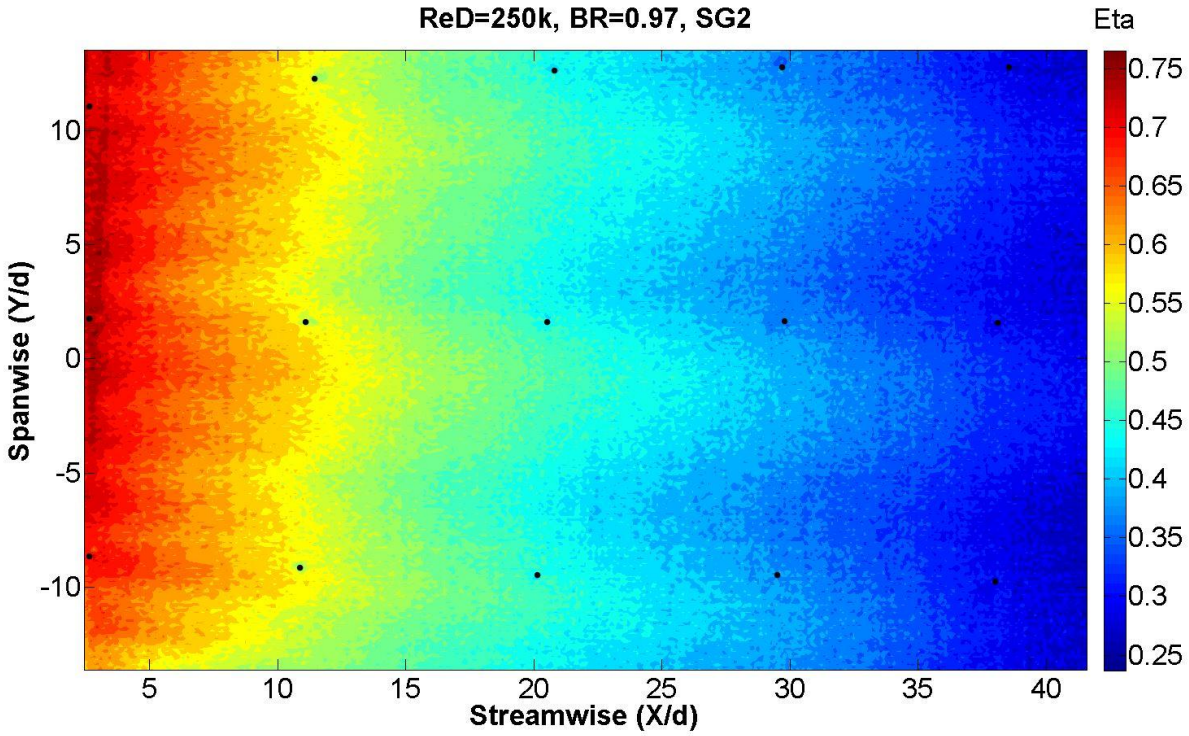

Figure 64. IR contour plot of adiabatic film cooling with SG2 at ReD=250k, M=0.97.

It is also important to show comparisons of the IR data to the thermocouple data used in creating the adjusted IR arrays. Figure 65 shows the spanwise average of the thermocouple data on top of the spanwise average of the 240 pixels in the IR image. This shows that the regression used for adjusting the IR array was effective in creating a good correlation between the two data types. In Figure 66, a spanwise plot of adiabatic effectiveness is shown for the low turbulence condition at M=0.97. Each row of thermocouples in the field of view is given with its corresponding row of IR values. In the early rows, the grouping of several holes is very clear between -5 and 0 hole diameters. These effects reduce as the boundary layer develops and are all but absent in the final row. Figure 67 shows a plot of the same form with a blowing ratio of 1.35. This shows less variation in the spanwise direction and fewer grouping effects in the region immediately downstream. When the turbulence level is increased for Figure 68, we see

lower overall effectiveness values, but with far less variation that the same blowing ratio at the low turbulence level. There are still grouping effects present in the early rows but these are less drastic than those seen in Figure 62 with low turbulence. The variation almost appears sinusoidal in the spanwise direction which suggests the holes are receiving equal amounts of coolant and the jets are very uniform.

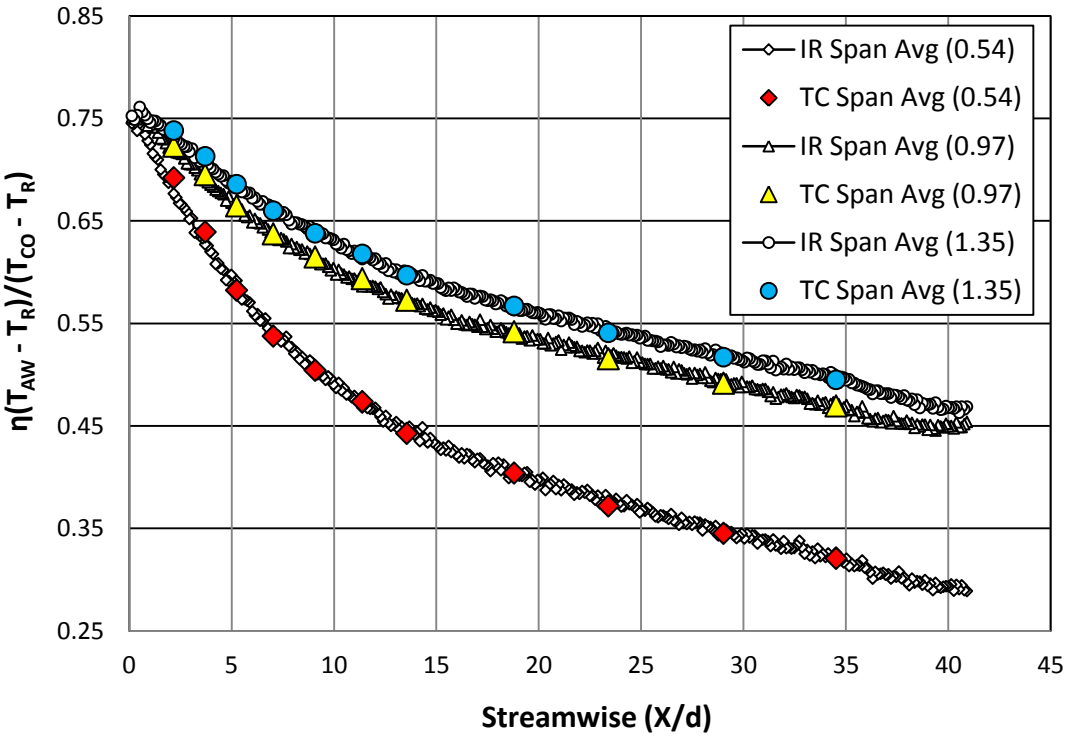

Figure 65. Spanwise averages of IR vs. thermocouple data with low Tu at ReD=250k.

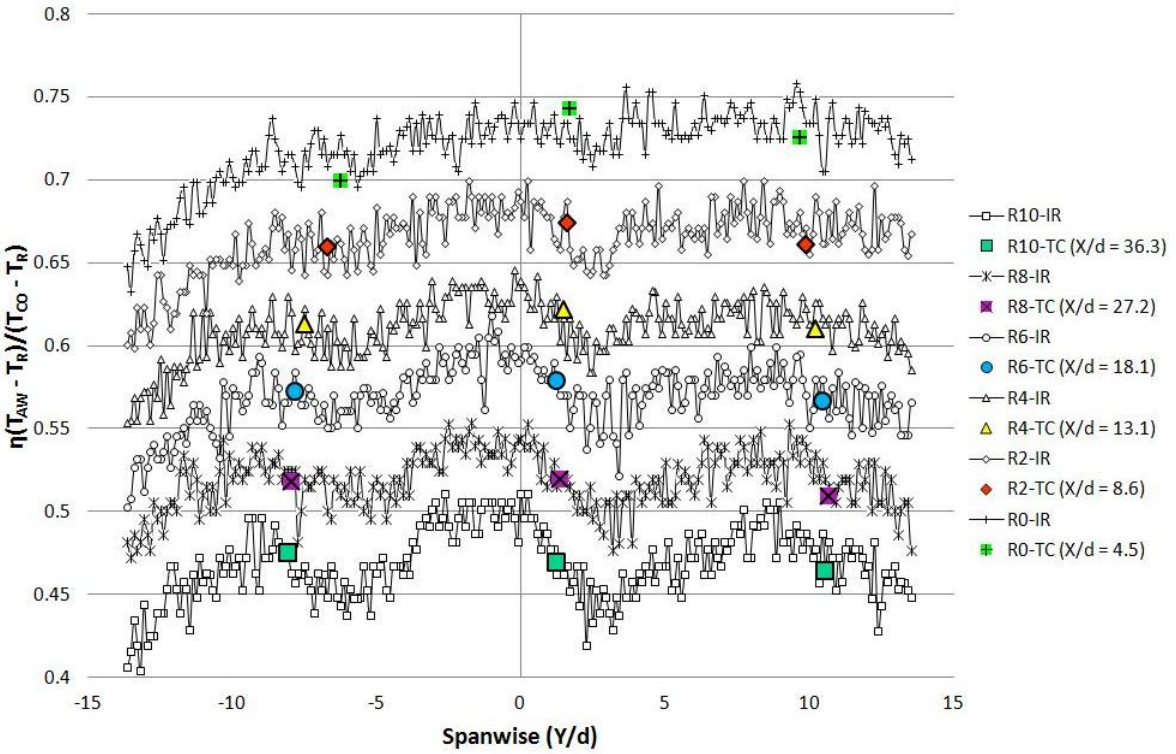

Figure 66. Plot of spanwise IR vs. thermocouple data with LT nozzle at ReD=250k, M=0.97.

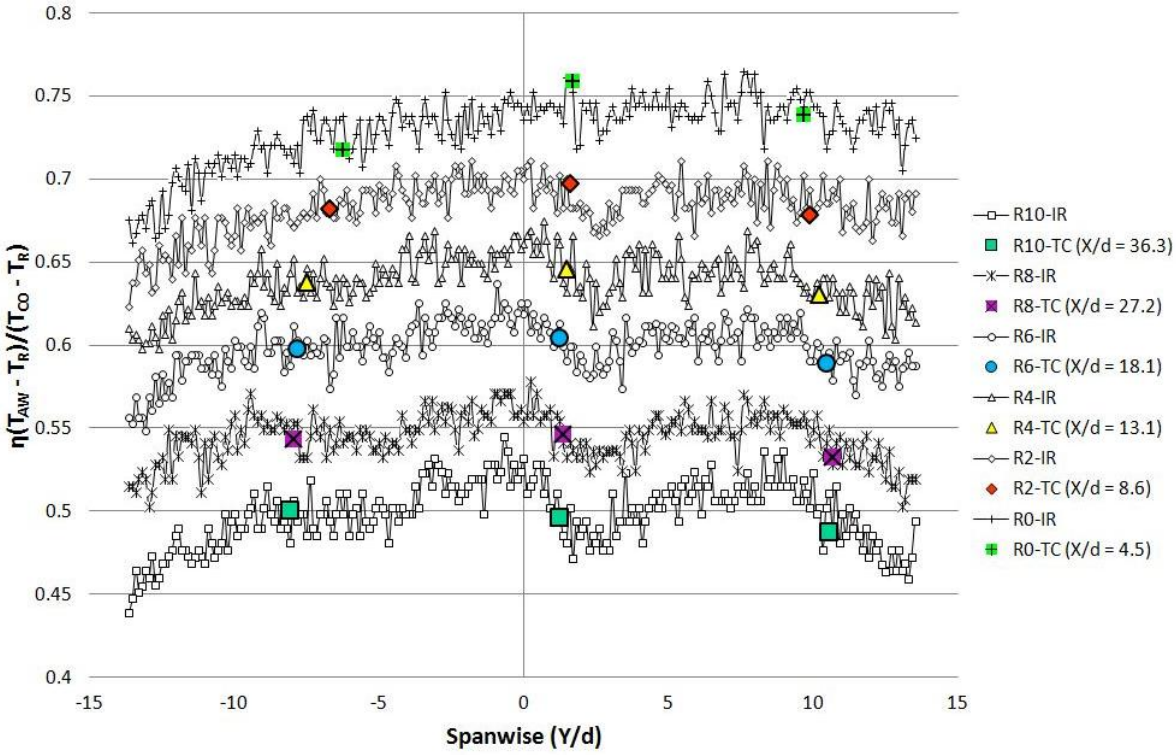

Figure 67. Plot of spanwise IR vs. thermocouple data with LT nozzle at ReD=250k, M=1.35.

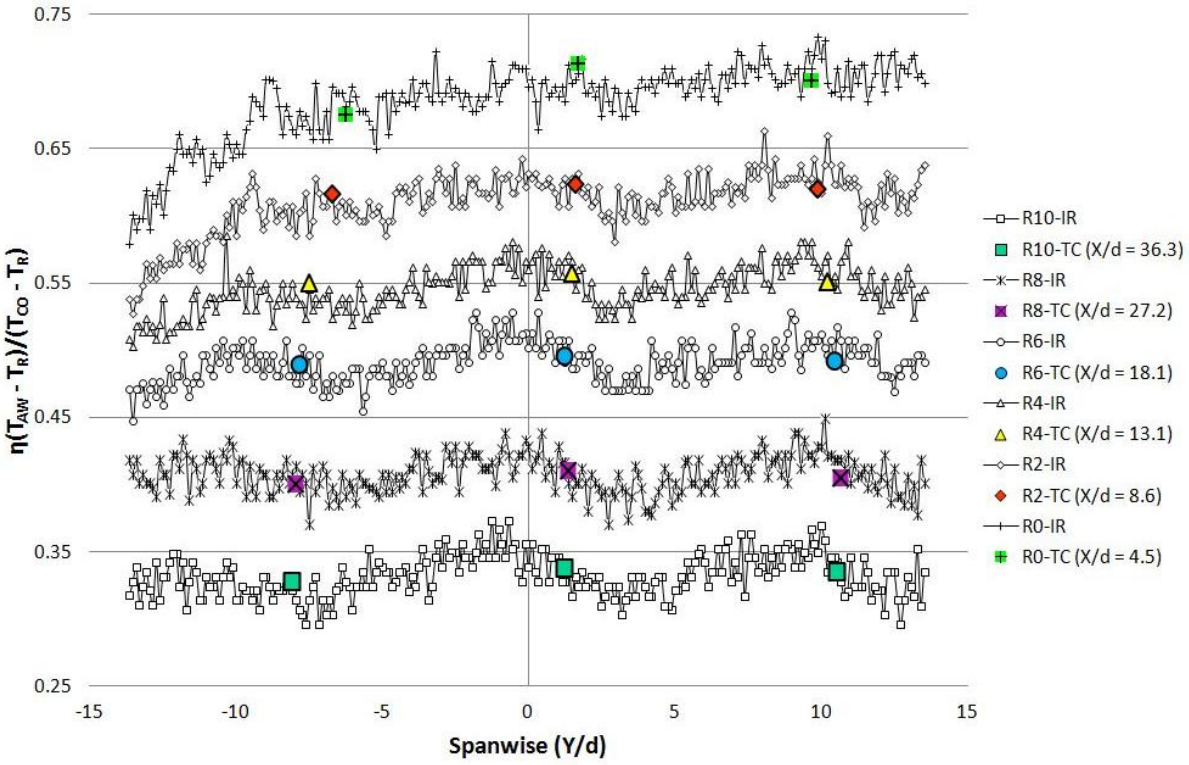

Figure 68. Plot of spanwise IR vs. thermocouple data with SG2 at ReD=250k, M=0.97.

Stanton number contour plots were also created from the IR arrays. Since the adjusted arrays ended up with such high Stanton numbers, the plots did not give much contour unless the first five hole diameters were left off. Figure 69 shows the heat transfer contour with the holes taped. The relatively straight contour lines show the boundary layer is even across the span, which we would expect given the no blowing condition. In Figure 70 with the second lowest blowing ratio, the contour lines clearly show the holes and the effects of the ejection geometry. The contour lines are relatively straight across again, showing that any grouping behavior has been subtracted out as the analysis was done. Up to a blowing ratio of 1.35 as seen in Figure 71, the gaps between the holes are very pronounced and show up as a sinusoidal contour across the span.

Increasing the blowing ratio to 1.90 in Figure 72, the sinusoidal behavior reduces significantly and the grouping behavior appears to be reoccurring.

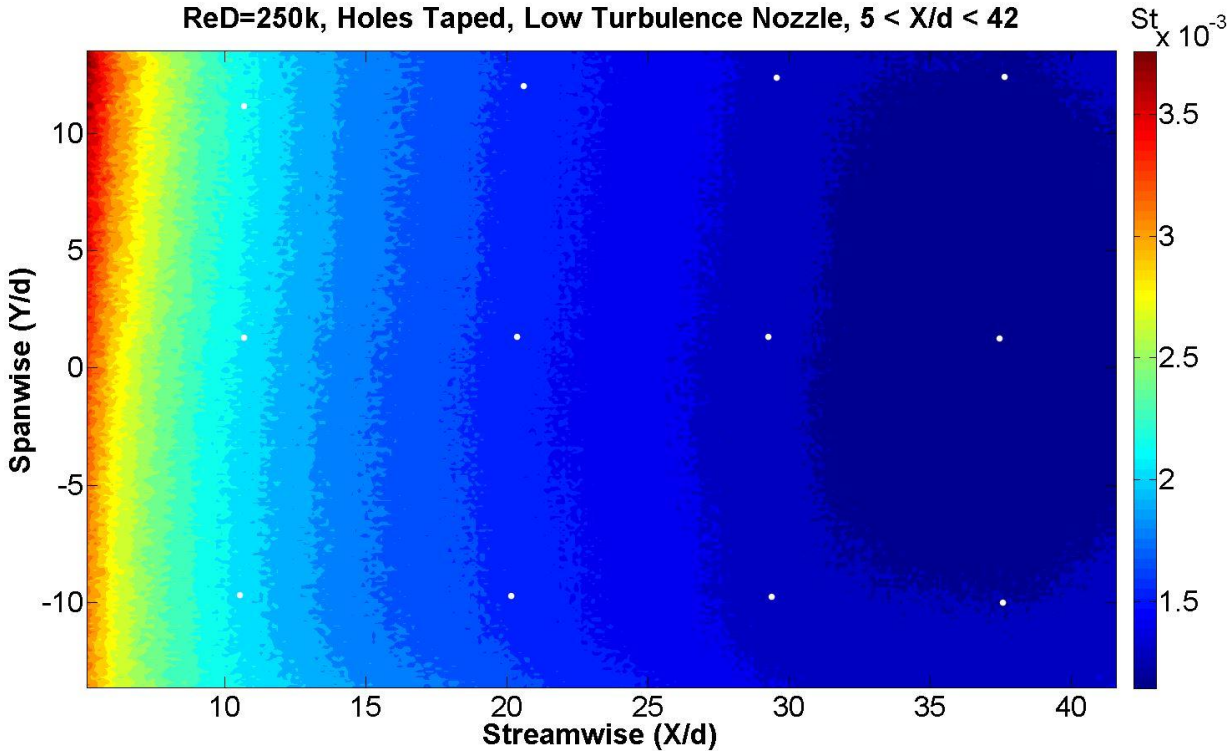

Figure 69. IR contour plot of Stanton number with LT nozzle at ReD=250k, holes taped.

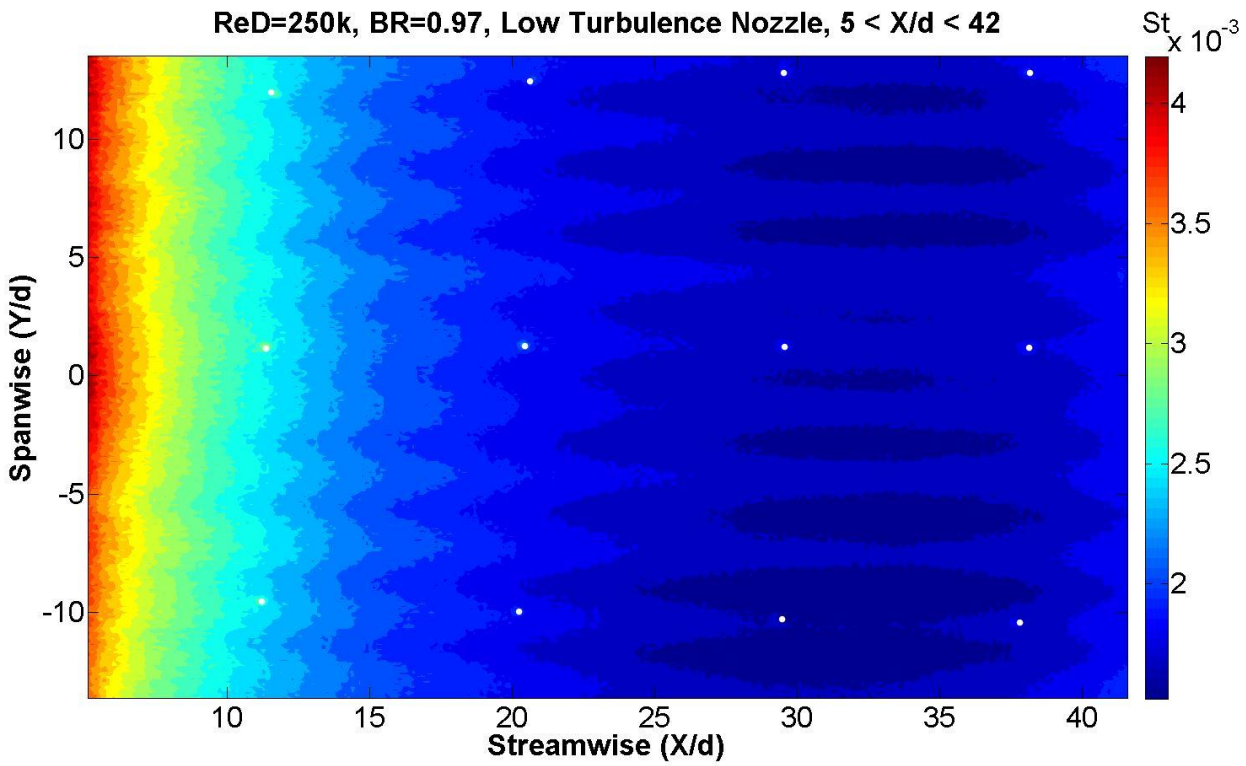

Figure 70. IR contour plot of Stanton number with LT nozzle at ReD=250k, M=0.97.

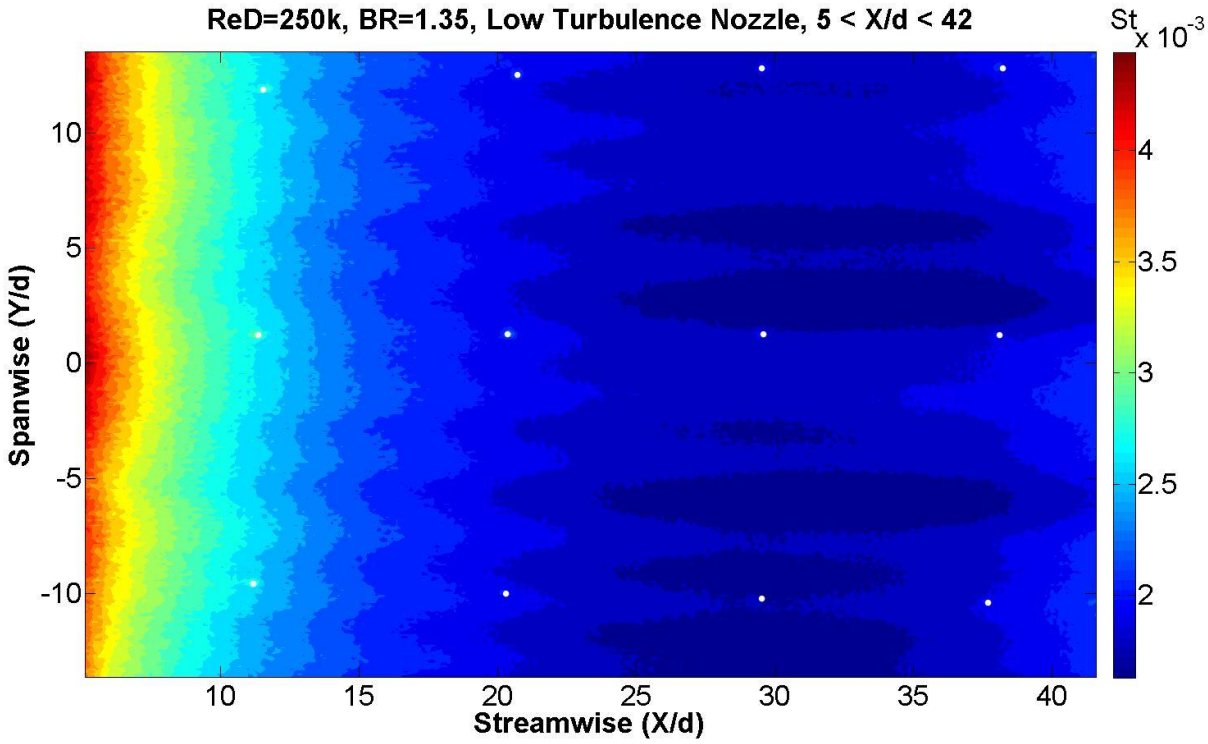

Figure 71. IR contour plot of Stanton number with LT nozzle at ReD=250k, M=1.35.

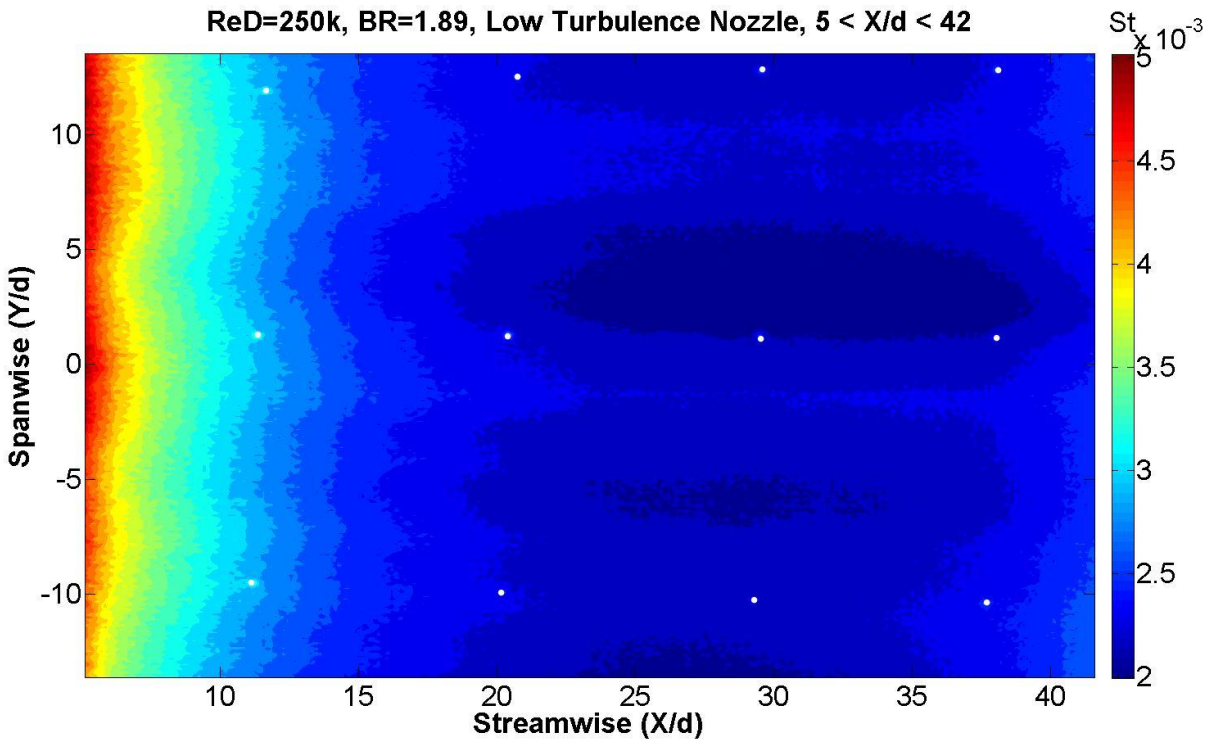

Figure 72. IR contour plot of Stanton number with LT nozzle at ReD=250, M=1.90.

Comparison of Shaped Holes and Slot Inserts

This study documents the streamwise effectiveness and heat transfer levels associated with a double staggered row of shaped holes in a highly accelerating flow. These measurements are consistent with a previous slot film cooling study and provide a means for back to back comparisons between the current shaped hole geometry and the slot's film cooling coverage. Since the profile of the test surface, the mass flow rate of the coolant, and the Reynolds numbers at which the two film cooling regimes were tested are nearly identical, a very good comparison can be made between the two. The slot film cooling data shown was from a previous study by Busche et al [5], and was conducted in the same facility as the current study. This section will show comparisons of adiabatic effectiveness and Stanton number with corresponding blowing ratios and increasing

levels of turbulence. As in the previous section on film cooling, the differences in effectiveness will discussed as simply the subtraction of one value from the other. The percentage differences given for the Stanton number comparison were calculated using Eq. 4-1.

$$\text{Percentage Difference} = \frac{\text{Slot Value} - \text{Shaped Holes Value}}{\text{Slot Value}} \tag{4-1}$$

Adiabatic Effectiveness

Adiabatic film cooling clearly favors the slot film cooling scheme immediately downstream. It is the theoretically ideal setup for film cooling coverage and its superiority can be seen in Figure 73. At 2.5 cm downstream, the slot has 14% to 24% higher effectiveness values than the shaped holes. However, by a distance of 35 cm, the effectiveness differences fall to a maximum of 1.9% and continue to decrease downstream to a value of less than 1%. Increasing the mass flow rate for a 1.35 blowing ratio (shaped holes) in Figure 74, the shaped holes actually show higher effectiveness values as early as 8.5 cm downstream for the low turbulence condition. The shaped holes also slightly outperform the slot for the small grid far condition, but the slot is more effective for the higher turbulence conditions. With the high blowing ratio in Figure 75, there is some different behavior. The low turbulence condition shows two changes, with the slot having higher effectiveness very early, and then again after 35 cm. The shaped holes slightly outperform the slot at the small grid far condition, but again the slot proves to have higher effectiveness at the higher turbulence levels.

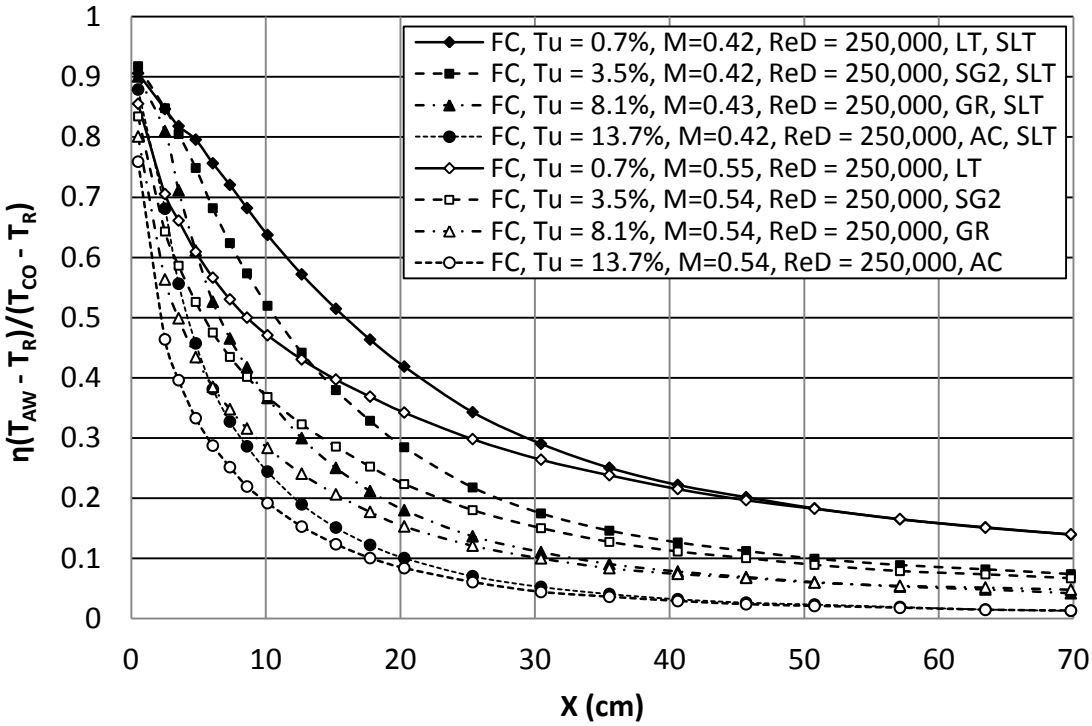

Figure 73. Film cooling comparison of slot vs shaped holes at ReD=250k, M=0.54.

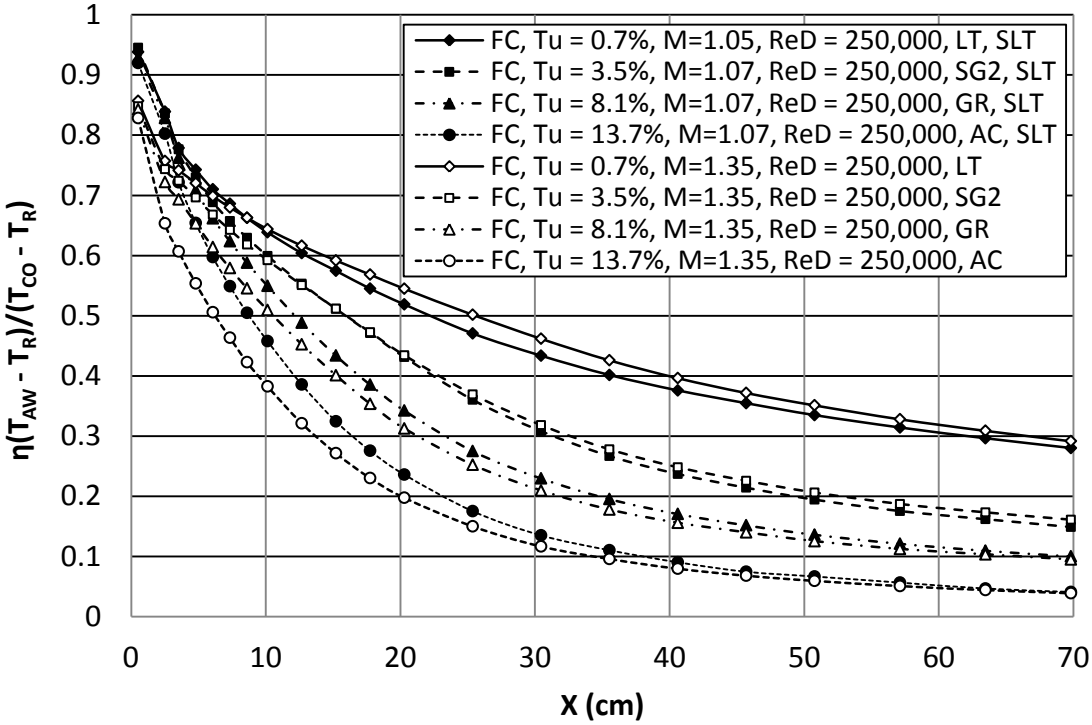

Figure 74. Film cooling comparison of slot vs shaped holes at ReD=250k, M=1.35.

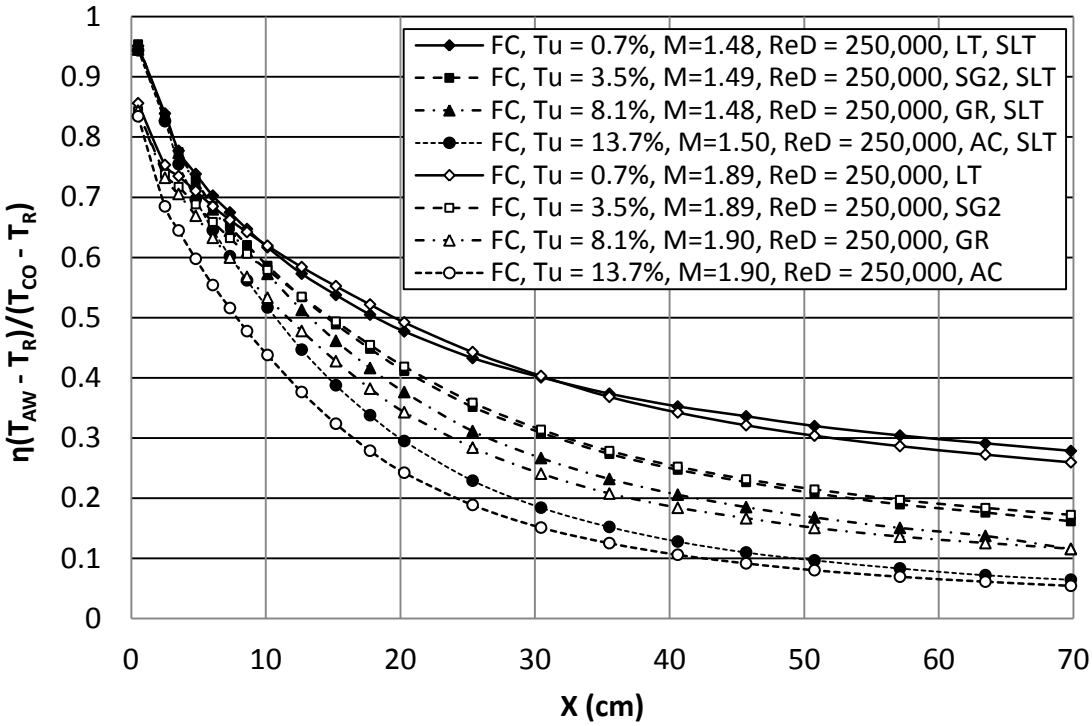

Figure 75. Film cooling comparison of slot vs shaped holes at ReD=250k, M=1.90.

Stanton Number

In a similar manner to the adiabatic effectiveness distribution, the slot provides significantly higher heat transfer immediately downstream. In Figure 76, we see the Stanton number values of the slot being higher in every case shown. However, the two lines at the low turbulence level are almost identical. The biggest disparity comes with the small grid far turbulence condition, where at a distance of 35 cm, there is a difference of 0.006, equating to about a 32% difference. The slot conditions appear to transition earlier than the shaped holes conditions which can be attributed to the profile of the shaped holes cylindrical test section being slightly smoother upstream of the test surface. When the mass flow rate is increased to the low blowing ratio, the differences drop significantly. In Figure 77 we see that all corresponding blowing ratios pair very closely.

Immediately downstream, there are percentage difference values of about 10%. These values fall rapidly and at a distance of 35 cm, the largest percentage difference is 1.1%. For the next blowing ratio in Figure 78, the same trend is followed. There is a slight anomaly for the low turbulence intensity, with an area of much different values appearing between 17 and 30 cm. Finally, Figure 79 shows the high blowing ratio. Again, large differences occur early and then drop about halfway down the foil. These differences early on show the curves using the slot geometry are transitioning earlier than the shaped holes curves.

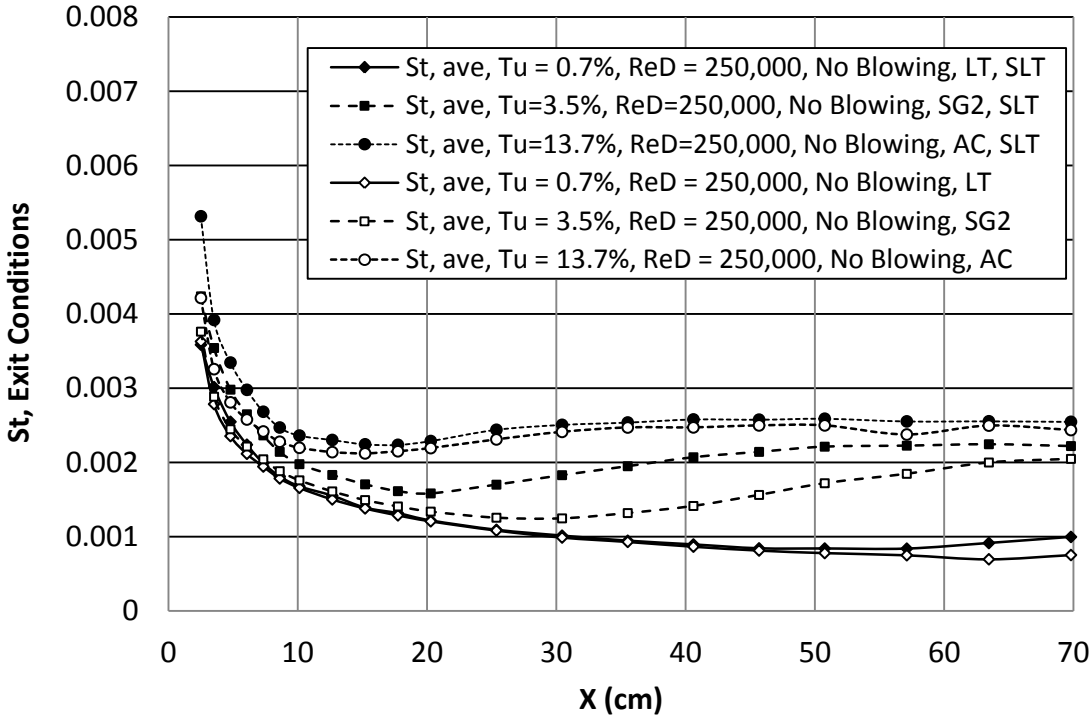

Figure 76. Stanton number comparison of slot vs shaped holes at ReD=250k, no blowing.

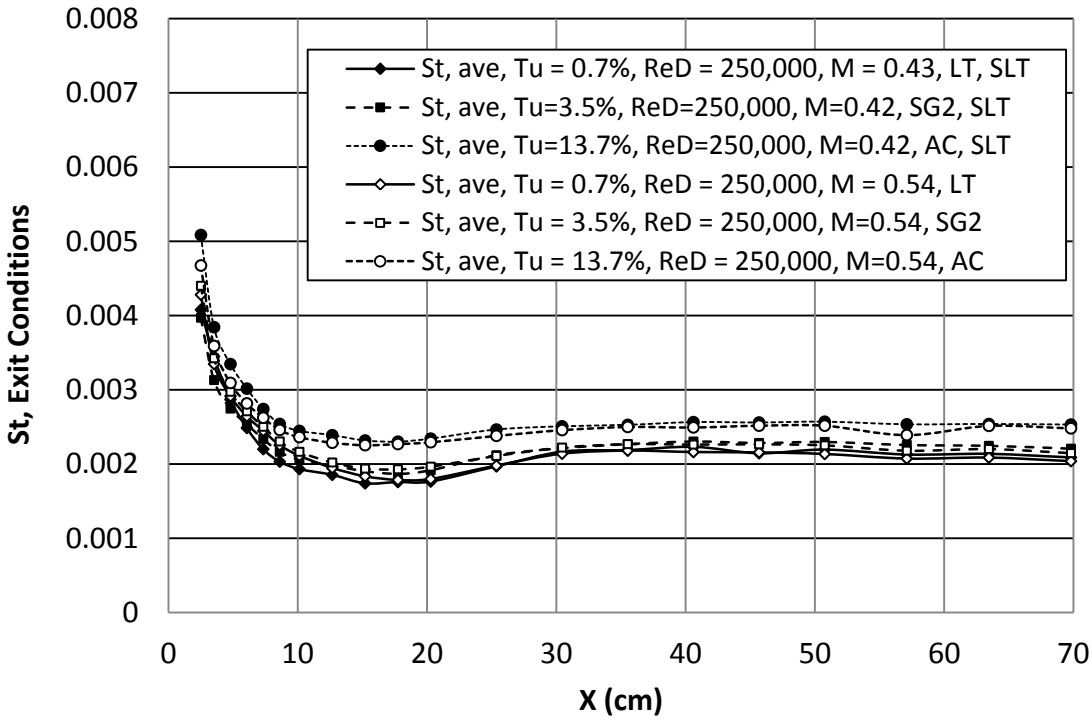

Figure 77. Stanton number comparison of slot vs shaped holes at ReD=250k, M=0.54.

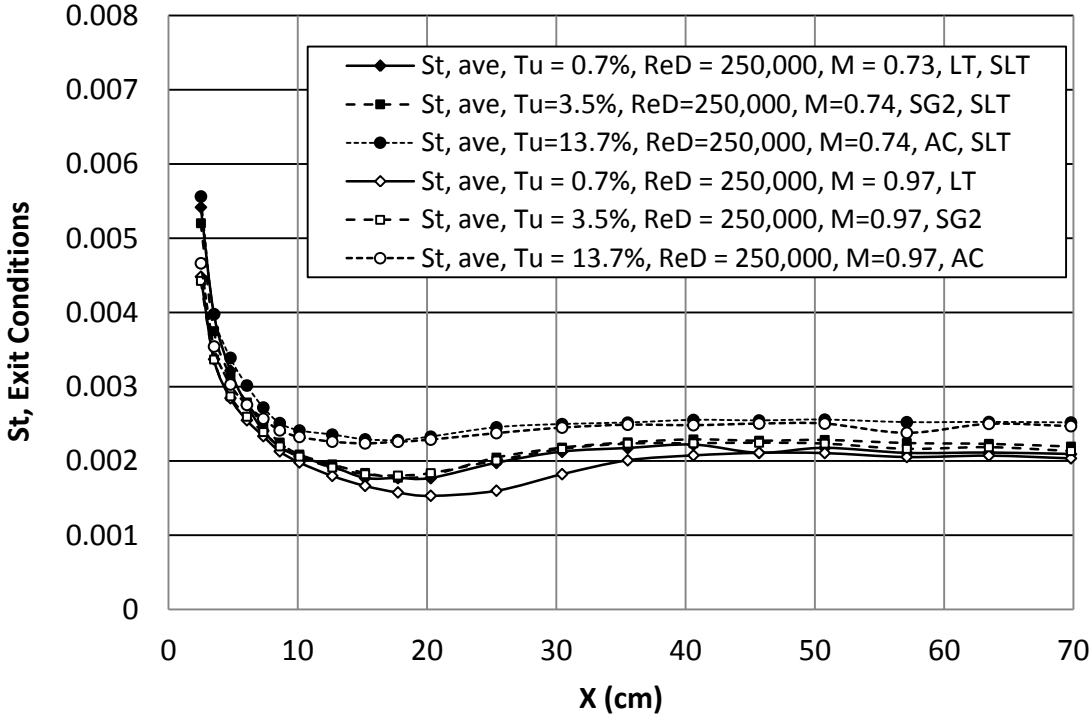

Figure 78. Stanton number comparison of slot vs shaped holes at ReD=250k, M=0.97.

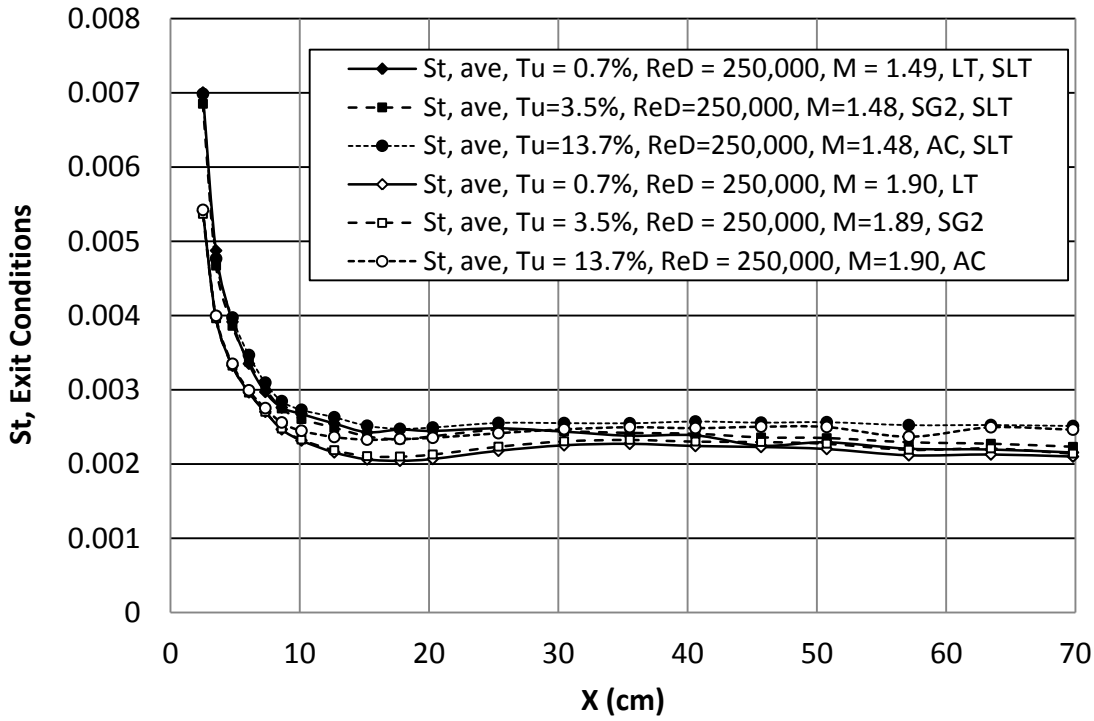

Figure 79. Stanton number comparison of slot vs shaped holes at ReD=250k, M=1.90.

CHAPTER V

CONCLUSIONS

A shaped holes leading edge insert containing a high solidity pin fin array was mounted to the large leading edge test cylinder for this film cooling study. The test cylinder was housed in the test section of UND's large scale low velocity wind tunnel cascade, which also underwent a number of modifications. The goal of this study was to document the film cooling coverage of a double staggered row of shaped holes in a highly accelerating flow. This study also expanded the database for film cooling and heat transfer data at a range of turbulence conditions. The cylinder diameter, free-stream Reynolds number, turbulence conditions, and coolant mass flow rate were very similar between the shaped holes study and a previous slot film cooling study, and comparisons were made between the two.

Adiabatic Effectiveness—Shaped Holes

Both the thermocouple data and the infrared images show that increasing turbulence intensity will decrease adiabatic effectiveness. Higher turbulence intensities have more adverse effects, and for many cases, the curves for a given blowing ratio show effectiveness ordering on turbulence intensity. Higher turbulence intensities caused more intense mixing which cause the coolant to be mixed off of the surface more quickly. Blowing ratio had a pronounced effect on adiabatic effectiveness. At all turbulence

intensities above the low turbulence condition, increasing the blowing ratio resulted in an increase in effectiveness. As turbulence increased, the importance of the mass addition regime was more pronounced, and the effectiveness levels nearly ordered on blowing ratio. Reynolds number had a small effect on adiabatic effectiveness. The higher Reynolds number condition would be expected to yield better cooling performance due to the thinner boundary layers, but the acceleration of the flow prolonged the laminar-transitional state of the low Reynolds number boundary layer to provide higher film cooling effectiveness. Once both flows had transitioned, the high and low Reynolds number curves were nearly indistinguishable.

Stanton Number—Shaped Holes

Values for Stanton number were calculated based on exit conditions. Both the thermocouple data and infrared images show an increase in Stanton number for increased turbulence intensity due to the increase in mixing across the boundary layer. This was true for all blowing ratios at the two Reynolds numbers, although the differences became less as turbulence increased. Blowing ratio had a more significant effect when the turbulence intensity was lower. The no blowing case showed significantly lower heat transfer at lower turbulence intensities since the boundary layer was able to stay laminar or transitioning longer. The high Stanton number values at the beginning of the test surface are a result of the unheated starting length. Stanton number values were slightly lower for the high Reynolds number for the first third of the surface distance before becoming closer. The lower Stanton number values for the higher velocity free-stream are consistent with a typical Reynolds number dependence.

Shaped Holes versus Slot Film Cooling

When comparing the new data to a previous study of similar design and flow conditions, the goal of providing similar film cooling performance and heat transfer with shaped holes as a 2D slot was nearly accomplished. The slot outperformed the shaped holes in adiabatic effectiveness in the near region, but there was much less disparity downstream. On the same note, the slot produced higher heat transfer in the near region, but downstream there was very little difference. This study shows that shaped hole film cooling technology is very vital to future improvements in cooling for gas turbine engines, based on the conditions tested.

Infrared Camera Measurements

The full coverage IR camera measurements show clear evidence of coolant jet grouping. There are clear streaks and variations across the span of the surface as the jets coalesce, but only a 10% variation exists across the span for the duration of the surface.

APPENDICES

Appendix A

Analysis of Data Sets

Film Cooling

Table 6. Cooled and adiabatic wall data.

ReD	250240.9							ReD	249871.7						
Ttin(K)	295.7199							Ttin(K)	291.656						
Ptin(Pa)	98101.92							Ptin(Pa)	98600.87						
Patm(Pa)	97888.56							Patm(Pa)	98396.45						
Blowing_r	0.398561	0.428848			0.437788			Blowing_r	0	0					
Vfreestm_	10.96478							Vfreestm_	10.20093						
Vexit(m/s)	19.24095				10.9277			Vexit(m/s)	18.64907						
Free_Strea	1.154349							Free_Strea	1.176523						
Exit_Mach	5.58E-02							Exit_Mach	5.45E-02						
Mass_flow	3.97E-03				4.784014			Mass_flow	0						
T_Cool_te	287.5081	287.6702	288.0095	287.7588				T_Cool_te	291.3454	291.3181	291.3106	291.328			
Surf_press	68.79566	70.02264	69.40915		Ttin =	22.627	C	Surf_press	60.65436	61.80061	61.22749		Ttin =	18.549	C
Slot&plm_	24.14241	24.24004			Tco =	14.61	C	Slot&plm_	149.4297	149.3911					
Temp_legend_Torf,Tin1,Tin2;Tc123;Tac12;Tbrk123;Tsrf1-60								Temp_legend_Torf,Tin1,Tin2;Tc123;Tac12;Tbrk123;Tsrf1-60							
	8.462	22.591	22.627						17.595	18.519	18.549				
	14.348	14.526	14.872						18.188	18.17	18.158				
	23.263	2.264							18.277	18.133					
	15.758	15.625	15.844						18.355	18.352	18.372				
	17.067	16.777	16.94						18.392	18.397	18.413				
	17.311	17.217	17.319						18.418	18.427	18.42				
	17.678	17.639	17.77						18.412	18.438	18.436				
	17.994	17.987	18.14						18.435	18.445	18.451				
	18.261	18.282	18.433						18.44	18.441	18.448				
	18.485	18.529	18.687						18.433	18.44	18.463				
	18.745	18.768	18.928						18.473	18.476	18.473				
	19.033	19.105	19.258						18.47	18.478	18.47				
	19.312	19.362	19.506						18.461	18.475	18.463				
	19.524	19.602	19.746						18.463	18.478	18.485				
	19.744	19.815	19.956						18.48	18.476	18.486				
	20.101	20.149	20.313						18.473	18.478	18.485				
	20.396	20.369	20.571						18.465	18.455	18.46				
	20.609	20.566	20.781						18.463	18.465	18.46				
	20.792	20.723	20.991						18.46	18.465	18.468				
	20.953	20.85	21.126						18.46	18.458	18.453				
	21.062	20.933	21.268						18.448	18.46	18.458				
	21.196	21.067	21.419						18.455	18.463	18.461				
	21.324	21.146	21.516						18.451	18.451	18.435				
	21.399	21.237	21.632						18.438	18.458	18.466				
HtrVlt_Cu	1.06E-02	0.00215	2.28E-05					HtrVlt_Cu	7.95E-03	0.00235	1.87E-05				
Orifice_pr	98128.7							Orifice_pr	98396.48						
DeltaP_or	26.12512							DeltaP_or	-7.66E-02						
Torific(K)	281.6405							Torific(K)	290.7364						
Pexit_stati	213.5301							Pexit_stati	204.4444						
Pressure_legend_Pbrk12;Pslt12;Plnm;Pta,Pts;Pua,dPorf								Pressure_legend_Pbrk12;Pslt12;Plnm;Pta,Pts;Pua,dPorf							
	0.276	0.281							0.244	0.248					
	0.097	0.097							0.6	0.6					
	0								0						
	0.105	0.964							0	0					
	0.857	213.53							0.821	204.444					
	14.042	14.591							17.964	17.941					

The above data sets were taken with the shaped holes insert in the large leading edge cylinder at the low turbulence intensity. The data set on the left shows the coolant temperature as low as was possible at the ReD=250k and M=0.55 blowing ratio. The data set on the right is for the adiabatic wall for the same ReD and turbulence but with the holes taped. Adiabatic effectiveness was calculated for each thermocouple using Eq. B-1.

$$\eta = \frac{(T_{cw} - T_{aw} - T_{in,cw} + T_{in,aw})}{(T_{co} - T_{aw} - T_{in,cw} + T_{in,aw})} \quad \text{(B-1)}$$

The equation yielded three columns of data that were then laterally averaged, which are the values given in all of the figures throughout Chapter 4.

Stanton Number

Table 7. Heated and adiabatic wall data.

ReD	249649.6							ReD	250219.4						
Ttin(K)	294.9302							Ttin(K)	294.8633						
Ptin(Pa)	97863.42							Ptin(Pa)	99012.44						
Patm(Pa)	97651.55							Patm(Pa)	98802.77						
Blowing_r	0.390336	0.420194			0.419581			Blowing_r	0.389855	0.420816					
Vfreestm_	10.91866							Vfreestm_	10.84126						
Vexit(m/s)	19.15087				11.72835			Vexit(m/s)	18.96301						
Free_Strea	1.154635							Free_Strea	1.168482						
Exit_Mach	0.055615							Exit_Mach	5.51E-02						
Mass_flow	3.87E-03				4.920991			Mass_flow	3.89E-03						
T_Cool_te	294.8287	294.9079	294.8535	294.8411				T_Cool_te	294.8807	294.8955	294.9005	294.8906			
Surf_press	68.08357	69.60333	68.84345		Ttin =	22.067	C	Surf_press	68.08627	69.28284	68.68456		Ttin =	21.793	
Slot&plm_	24.10496	23.58792			Tco =	21.703	C	Slot&plm_	24.08432	24.37725			Tco =	21.7395	C
Temp_legend_Torf,Tin1,Tin2;Tc123;Tac12;Tbrk123;Tsrf1-60								Temp_legend_Torf,Tin1,Tin2;Tc123;Tac12;Tbrk123;Tsrf1-60							
	21.793	21.901	22.067						21.967	21.675	21.793				
	21.693	21.755	21.713						21.727	21.752	21.752				
	22.543	22.599							22.221	22.275					
	22.204	22.224	22.076						21.744	21.752	21.755				
	29.476	28.653	28.848						21.727	21.736	21.759				
	31.488	30.674	30.754						21.726	21.744	21.754				
	32.749	32.187	31.989						21.714	21.742	21.747				
	33.753	33.249	33.094						21.717	21.732	21.752				
	34.681	34.143	33.982						21.709	21.724	21.747				
	35.807	35.121	35.038						21.706	21.732	21.774				
	36.736	36.092	35.841						21.731	21.749	21.764				
	37.996	37.14	37.103						21.726	21.749	21.77				
	38.938	38.028	38.051						21.724	21.751	21.752				
	39.417	38.473	38.457						21.716	21.744	21.764				
	39.316	38.32	38.393						21.708	21.746	21.77				
	37.784	37.008	36.816						21.706	21.734	21.762				
	36.26	36.082	35.89						21.703	21.716	21.739				
	35.789	35.984	35.657						21.683	21.713	21.724				
	35.945	36.149	35.748						21.68	21.716	21.751				
	35.862	36.252	35.813						21.681	21.713	21.734				
	35.988	36.413	35.909						21.661	21.696	21.732				
	36.255	36.899	36.421						21.656	21.701	21.741				
	36.395	36.805	36.121						21.668	21.701	21.726				
	36.744	37.246	36.34						21.658	21.694	21.724				
HtrVlt_Cu	5.162395	32.04805	165.4447	0.161083				HtrVlt_Cu	0.005491	0.0021	1.15E-05				
Orifice_pr	97889.7							Orifice_pr	99037.36						
DeltaP_or	25.98419							DeltaP_or	25.88625						
Torific(K)	294.9475							Torific(K)	295.1209						
Pexit_stati	211.5892							Pexit_stati	209.9499						
Pressure_legend_Pbrk12;Pslt12;Plnm;Pta,Pts;Pua,dPorf								Pressure_legend_Pbrk12;Pslt12;Plnm;Pta,Pts;Pua,dPorf							
	0.273	0.28							0.273	0.278					
	0.097	0.095							0.097	0.098					
	0								0						
	0.104	0.956							0.104	0.942					
	0.851	211.589							0.842	209.95					
	21.651	21.683							21.708	21.732					

The above data sets were taken with the shaped holes insert in the large leading edge cylinder at the low turbulence intensity. The data set on the left shows the heater was dissipating 165 watts and temperatures were nearly 40°C at the ReD=250k and

M=0.55 blowing ratio. The data set on the right is for the adiabatic wall for the same ReD , blowing ratio, and turbulence with no power sent to the Inconel heater. First, ΔT was calculated for each thermocouple location using Eq. B-2.

$$\Delta T = (T_{hw} - T_{aw}) - \eta * \left(T_{co,hw} - T_{co,aw}\right) + (1 - \eta) * (T_{in,hw} - T_{in,aw}) \quad \text{(B-2)}$$

After creating a table of delta T values, the convective heat transfer coefficient h was calculated using Eq. B-3, where 5.67e-8 represents the Stephan Boltzmann constant and 0.21 represents the emissivity for the Inconel foil.

$$h = \frac{\left[\frac{\text{Heater Power}}{\text{Area of Foil} - 0.0000000567 * 0.21 * (T_{hw}{}^4 - T_{aw}{}^4)}\right]}{\Delta T} \quad \text{(B-3)}$$

After calculating the heat transfer coefficient, the Stanton number could be calculated using Eq. B-4. Here, 1005 j/kg*K was the value used for c_p throughout all of the analyses. Also, the values for U_{ex} come from Vexit in the data sets.

$$St = \frac{h}{\rho U_{ex} * 1005} \quad \text{(B-4)}$$

Once the Stanton numbers were calculated, they were laterally averaged. These are the values given in all of the Stanton number charts throughout Chapter 4.

Appendix B

Adiabatic Effectiveness and Stanton Number Data

Table 8. Effectiveness data for low turbulence case.

Low Turbulence (LT)						
ReD	250241	249448	250741	250278	500388	499896
Ttin (K)	295.72	295.81	295.89	293.85	295.82	295.69
Ptin (Pa)	98102	98100	98104	98132	98784	98776
Patm (Pa)	97889	97889	97889	97922	97922	97922
Blowing Ratio	0.550	0.976	1.352	1.890	0.527	0.946
Vexit (m/s)	19.241	19.190	19.299	19.022	38.613	38.545
Free Stream Density	1.154	1.154	1.154	1.162	1.157	1.158
Exit Mach Number	0.0558	0.0556	0.0560	0.0553	0.1119	0.1117
Mass Flow Rate (kg/s)	0.00397	0.00703	0.00979	0.01359	0.00766	0.01373
T Cool, avg (K)	287.51	285.55	284.60	281.14	285.53	283.75
X/d	Adiabatic Effectiveness					
0.909091	0.855353	0.850227	0.856965	0.856265	0.844383	0.871273
1.818182	0.705411	0.737873	0.75705	0.753736	0.641849	0.769151
3.636364	0.661284	0.718858	0.741454	0.735058	0.592012	0.747251
5.909091	0.609245	0.692331	0.720181	0.710395	0.54019	0.718311
8.181818	0.566426	0.668133	0.698732	0.684995	0.498951	0.689193
10.454545	0.530363	0.647744	0.679757	0.662395	0.467129	0.662998
12.727273	0.499974	0.628587	0.662829	0.6422	0.43794	0.637849
15.454545	0.470704	0.608657	0.643761	0.619495	0.410712	0.613225
20.000000	0.430525	0.579711	0.61624	0.583972	0.370952	0.573456
24.545455	0.397133	0.554883	0.591786	0.552338	0.342258	0.540891
29.090909	0.36879	0.531852	0.568299	0.521861	0.31958	0.514881
33.636364	0.342242	0.509024	0.544802	0.492122	0.300941	0.492428
42.727273	0.298119	0.467263	0.501588	0.442771	0.271156	0.455349
51.818182	0.263959	0.427934	0.461725	0.403106	0.24654	0.422884
60.909091	0.238144	0.393965	0.425922	0.368343	0.226986	0.394515
70.000000	0.215199	0.364271	0.396304	0.342292	0.208108	0.367233
79.090909	0.196673	0.339444	0.371672	0.321139	0.192935	0.343212
88.181818	0.182456	0.318117	0.351127	0.303788	0.179423	0.323961
99.545455	0.165285	0.293626	0.327964	0.286443	0.163748	0.300289
110.909091	0.150988	0.272734	0.308838	0.272349	0.150437	0.278901
122.272727	0.140041	0.254094	0.291558	0.259539	0.138605	0.259461

Table 9. Effectiveness data for small grid far Tu case.

Small Grid Far (SG2)						
ReD	251406	250927	251086	251883	501358	500937
Ttin (K)	295.73	296.07	295.45	294.05	296.35	296.31
Ptin (Pa)	99827	99827	99827	100839	101474	101474
Patm (Pa)	99615	99615	99615	100631	100631	100631
Blowing Ratio	0.543	0.970	1.353	1.894	0.532	0.957
Vexit (m/s)	18.996	18.998	18.940	18.650	37.759	37.717
Free Stream Density	1.175	1.173	1.176	1.193	1.187	1.187
Exit Mach Number	0.0551	0.0551	0.0550	0.0542	0.1093	0.1092
Mass Flow Rate (kg/s)	0.00394	0.00703	0.00980	0.01371	0.00776	0.01394
T Cool, avg (K)	285.69	283.11	281.20	281.77	286.06	284.36
X/d	Adiabatic Effectiveness					
0.909091	0.834316	0.842182	0.847885	0.843223	0.805971	0.860525
1.818182	0.64308	0.715709	0.743395	0.738864	0.56606	0.745119
3.636364	0.586226	0.687502	0.72401	0.717243	0.513586	0.713761
5.909091	0.526015	0.649657	0.696376	0.688157	0.456544	0.672188
8.181818	0.475138	0.614015	0.66784	0.658983	0.411582	0.631549
10.454545	0.434662	0.585075	0.642478	0.632118	0.375784	0.59452
12.727273	0.401507	0.55737	0.618152	0.606029	0.343095	0.558433
15.454545	0.368018	0.526696	0.59209	0.57925	0.311493	0.52124
20.000000	0.322717	0.482869	0.550693	0.534916	0.268386	0.463646
24.545455	0.285612	0.443081	0.51154	0.49367	0.234783	0.416047
29.090909	0.252387	0.404269	0.472492	0.454665	0.209258	0.376934
33.636364	0.223327	0.367057	0.434162	0.418571	0.189017	0.344126
42.727273	0.180036	0.306181	0.369114	0.358717	0.158916	0.294602
51.818182	0.150102	0.260508	0.318126	0.313923	0.137668	0.2568
60.909091	0.127216	0.225038	0.277847	0.278606	0.121206	0.227568
70.000000	0.111224	0.199701	0.248003	0.252415	0.108029	0.203624
79.090909	0.100257	0.181588	0.225552	0.231442	0.098216	0.18409
88.181818	0.089047	0.163716	0.206076	0.214539	0.090076	0.16914
99.545455	0.078694	0.147623	0.186975	0.197083	0.081727	0.152719
110.909091	0.073214	0.1366	0.17308	0.183818	0.075344	0.139239
122.272727	0.066779	0.126543	0.160897	0.172274	0.070025	0.129116

Table 10. Effectiveness data for small grid near case.

Small Grid Near (SG1)						
ReD	250294	250361	250544	250875	501082	499663
Ttin (K)	298.67	298.56	298.46	298.52	297.85	297.99
Ptin (Pa)	98682	98681	98682	98683	99775	99767
Patm (Pa)	98464	98464	98464	98464	98904	98904
Blowing Ratio	0.543	0.972	1.347	1.896	0.529	0.952
Vexit (m/s)	19.472	19.464	19.467	19.500	38.749	38.673
Free Stream Density	1.150	1.150	1.150	1.150	1.161	1.160
Exit Mach Number	0.0562	0.0562	0.0562	0.0563	0.1119	0.1116
Mass Flow Rate (kg/s)	0.00395	0.00707	0.00981	0.01383	0.00773	0.01389
T Cool, avg (K)	290.06	286.58	285.78	284.03	287.80	285.56
X/d	Adiabatic Effectiveness					
0.909091	0.823898	0.838802	0.848348	0.845743	0.809445	0.870976
1.818182	0.604292	0.694805	0.729006	0.731996	0.53538	0.712947
3.636364	0.543451	0.65935	0.701515	0.705923	0.473133	0.669498
5.909091	0.479109	0.613836	0.664929	0.671249	0.410485	0.615984
8.181818	0.428364	0.572363	0.629536	0.637731	0.362855	0.564581
10.454545	0.389396	0.536395	0.597719	0.606974	0.324569	0.520444
12.727273	0.35514	0.502117	0.56626	0.576119	0.289071	0.478949
15.454545	0.319981	0.465735	0.53276	0.543361	0.256359	0.433746
20.000000	0.273883	0.410345	0.47886	0.489757	0.212751	0.372806
24.545455	0.235475	0.360827	0.428086	0.44084	0.178809	0.325198
29.090909	0.203181	0.317003	0.381762	0.396916	0.155305	0.28643
33.636364	0.175734	0.279616	0.341303	0.359089	0.13732	0.255537
42.727273	0.140033	0.22582	0.280837	0.301798	0.110073	0.21199
51.818182	0.117132	0.189499	0.238312	0.260521	0.090566	0.181105
60.909091	0.098128	0.161228	0.205226	0.228573	0.079276	0.156738
70.000000	0.085984	0.141554	0.182097	0.204959	0.068409	0.139037
79.090909	0.078577	0.127848	0.164607	0.187073	0.05971	0.126345
88.181818	0.069506	0.114563	0.148909	0.171302	0.054706	0.113617
99.545455	0.06171	0.10265	0.134223	0.155804	0.048715	0.101892
110.909091	0.058291	0.094418	0.123697	0.144433	0.042849	0.094085
122.272727	0.053975	0.087023	0.114487	0.13454	0.039469	0.086704

Table 11. Effectiveness data for large grid case.

Large Grid (GR)						
ReD	251189	250896	250645	250495	502963	501036
Ttin (K)	294.88	294.94	295.01	295.05	295.51	295.87
Ptin (Pa)	98744	98744	98744	98743	100933	100936
Patm (Pa)	98532	98532	98532	98532	100089	100089
Blowing Ratio	0.542	0.968	1.346	1.896	0.530	0.953
Vexit (m/s)	19.091	19.075	19.065	19.057	37.898	37.829
Free Stream Density	1.165	1.165	1.165	1.165	1.184	1.183
Exit Mach Number	0.0554	0.0554	0.0554	0.0553	0.1098	0.1096
Mass Flow Rate (kg/s)	0.00392	0.00699	0.00972	0.01368	0.00773	0.01387
T Cool, avg (K)	284.78	281.86	280.49	279.93	281.37	284.95
X/d	Adiabatic Effectiveness					
0.909091	0.801011	0.835732	0.842796	0.843926	0.771435	0.855885
1.818182	0.563398	0.68684	0.722106	0.732363	0.494141	0.704685
3.636364	0.498922	0.648213	0.693201	0.705511	0.43629	0.659643
5.909091	0.434339	0.598618	0.653327	0.669267	0.378259	0.602826
8.181818	0.384985	0.552905	0.613965	0.632653	0.336117	0.552497
10.454545	0.347861	0.513606	0.579129	0.599722	0.301749	0.508022
12.727273	0.315722	0.477605	0.545444	0.567695	0.270496	0.464807
15.454545	0.283542	0.43943	0.509426	0.533065	0.241849	0.422228
20.000000	0.240642	0.382551	0.452375	0.47774	0.201134	0.360225
24.545455	0.20632	0.332875	0.400977	0.427574	0.170853	0.312136
29.090909	0.177239	0.289702	0.353459	0.381984	0.148659	0.274085
33.636364	0.153073	0.252952	0.312593	0.342815	0.131859	0.244027
42.727273	0.121121	0.20037	0.252276	0.283938	0.107552	0.201337
51.818182	0.100004	0.16456	0.209497	0.240639	0.090623	0.170442
60.909091	0.08376	0.138665	0.177809	0.207623	0.079997	0.14905
70.000000	0.074211	0.121109	0.155804	0.183981	0.070445	0.131224
79.090909	0.067563	0.108842	0.139888	0.166533	0.064275	0.11945
88.181818	0.059832	0.096994	0.125262	0.150487	0.059214	0.109096
99.545455	0.054416	0.086805	0.112271	0.135903	0.054019	0.099311
110.909091	0.051605	0.080406	0.10332	0.125331	0.049468	0.090701
122.272727	0.048068	0.073735	0.094874	0.115648	0.0462	0.084046

Table 12. Effectiveness data for mock aero combustor with spool case.

Mock Aero Combustor with Spool (ACS)						
ReD	250030	249595	249894	249020	499468	499974
Ttin (K)	295.69	295.69	295.62	295.75	297.67	297.99
Ptin (Pa)	99824	99824	99825	99825	99902	99538
Patm (Pa)	99615	99615	99615	99615	99040	98667
Blowing Ratio	0.539	0.971	1.349	1.897	0.528	0.954
Vexit (m/s)	18.888	18.855	18.868	18.817	38.529	38.788
Free Stream Density	1.175	1.175	1.175	1.175	1.163	1.158
Exit Mach Number	0.0548	0.0547	0.0547	0.0546	0.1113	0.1120
Mass Flow Rate (kg/s)	0.00389	0.00700	0.00972	0.01364	0.00770	0.01393
T Cool, avg (K)	286.09	282.96	281.45	281.77	286.34	286.15
X/d	Adiabatic Effectiveness					
0.909091	0.790565	0.833713	0.84113	0.84187	0.766505	0.851161
1.818182	0.550071	0.6704	0.709792	0.722394	0.463917	0.666246
3.636364	0.48496	0.625718	0.676961	0.692336	0.404807	0.613737
5.909091	0.421493	0.573878	0.635224	0.653787	0.349279	0.554177
8.181818	0.373176	0.529027	0.595917	0.61604	0.307994	0.503742
10.454545	0.335866	0.491674	0.561738	0.584022	0.274788	0.459889
12.727273	0.30279	0.455746	0.528081	0.55245	0.245332	0.418574
15.454545	0.271963	0.41966	0.493365	0.51833	0.216209	0.378058
20.000000	0.229039	0.365743	0.438269	0.465026	0.177047	0.319773
24.545455	0.194022	0.318492	0.387889	0.416716	0.148295	0.274383
29.090909	0.165113	0.277	0.342364	0.371995	0.12584	0.238315
33.636364	0.141416	0.241915	0.302533	0.332673	0.108286	0.209739
42.727273	0.107517	0.189067	0.2417	0.272751	0.084801	0.168473
51.818182	0.087882	0.153982	0.199036	0.23088	0.078475	0.148335
60.909091	0.067912	0.124611	0.164105	0.19434	0.05755	0.119611
70.000000	0.056672	0.105603	0.140325	0.169719	0.049098	0.10371
79.090909	0.048347	0.091606	0.122744	0.150961	0.042356	0.090659
88.181818	0.042992	0.080562	0.108429	0.134651	0.036984	0.081887
99.545455	0.037217	0.070065	0.094794	0.11958	0.032804	0.073052
110.909091	0.032778	0.06249	0.084578	0.108409	0.028661	0.064779
122.272727	0.028358	0.055153	0.075012	0.097338	0.025347	0.058585

Table 13. Effectiveness data for mock aero combustor case.

Mock Aero Combustor (AC)						
ReD	250216	250185	250761	249299	501958	498372
Ttin (K)	296.54	296.53	296.51	297.02	298.42	298.81
Ptin (Pa)	98035	98035	98035	98036	99943	99940
Patm (Pa)	97821	97821	97821	97821	99074	99074
Blowing Ratio	0.540	0.971	1.351	1.895	0.529	0.959
Vexit (m/s)	19.348	19.344	19.386	19.331	38.885	38.693
Free Stream Density	1.150	1.150	1.151	1.149	1.161	1.159
Exit Mach Number	0.0560	0.0560	0.0561	0.0559	0.1122	0.1115
Mass Flow Rate (kg/s)	0.00391	0.00703	0.00980	0.01369	0.00776	0.01400
T Cool, avg (K)	288.01	283.75	282.15	282.47	290.18	286.48
X/d	Adiabatic Effectiveness					
0.909091	0.759099	0.81087	0.828352	0.834479	0.868431	0.818098
1.818182	0.46378	0.596771	0.653378	0.684829	0.459375	0.565797
3.636364	0.396006	0.539979	0.606732	0.644834	0.388122	0.503315
5.909091	0.332917	0.478339	0.553603	0.597746	0.323497	0.438045
8.181818	0.28726	0.427347	0.505628	0.55413	0.275984	0.384112
10.454545	0.251457	0.385003	0.463387	0.515926	0.237539	0.34043
12.727273	0.219306	0.34502	0.422693	0.477603	0.204299	0.299749
15.454545	0.191719	0.307789	0.382489	0.437911	0.173697	0.261509
20.000000	0.152639	0.253423	0.32111	0.376401	0.135427	0.210601
24.545455	0.123361	0.210215	0.271458	0.323722	0.106226	0.172267
29.090909	0.100415	0.175695	0.230145	0.278834	0.085949	0.143784
33.636364	0.083704	0.149125	0.197473	0.242303	0.071708	0.122607
42.727273	0.06042	0.111183	0.149948	0.18872	0.051685	0.092654
51.818182	0.044079	0.085345	0.116582	0.151087	0.038128	0.072776
60.909091	0.036047	0.069424	0.095753	0.125267	0.030348	0.059945
70.000000	0.028972	0.05749	0.079602	0.105968	0.024101	0.050102
79.090909	0.023616	0.048617	0.068005	0.091704	0.019008	0.041743
88.181818	0.020783	0.042631	0.059382	0.080303	0.015238	0.036096
99.545455	0.017785	0.036735	0.050787	0.069483	0.011508	0.029752
110.909091	0.014373	0.031206	0.044137	0.061295	0.009035	0.026016
122.272727	0.013013	0.027547	0.038841	0.054388	0.006413	0.022319

Table 14. Stanton number data for low turbulence case.

Low Turbulence (LT)								
ReD	249924	249767	248670	249294	249568	498604	499009	499242
Ttin (K)	291.68	294.90	295.16	295.20	295.06	293.07	294.71	294.93
Ptin (Pa)	98600	99012	99011	99012	99891	99232	100180	100179
Patm (Pa)	98396	98803	98803	98803	99683	98396	99345	99345
Blowing Ratio	0	0.542	0.967	1.342	1.896	0	0.530	0.949
Vexit (m/s)	18.656	18.932	18.879	18.931	18.769	37.652	37.696	37.765
Free Stream Density	1.176	1.168	1.167	1.167	1.178	1.174	1.178	1.178
Exit Mach Number	0.0545	0.0550	0.0548	0.0550	0.0545	0.1096	0.1094	0.1096
Mass Flow Rate (kg/s)	0	0.00390	0.00693	0.00965	0.01363	0	0.00766	0.01372
T Cool, avg (K)	291.4274	295.0268	295.2769	295.5046	295.4799	293.0811	295.1457	295.9154
X/d	Stanton Number							
1.818182	0.003629	0.004281	0.004483	0.004809	0.005411	0.002614	0.003621	0.003694
3.636364	0.002785	0.003347	0.003371	0.003575	0.003974	0.002012	0.002756	0.002732
5.909091	0.002355	0.002914	0.002847	0.002994	0.003326	0.001710	0.002438	0.002365
8.181818	0.002116	0.002643	0.002550	0.002663	0.002967	0.001537	0.002264	0.002181
10.454545	0.001944	0.002448	0.002335	0.002425	0.002705	0.001409	0.002147	0.002064
12.727273	0.001783	0.002255	0.002131	0.002205	0.002468	0.001290	0.002060	0.001978
15.454545	0.001657	0.002113	0.001981	0.002049	0.002318	0.001206	0.002055	0.001982
20.000000	0.001502	0.001948	0.001800	0.001862	0.002158	0.001104	0.002083	0.002033
24.545455	0.001380	0.001835	0.001666	0.001729	0.002064	0.001038	0.002080	0.002046
29.090909	0.001287	0.001786	0.001577	0.001650	0.002045	0.000999	0.002073	0.002046
33.636364	0.001207	0.001799	0.001532	0.001624	0.002069	0.000976	0.002054	0.002032
42.727273	0.001082	0.001979	0.001600	0.001735	0.002179	0.000969	0.002021	0.001997
51.818182	0.000987	0.002139	0.001823	0.001945	0.002253	0.000978	0.001988	0.001964
60.909091	0.000929	0.002181	0.002010	0.002081	0.002273	0.000999	0.001946	0.001928
70.000000	0.000865	0.002161	0.002076	0.002116	0.002243	0.001010	0.001919	0.001903
79.090909	0.000813	0.002157	0.002111	0.002132	0.002230	0.001028	0.001889	0.001872
88.181818	0.000778	0.002136	0.002108	0.002120	0.002203	0.001090	0.001869	0.001856
99.545455	0.000749	0.002073	0.002055	0.002058	0.002118	0.001251	0.001822	0.001811
110.909091	0.000695	0.002087	0.002073	0.002072	0.002129	0.001487	0.001810	0.001796
122.272727	0.000752	0.002039	0.002036	0.002037	0.002101	0.001618	0.001767	0.001761

Table 15. Stanton number data for small grid far case.

Small Grid Far (SG2)								
ReD	252630	249916	251147	250845	250331	500680	501224	502282
Ttin (K)	289.87	293.59	293.76	293.85	294.27	292.58	295.25	295.49
Ptin (Pa)	98805	98774	98776	98776	98776	99433	99484	99491
Patm (Pa)	98600	98566	98566	98566	98566	98600	98633	98633
Blowing Ratio	0	0.541	0.966	1.350	1.894	0	0.520	0.948
Vexit (m/s)	18.612	18.840	18.953	18.940	18.949	37.621	38.267	38.402
Free Stream Density	1.186	1.171	1.170	1.170	1.168	1.178	1.168	1.167
Exit Mach Number	0.0545	0.0548	0.0551	0.0551	0.0551	0.1096	0.1110	0.1113
Mass Flow Rate (kg/s)	0	0.00388	0.00696	0.00972	0.01363	0	0.00756	0.01382
T Cool, avg (K)	290.097	293.4036	293.6615	293.8995	294.5909	292.5352	294.9302	296.3483
X/d	Stanton Number							
1.818182	0.003761	0.004402	0.004427	0.004789	0.005371	0.0031	0.003635	0.003634
3.636364	0.002885	0.003426	0.003368	0.003574	0.003964	0.002383	0.002758	0.002707
5.909091	0.002447	0.002974	0.002871	0.003006	0.003326	0.002035	0.002431	0.002366
8.181818	0.002213	0.002711	0.002596	0.002688	0.002963	0.001856	0.002255	0.002198
10.454545	0.002042	0.002502	0.00239	0.002454	0.002705	0.001735	0.002136	0.002086
12.727273	0.001882	0.002304	0.002196	0.002241	0.00248	0.001637	0.002053	0.002011
15.454545	0.001758	0.002165	0.002059	0.002091	0.002331	0.001606	0.002052	0.002019
20.000000	0.001609	0.002021	0.001911	0.001929	0.002187	0.001635	0.002085	0.002069
24.545455	0.001492	0.001939	0.001822	0.001829	0.002107	0.001693	0.002098	0.002088
29.090909	0.001406	0.00193	0.001804	0.001804	0.002101	0.001782	0.002111	0.002103
33.636364	0.001337	0.001965	0.001837	0.001834	0.002129	0.001862	0.002106	0.002099
42.727273	0.001254	0.002109	0.002006	0.002	0.002234	0.001989	0.002089	0.00208
51.818182	0.001246	0.002222	0.002162	0.002156	0.002307	0.002054	0.002065	0.002057
60.909091	0.001317	0.002268	0.002234	0.002231	0.002326	0.002059	0.002028	0.002023
70.000000	0.001413	0.002263	0.002239	0.002238	0.002303	0.002052	0.002006	0.002001
79.090909	0.001561	0.002266	0.002246	0.002246	0.002298	0.002028	0.001976	0.001971
88.181818	0.001719	0.002252	0.002234	0.002234	0.002274	0.002014	0.001961	0.001958
99.545455	0.001846	0.00218	0.002164	0.002165	0.002193	0.001964	0.001911	0.001905
110.909091	0.001998	0.002202	0.002186	0.002185	0.002212	0.001951	0.001902	0.001899
122.272727	0.002047	0.002148	0.002134	0.002124	0.002141	0.001917	0.001841	0.001837

Table 16. Stanton number data for small grid near case.

Small Grid Near (SG1)								
ReD	250105	248970	248870	249577	249893	499592	499402	500008
Ttin (K)	293.02	295.98	294.86	296.84	296.78	296.80	296.66	296.74
Ptin (Pa)	100091	99486	99147	99083	99084	100128	98589	98587
Patm (Pa)	99886	99277	98938	98871	98871	99277	97719	97719
Blowing Ratio	0	0.544	0.969	1.348	1.891	0	0.530	0.953
Vexit (m/s)	18.540	18.904	18.834	19.127	19.144	38.246	38.812	38.879
Free Stream Density	1.189	1.170	1.170	1.161	1.162	1.170	1.152	1.151
Exit Mach Number	0.0540	0.0548	0.0547	0.0554	0.0554	0.1106	0.1123	0.1125
Mass Flow Rate (kg/s)	0	0.00391	0.00694	0.00974	0.01368	0	0.00771	0.01388
T Cool, avg (K)	293.1506	295.9822	295.0194	296.6994	296.8082	296.7291	296.6327	296.8675
X/d	Stanton Number							
1.818182	0.004076	0.004792	0.00472	0.005075	0.005714	0.003892	0.003922	0.003933
3.636364	0.003134	0.003658	0.003573	0.003783	0.004204	0.002913	0.002983	0.002947
5.909091	0.002669	0.003094	0.003026	0.003164	0.003498	0.002474	0.002598	0.002548
8.181818	0.002408	0.002751	0.002707	0.002799	0.003088	0.002249	0.002395	0.002347
10.454545	0.002224	0.002517	0.002489	0.002557	0.002823	0.002134	0.002292	0.002249
12.727273	0.002061	0.002318	0.002302	0.002352	0.002607	0.00207	0.002229	0.002194
15.454545	0.001944	0.002184	0.002182	0.002219	0.002475	0.002087	0.002234	0.002208
20.000000	0.001829	0.002066	0.002082	0.002107	0.002363	0.002148	0.002257	0.00224
24.545455	0.001768	0.002019	0.002054	0.002074	0.002316	0.002198	0.002268	0.002253
29.090909	0.001764	0.002042	0.002093	0.002111	0.002328	0.002243	0.002278	0.002262
33.636364	0.001795	0.002088	0.002153	0.002168	0.002349	0.002262	0.002275	0.002258
42.727273	0.001942	0.002216	0.00228	0.002292	0.002411	0.002262	0.002254	0.002237
51.818182	0.002116	0.002315	0.002352	0.002363	0.002441	0.002235	0.002223	0.002208
60.909091	0.00224	0.002361	0.002374	0.002379	0.002436	0.002195	0.002181	0.002168
70.000000	0.002285	0.002349	0.002348	0.00235	0.002396	0.00216	0.002149	0.002137
79.090909	0.002327	0.002355	0.002343	0.002346	0.002385	0.002127	0.002117	0.002106
88.181818	0.002333	0.00234	0.002328	0.002327	0.002361	0.00211	0.002099	0.002088
99.545455	0.002204	0.002204	0.002192	0.00219	0.002215	0.001986	0.001988	0.001981
110.909091	0.002312	0.002302	0.002288	0.002287	0.002312	0.002044	0.002037	0.002027
122.272727	0.002246	0.002258	0.002246	0.002245	0.002264	0.002007	0.002006	0.001998

Table 17. Stanton number data for large grid case.

Large Grid (GR)								
ReD	250287	251211	251062	251609	251129	500084	500417	501460
Ttin (K)	293.07	293.06	293.32	293.66	293.88	295.42	292.64	292.75
Ptin (Pa)	98334	98808	98808	98810	98810	98986	99700	99701
Patm (Pa)	98126	98600	98600	98600	98600	98126	98871	98871
Blowing Ratio	0	0.544	0.970	1.342	1.896	0	0.532	0.949
Vexit (m/s)	18.894	18.871	18.890	18.970	18.959	38.413	37.512	37.616
Free Stream Density	1.168	1.173	1.172	1.171	1.170	1.162	1.181	1.181
Exit Mach Number	0.0550	0.0550	0.0550	0.0552	0.0552	0.1114	0.1093	0.1095
Mass Flow Rate (kg/s)	0	0.00392	0.00699	0.00969	0.01368	0	0.00767	0.01371
T Cool, avg (K)	293.2944	293.4333	293.8003	294.1498	294.8386	295.2744	292.6394	293.5524
X/d	Stanton Number							
1.818182	0.003969	0.004512	0.004558	0.004855	0.005434	0.003509	0.003814	0.003785
3.636364	0.00306	0.0035	0.003456	0.003628	0.004011	0.002664	0.002875	0.002825
5.909091	0.00262	0.003026	0.002943	0.003054	0.003365	0.002299	0.002525	0.002466
8.181818	0.002378	0.002751	0.00266	0.002733	0.002999	0.002115	0.00234	0.002291
10.454545	0.00221	0.002548	0.002461	0.002508	0.002748	0.002008	0.002226	0.002185
12.727273	0.002056	0.002365	0.00228	0.00231	0.002535	0.001937	0.002149	0.002119
15.454545	0.001947	0.002246	0.002165	0.002184	0.002406	0.001943	0.002148	0.002129
20.000000	0.001836	0.002139	0.002067	0.002074	0.002294	0.002004	0.002178	0.002168
24.545455	0.001771	0.002089	0.002027	0.002029	0.002241	0.002067	0.002197	0.002189
29.090909	0.001758	0.002099	0.00205	0.002051	0.002246	0.002138	0.002226	0.002217
33.636364	0.00178	0.002132	0.002096	0.002097	0.002267	0.002189	0.002238	0.002229
42.727273	0.001912	0.002239	0.002222	0.002224	0.002341	0.002242	0.002244	0.002234
51.818182	0.002088	0.00233	0.002325	0.002323	0.002397	0.002242	0.002228	0.002218
60.909091	0.002231	0.002378	0.002375	0.002373	0.002419	0.002212	0.002195	0.002186
70.000000	0.002301	0.002387	0.002375	0.002371	0.002405	0.002186	0.002173	0.002164
79.090909	0.002361	0.002394	0.00239	0.002385	0.002406	0.002159	0.002144	0.002135
88.181818	0.002377	0.002384	0.00238	0.002376	0.002389	0.002142	0.002128	0.00212
99.545455	0.002329	0.002316	0.002311	0.002308	0.002317	0.002096	0.002082	0.002076
110.909091	0.002351	0.002338	0.002334	0.00233	0.002337	0.002077	0.002066	0.002058
122.272727	0.002303	0.002283	0.002279	0.002274	0.002278	0.002041	0.002016	0.002006

Table 18. Stanton number data for mock aero combustor with spool case.

Mock Aero Combustor with Spool (ACS)								
ReD	249450	250186	249702	249381	249480	499747	501496	499169
Ttin (K)	295.13	294.70	294.73	295.24	295.28	297.05	295.11	295.54
Ptin (Pa)	100836	98810	98809	98810	101006	101472	98346	101631
Patm (Pa)	100631	98600	98600	98600	100801	100631	97482	100801
Blowing Ratio	0	0.542	0.967	1.355	1.896	0	0.529	0.953
Vexit (m/s)	18.590	18.981	18.948	18.981	18.578	37.796	38.710	37.346
Free Stream Density	1.189	1.167	1.167	1.165	1.190	1.184	1.155	1.192
Exit Mach Number	0.0540	0.0551	0.0550	0.0551	0.0539	0.1093	0.1123	0.1082
Mass Flow Rate (kg/s)	0	0.00390	0.00695	0.00974	0.01363	0	0.00769	0.01380
T Cool, avg (K)	295.215	294.3605	294.5983	295.1877	295.1605	297.001	295.0392	295.4229
X/d	Stanton Number							
1.818182	0.004018	0.004583	0.004613	0.004919	0.005481	0.003679	0.003806	0.003795
3.636364	0.003082	0.003516	0.003476	0.003653	0.004012	0.002738	0.00287	0.002828
5.909091	0.002628	0.003027	0.002952	0.003063	0.003357	0.002349	0.002503	0.00247
8.181818	0.002395	0.002755	0.002671	0.002743	0.002996	0.002161	0.002313	0.002292
10.454545	0.002226	0.002547	0.002467	0.002511	0.002738	0.002042	0.002199	0.002183
12.727273	0.002071	0.002362	0.002285	0.002311	0.002523	0.001964	0.002119	0.002112
15.454545	0.001963	0.00224	0.002167	0.002181	0.002388	0.001967	0.002116	0.002117
20.000000	0.001854	0.002125	0.002063	0.002064	0.002271	0.002018	0.002138	0.002149
24.545455	0.00179	0.002065	0.002015	0.00201	0.002217	0.002074	0.00216	0.002172
29.090909	0.001775	0.002065	0.002026	0.00202	0.002221	0.002136	0.002189	0.002202
33.636364	0.001786	0.002088	0.002057	0.002054	0.002239	0.002177	0.002205	0.002215
42.727273	0.001889	0.002181	0.002168	0.002167	0.002312	0.002223	0.002216	0.002224
51.818182	0.002044	0.002275	0.00227	0.002268	0.002372	0.002242	0.002207	0.002214
60.909091	0.002174	0.002338	0.002333	0.00233	0.002402	0.002202	0.002179	0.002185
70.000000	0.002248	0.002354	0.002346	0.002338	0.002389	0.002184	0.002159	0.002163
79.090909	0.002324	0.002384	0.002375	0.002366	0.002403	0.002158	0.002134	0.002141
88.181818	0.002362	0.00239	0.002379	0.002369	0.002397	0.002147	0.002125	0.00213
99.545455	0.002285	0.002288	0.002278	0.002265	0.002271	0.00205	0.002037	0.002021
110.909091	0.002382	0.002375	0.002366	0.002356	0.00238	0.002096	0.002074	0.002084
122.272727	0.002333	0.002346	0.002336	0.002323	0.002345	0.002064	0.002057	0.002069

Table 19. Stanton number for mock aero combustor case.

Mock Aero Combustor (AC)								
ReD	250011	249823	251032	251057	250328	502704	499454	499230
Ttin (K)	292.45	294.52	294.45	294.45	295.48	297.19	295.42	295.76
Ptin (Pa)	100359	98336	98337	98338	99420	99326	100047	100060
Patm (Pa)	100157	98126	98126	98126	99209	98464	99209	99209
Blowing Ratio	0	0.542	0.967	1.351	1.895	0	0.529	0.952
Vexit (m/s)	18.420	19.024	19.109	19.110	18.964	38.901	37.946	38.003
Free Stream Density	1.194	1.162	1.162	1.162	1.171	1.159	1.174	1.173
Exit Mach Number	0.0537	0.0553	0.0555	0.0555	0.0550	0.1124	0.1100	0.1101
Mass Flow Rate (kg/s)	0	0.00390	0.00698	0.00976	0.01368	0	0.00767	0.01381
T Cool, avg (K)	292.4632	294.4794	294.4298	294.3927	295.3759	297.4112	295.4452	295.4576
X/d	Stanton Number							
1.818182	0.004215	0.004675	0.004664	0.004947	0.005424	0.003888	0.003864	0.003807
3.636364	0.003256	0.003591	0.003542	0.003692	0.003997	0.002889	0.002905	0.002865
5.909091	0.002809	0.003093	0.003031	0.003109	0.003351	0.002482	0.002533	0.002503
8.181818	0.002578	0.002817	0.002757	0.002797	0.002994	0.002285	0.002352	0.00233
10.454545	0.002416	0.002624	0.00257	0.002589	0.002754	0.002182	0.002245	0.002233
12.727273	0.002278	0.00246	0.002413	0.002418	0.002561	0.00212	0.002175	0.002168
15.454545	0.002197	0.002363	0.002325	0.002322	0.002449	0.002122	0.002175	0.002171
20.000000	0.002138	0.002288	0.002261	0.002254	0.002366	0.00216	0.002195	0.002195
24.545455	0.002121	0.002255	0.002238	0.002233	0.00233	0.002198	0.00222	0.002218
29.090909	0.00215	0.00227	0.00226	0.002258	0.002339	0.002243	0.002256	0.002253
33.636364	0.002192	0.002294	0.002288	0.002289	0.002354	0.002274	0.00228	0.002273
42.727273	0.002309	0.00238	0.002376	0.002379	0.002417	0.002306	0.002308	0.002298
51.818182	0.002411	0.002458	0.00245	0.002452	0.00247	0.002309	0.002307	0.0023
60.909091	0.00247	0.0025	0.002489	0.002491	0.002498	0.002284	0.002285	0.002276
70.000000	0.002471	0.002494	0.002483	0.002484	0.002485	0.002266	0.002268	0.00226
79.090909	0.002498	0.002517	0.002504	0.002505	0.002504	0.002246	0.00225	0.002243
88.181818	0.002498	0.002517	0.002504	0.002504	0.0025	0.002238	0.002242	0.002237
99.545455	0.002375	0.002391	0.00238	0.002378	0.00237	0.002124	0.002129	0.002124
110.909091	0.002495	0.002515	0.0025	0.002501	0.002496	0.002198	0.002204	0.002199
122.272727	0.002436	0.002482	0.00247	0.002469	0.002464	0.002169	0.002189	0.002185

Appendix C

Uncertainty Calculations

Uncertainty estimates for this study were done using the root sum square method shown by Moffat [44]. These uncertainties arise from several possible sources of error in data acquisition equipment, procedure, and fabrication error. All uncertainties were calculated with 95% confidence interval.

The uncertainty in adiabatic effectiveness for the low turbulence condition was calculated for the near holes region and for a region downstream. In the near holes region, the uncertainty in effectiveness was +/- 0.055 and downstream was slightly lower at +/- 0.04. Reasons for this uncertainty include the unsteadiness of the flow and errors in thermocouple temperature measurement.

The uncertainty in Stanton number was also calculated for the low turbulence condition for the near holes region and a region downstream. Due to issues such as unheated starting length and unsteadiness in the flows, the near holes region Stanton number uncertainty was +/- 0.00028 or around 8%. Downstream the uncertainty was less, with values of +/- 0.0001 or about 5%.

REFERENCES

[1] Downs, J.P., and Landis, K.K., 2009, "Turbine Cooling Systems Design—Past, Present and Future," ASME Paper No. GT2009-59991.

[2] Bunker, R.S., 2005, "A Review of Shaped Hole Turbine Film Cooling Technology," *J. Heat Transfer,* v. 127, pp. 441-453.

[3] Sundaram, N., and Thole, K.A., 2006, "Effects of Surface Deposition, Hole Blockage, and TBC Spallation on Vane Endwall Film Cooling," ASME Paper No. GT2006-90379.

[4] Bruce-Black, J.E., Bogard, D.G., Davidson, F.T., and Johns, D.R., 2009, "Practical Slot Configurations for Turbine Film Cooling Applications," ASME Paper No. GT2009-59674.

[5] Busche, M.L., Kingery, J.E., and Ames, F.E., 2014, "Slot Film Cooling in an Accelerating Boundary Layer with High Free-stream Turbulence," ASME Paper No. GT2014-25360.

[6] Bunker, R.S., 2011, "A Study of Mesh-Fed Slot Film Cooling," *J. Turbomachinery,* v. 133, pp.1-11.

[7] Simon, F.F., 1986, "Jet Model for Slot Film Cooling with Effect of Free-Stream and Coolant Turbulence," *NASA Technical Paper,* No. 2655, pp. 1-18.

[8] L'Ecuyer, M.R., and Soechting, F.O., 1985, "A Model for Correlating Flat Plate Film Cooling Effectiveness for Rows of Round Holes," *Heat Transfer and Cooling in Gas Turbines: AGARD Conference Proceedings No. 390.*

[9] Pedersen, D.R., Eckert, E.R.G., and Goldstein, R.J., 1977, "Film Cooling with Large Density Differences Between the Mainstream and the Secondary Fluid Measured by the Heat-Mass Transfer Analogy," *J. Heat Transfer,* v. 99, pp. 620-627.

[10] Sinha, A.K., Bogard, D.G., and Crawford, M.E., 1990, "Film Cooling Effectiveness Downstream of a Single Row of Holes with Variable Density Ratio," ASME Paper No. 90-GT-43.

[11] Liu, K., Yang, S., and Han, J., 2012, "Influence of Coolant Density on Turbine Blade Film Cooling with Compound Angle Shaped Holes," ASME Paper No. GT2012-69117.

[12] Foster, N.W., and Lampard, D., 1980, "The Flow and Film Cooling Effectiveness Following Injection through a Row of Holes," *J. Eng. Gas Turbines Power,* v. 102, pp. 584-558.

[13] Leiss, C., 1975, "Experimental Investigation of Film Cooling with Ejection from a Row of Holes for the Application to Gas Turbine Blades," *J. Eng. Gas Turbines Power,* v. 97, pp. 21-27.

[14] Qin, Y., Ren, J., and Jiang, H., 2014, "Effects of Streamwise Pressure Gradient and Convex Curvature on Film Cooling Effectiveness," ASME Paper No. GT2014-25808.

[15] Muska, J.F., Fish, R.W., and Suo, M., 1976, "The Additive Nature of Film Cooling from Rows of Holes," *J. Eng. Gas Turbines Power,* v. 94, pp 457-463.

[16] Laveau, B., and Abhari, R.S., 2010, "Influence of Flow Structure on Shaped Hole Film Cooling Performance," ASME Paper No. GT2010-23032.

[17] Bunker, R.S., 2010, "Film Cooling: Breaking the Limits of Diffusion Shaped Holes," *Heat Transfer Research,* v. 41, pp. 627-650.

[18] Dittmar, J., Schulz, A., and Witting, S., 2003, "Assessment of Various Film Cooling Configurations Including Shaped and Compound Angle Holes Based on Large-Scale Experiments," *J. Turbomachinery,* v. 125, pp. 57-64.

[19] Saumweber, C., and Schulz, A., 2012, "Effect of Geometry Variations on the Cooling Performance of Fan-Shaped Cooling Holes," *J. Turbomachinery,* v. 134, pp. 1-16.

[20] Yu, Y., Yen, C.-H., Shih, T.I.-P., Chyu, M.K., and Gogieni, S., 2002, "Film Cooling Effectiveness and Heat Transfer Coefficient Distribution Around Diffusion Shaped Holes," *J. Heat Transfer,* v. 124, pp. 820-827.

[21] Colban, W., Thole, K.A., and Haendler, M., 2006, "A Comparison of Cylindrical and Fan-Shaped Film Cooling Holes on a Vane Endwall at Low and High Free-Stream Turbulence Levels," ASME Paper No. GT2006-90021.

[22] Saumweber, C., and Schulz, A., 2004, "Interaction of Film Cooling Rows: Effects of Hole Geometry and Row Spacing on the Cooling Performance Downstream of the Second Row of Holes," *J. Turbomachinery,* v. 126, pp. 237-246.

[23] Brauckmann, D., and von Wolfersdorf, J., 2005, “Influence of Compound Angle on Adiabatic Film Cooling Effectiveness and Heat Transfer Coefficient for a Row of Shaped Film Cooling Holes,” ASME Paper No. GT2005-68036.

[24] Colban, W., Gratton, A., Thole, K.A., and Haendler, M., 2005, “Heat Transfer and Film Cooling Measurements on a Stator Vane with Fan-Shaped Cooling Holes,” ASME Paper No. GT2005-68258.

[25] Mhetras, S., Han, J., and Rudolph, R., 2008, “Film Cooling Effectiveness from Shaped Film Cooling Holes for a Gas Turbine Blade,” ASME Paper No. GT2008-50916.

[26] Schroeder, R.P., and Thole, K.A., 2014, “Adiabatic Effectiveness Measurements for a Baseline Shaped Film Cooling Hole,” ASME Paper No. GT2014-25992.

[27] Saumweber, C., and Schulz, A., 2012, “Free-Stream Effects on the Cooling Performance of Cylindrical and Fan-Shaped Cooling Holes,” *J. Turbomachinery,* v. 134, pp. 1-12.

[28] Saumweber, C., Schulz, A., and Wittig, S., 2003, “Free-Stream Turbulence Effects on Film Cooling with Shaped Holes,” *J. Turbomachinery,* v. 125, pp. 65-73.

[29] Mayhew, J.E., Baughn, J.W., and Byerley, A.R., 2002, “The Effect of Free-Stream Turbulence on Film Cooling Adiabatic Effectiveness,” ASME Paper No. GT2002-30172.

[30] Mayhew, J.E., Baughn, J.W., and Byerley, A.R., 2002, “The Effect of Free-Stream Turbulence on Film Cooling Heat Transfer,” ASME Paper No. GT2002-30173.

[31] Ames, F.E., 1998, “Aspects of Vane Film Cooling with High Turbulence: Part I-Heat Transfer,” *J. Turbomachinery,* v. 120, pp.768-776.

[32] Ames, F.E., 1998, “Aspects of Vane Film Cooling with High Turbulence: Part II-Adiabatic Effectiveness,” *J. Turbomachinery,* v. 120, pp.777-784.

[33] Cutbirth, J.M., and Bogard, D.G., 2002, “Evaluation of Pressure Side Film Cooling with Flow and Thermal Field Measurements—Part II: Turbulence Effects,” *J. Turbomachinery,* v. 124, pp. 678-685.

[34] Mayhew, J.E., Baughn, J.W., and Byerley, A.R., 2004, “The Effect of Free-Stream Turbulence on Film Cooling Heat Transfer Coefficient and Adiabatic Effectiveness using Compound Angle Holes,” ASME Paper No. GT2004-53230.

[35] Wright, M.W., McClain, S.T., and Clemenson, M.D., 2011, “PIV Investigation of the Effect of Free-Stream Turbulence Intensity on Film Cooling from Fan-Shaped Holes,” ASME Paper No. GT2011-46127.

[36] Davidson, F.T., Bruce-Black, J.E., Bogard, D.G., and Johns, D.R., 2008, “Adiabatic Effectiveness on the Suction Side of a Turbine Vane and the Effects of Curvature at the Point of Injection,” ASME Paper No. GT2008-51350.

[37] Gandavarapu, P., 2011, "The Influence of High Turbulence Intensity and Large Leading Edge Reynolds Numbers on Stagnation Region Heat Transfer", *University of North Dakota,* Grand Forks, ND.

[38] Chowdhury, N.K., and Ames, F.E., 2013, “The Response of High Intensity Turbulence in the Presence of Large Stagnation Regions,” ASME Paper No. GT2013-95055.

[39] Kays, W., Crawford, M., and Weigand, B., 2005, “Convective Heat and Mass Transfer”, McGraw-Hill, New York, p. 546.

[40] Kingery, J.E., and Ames, F.E., 2015, “Stagnation Region Heat Transfer Augmentation at Very High Turbulence Levels,” ASME Paper No. GT2015-42420.

[41] Ames, F.E., and Moffat, R.J., 1990, "Heat Transfer with High Intensity, Large Scale Turbulence: The Flat Plate Turbulent Boundary Layer and the Cylindrical Stagnation Point", *Stanford University,* Palo Alto, CA.

[42] Busche, M.L., 2013, “Experimental Investigation of the Effect of Turbulence on Slot-Fed Film Cooling Adiabatic Effectiveness and Downstream Heat Transfer,” *University of North Dakota,* Grand Forks, ND

[43] Jaswal, I., 2008 "Aerodynamic Losses and Heat Transfer for a Covered Trailing Edge Turbine Vane with a High Solidity Low Pressure Drop Pedestal Pin Fin Array and Variable Coolant Ejection", *University of North Dakota,* Grand Forks, ND.

[44] Moffat, R.J., 1988, “Describing the Uncertainties in Experimental Results,” *Experimental Thermal and Fluid Science,* v. 1, pp. 3-17.